DEPARTMENT OF PHYSICS AND ASTRONOMY

UNIVERSITY OF HEIDELBERG

Master Thesis

in Physics
submitted by

Felix Reidt

born in Schwetzingen

2012

Analysis of Double-Gap Events in Proton-Proton Collisions at $\sqrt{s} = 7$ TeV with the ALICE Experiment at the LHC

This master thesis has been carried out by Felix Reidt at the
Physikalisches Institut at the University of Heidelberg
under the supervision of
Prof. Dr. Johanna Stachel

Analysis of Double-Gap Events in Proton-Proton Collisions at $\sqrt{s} = 7$ TeV with the ALICE Experiment at the LHC

This thesis focuses on identifying the signatures of central diffraction in proton-proton collisions at a centre-of-mass energy of $\sqrt{s} = 7$ TeV. A double-gap topology is used for filtering central-diffractive events from a minimum-bias data sample. Such a topology can be defined by detector activity in the ALICE central barrel in conjunction with the absence of detector activity outside of the central barrel. The derived double-gap cross section is $44.0 \pm 0.1(\mathit{stat.}) \pm 7.0(\mathit{syst.})\,\mu$b. The background of this cross section is estimated by studying the contributions of non-diffractive, single- and double-diffractive dissociation processes as modelled by Monte Carlo event generators, and is found to be about 10%. Further studies of this background indicate a strong multiplicity dependence of the double-gap fraction. The comparison of the two-track invariant-mass distribution of double-gap events to the invariant-mass distribution of no-gap events reveals an enhancement at an invariant mass just below $1\,\mathrm{GeV}/c^2$ and at about $1.3\,\mathrm{GeV}/c^2$.

Analyse von Double-Gap-Ereignissen in Proton-Proton-Kollisionen bei $\sqrt{s} = 7$ TeV mit dem ALICE Experiment am LHC

Der Schwerpunkt dieser Masterarbeit liegt in der Identifizierung und Charakterisierung von zentral diffraktiven Ereignissen in Proton-Proton-Kollisionen bei einer Schwerpunktsenergie von $\sqrt{s} = 7$ TeV. Die zentral diffraktiven Ereignisse werden durch eine Double-Gap-Topologie selektiert. Diese Topologie ist definiert durch Detektorsignale im zentralen Barrel des ALICE Experiments verbunden mit fehlender Aktivität in den Detektoren außerhalb des Barrels. Der aus den Daten gewonnene Double-Gap-Wirkungsquerschnitt ist $44.0 \pm 0.1(\mathit{stat.}) \pm 7.0(\mathit{syst.})\,\mu$b. Der dazugehörige Untergrund wird durch die Analyse von nicht-diffraktiven, einfach und doppelt diffraktiv dissoziativen Reaktionen untersucht, die von Monte-Carlo-Ereignisgeneratoren erzeugt sind. Der Anteil des Untergrunds am Wirkungsquerschnitt beläuft sich auf etwa 10%. Die weitere Untersuchung des Untergrunds zeigt eine starke Multiplizitätsabhängigkeit des Double-Gap-Verhältnisses. Der Vergleich der Zwei-Teilchen invarianten Massenverteilung von Double-Gap- und No-Gap-Ereignissen zeigt eine Überhöhung bei invarianten Massen leicht unterhalb von $1\,\mathrm{GeV}/c^2$ und bei etwa $1.3\,\mathrm{GeV}/c^2$.

Contents

1. Introduction

The Large Hadron Collider (LHC) started operation by colliding protons on November 23^{rd}, 2009. With its current and future centre-of-mass energies of up to 14 TeV in proton-proton collisions and 5.5 TeV per nucleon pair in lead-lead collisions, high-energy physics enters a new era. The LHC proton-proton physics programme aims to answer fundamental questions regarding the Standard Model, which combines three of the four known interactions at the quantum level. The heavy-ion physics programme focuses on the study of strongly interacting matter at LHC energies, where large energy densities are reached. At these energy densities, a phase transition or rapid crossover is expected to occur reflecting changes of the non-perturbative QCD vacuum [1]. In particular, the restoration of chiral symmetry and the onset of deconfinement are predicted as consequences of these changes.

The LHC physics programme is currently addressed by seven experiments. ATLAS[1] and CMS[2] are multi-purpose experiments optimised for the detection of rare probes, such as the Higgs particle, and for physics beyond the Standard Model. The ALICE[3] experiment is dedicated to heavy-ion physics. Its physics programme is focused on the signatures of the QCD phase transition at high energy densities. LHCb[4] is a forward spectrometer built to study B-meson physics. The concept behind LHCf[5] is to measure the energy flow at very forward direction at cosmic-ray energies. MoEDAL[6] attempts to detect heavily-ionising particles such as magnetic monopoles and other exotic states. TOTEM[7] is designed to measure the total, the elastic and the inelastic as well as the diffractive cross sections in proton-proton collisions.

The Standard Model of particle physics gives a unified picture of the electromagnetic, the weak and the strong force, based on the principle of local gauge invariance. It is spectacularly successful and in good agreement with experimental results from many experiments. The electromagnetic and the weak component of the Standard Model are unified to the electroweak interaction represented by the symmetry $\mathrm{SU_L(2)\times U_Y(1)}$ [2–4]. This symmetry is spontaneously broken to the $\mathrm{U_{em}(1)}$ symmetry of Quantum Electrodynamics (QED) by the Higgs mechanism [5–8]. The strong-interaction part is described by Quantum Chromodynamics (QCD), with an inherent SU(3) colour symmetry [9, 10]. This SU(3) symmetry results in self-interactions of gluons. The self-interactions lead to a running coupling constant

---

[1] ATLAS: **A** **T**oroidal **LHC** **A**pparatu**S**

[2] CMS: **C**ompact **M**uon **S**olenoid

[3] ALICE: **A** **L**arge **I**on **C**ollider **E**xperiment

[4] LHCb: **LHC** **b**eauty

[5] LHCf: **LHC** **f**oward

[6] MoEDAL: **Mo**nopole and **E**xotics **D**etector **A**t the **L**HC

[7] TOTEM: **TOT**al **E**lastic and diffractive cross section **M**easurement

$\alpha_s(q^2)$ and the two unique features of QCD, asymptotic freedom and confinement. Asymptotic freedom reflects the fact that strongly interacting particles behave essentially as free and non-interacting at asymptotically high energies. Due to confinement, only colour-neutral particles are seen in the detector. QCD calculations on the lattice predict a phase transition or rapid crossover into a deconfined state at high energy densities as available in heavy-ion collisions at the LHC [11]. This deconfined phase is called Quark-Gluon Plasma (QGP).

In QCD the running coupling constant $\alpha_s(q^2)$ is small for large momentum transfers q^2. Perturbative calculations can therefore be carried out in this domain. For processes with small momentum transfer q^2, the coupling constant $\alpha_s(q^2)$ is large. As a result, a perturbative description of these processes is not possible, and effective models with effective degrees of freedom have to be used. For example, the nuclear force at low energies is successfully described by using the attractive pion exchange potential and a repulsive core at small distances due to ρ-meson exchange.

In perturbative Quantum Chromodynamics (pQCD) the strong interaction is mediated in first order by the exchange of a coloured gluon, which couples to coloured quarks and gluons. In higher order, many gluons can be exchanged. An exchanged multi-gluon object can, however, be in a colour neutral state. Such exchanges transfer only little energy and momentum and lead to specific features of these processes. First, the final-state particles are forward peaked close to the beam rapidity. Second, these events show large ranges in rapidity without activity, so-called gaps. Such types of interactions are called diffractive processes.

In addition to the exchange of a colour-neutral object between the two beam particles, the fusion of two colour-singlets is possible. Such reactions are central-diffractive events. This type of event is characterised by particle production at central rapidity and large rapidity gaps in between the activity and the beam remnants.

Diffractive reactions at a soft scale can currently only be described by phenomenological models based on Regge theory [12–14]. At the high centre-of-mass energies of the LHC, cross sections of diffractive reactions with an intrinsic hard scale are measurable, such as diffractive dijet production. This hard scale enables a formulation of these processes within the framework of pQCD. The study of diffractive reactions at both the soft and the hard scale is therefore of interest to study the nature of the colour-singlet exchange in the interplay of Regge theory and pQCD.

This thesis is structured as follows. Chapter 2 introduces diffraction with its common concepts and focuses on central diffraction and its history. In Chapter 3, the ALICE experiment is presented. The physics analysis which is subject of this thesis is described in Chapter 4 and the corresponding results are discussed in Chapter 5. A summary and an outlook are given in Chapter 6. The evaluation of the triggered double-gap data can be found in Appendix A, and the ESD pre-selection is explained in Appendix B.

2. Diffraction

Diffraction is a well-known concept in optics. This phenomenon describes the scattering of light waves on objects which are large compared to the wavelength. Characteristic features of diffracted light are the very forward-focused intensity with a diffraction pattern of maxima and minima. In hadronic physics, a class of events is observed with similar features of forward-focused intensity and diffraction pattern. Such hadronic events are therefore known as diffractive interactions. However, diffraction in hadronic physics has an inelastic component reflecting the internal structure of the hadron. In this chapter the basic concepts behind hadronic diffraction and its historical background are outlined.

2.1. Regge Theory

In the early 1960's before the advent of Quantum Chromodynamics (QCD) [9, 10], many hadronic reactions were analysed by using Regge theory. In 1959 Tullio Regge extended the scattering theory of non-relativistic quantum mechanics to complex angular momenta l [12]. Presuming real values of l, the bound states of an attractive spherically symmetric potential are grouped into clusters with increasing angular momentum and energy. In the partial-wave amplitude, the bound states are represented by poles $\alpha(k)$. Due to Regge's continuation to complex values of l, the singularities turn out to be described by

$$l = \alpha(k) \ . \tag{2.1}$$

Here, k denotes the wave vector. $\alpha(k)$ is a so-called Regge trajectory.

At that time a different approach consisted in using the S-matrix framework. The corresponding probability for the transition from an initial state $|i\rangle$ to a final state $|f\rangle$ is (for orthonormal states)

$$P_{i\to f} = |\langle f|S|i\rangle|^2 \ . \tag{2.2}$$

The S-matrix has three postulated important properties:

Unitarity

As a consequence of probability conservation the unitarity of the S-matrix follows, which is the basis for the optical theorem

$$\sigma_{\mathrm{tot}} = \frac{2}{\Phi}\,\mathrm{Im}\,A_{\mathrm{el}}(s, t=0) \ , \tag{2.3}$$

relating the total cross section σ_{tot} to the imaginary part of the forward elastic scattering amplitude A_{el} and the flux factor Φ.

Analyticity

A further important property is analyticity, the fact that scattering amplitudes are analytic functions of the Mandelstam variables[1] regarded to be complex. The amplitudes contain only the singularities required by unitarity.

Crossing

Crossing symmetry relates the amplitudes of processes which are connected by the exchange of an incoming and an outgoing particle by the corresponding outgoing and incoming antiparticle, respectively:

$$A_{1+2\to 3+4}(s,t,u) = A_{1+\bar{3}\to\bar{2}+4}(t,s,u) \tag{2.4}$$

While the reaction $1+2\to 3+4$ is in the domain $s>0$ and $t,u<0$, the $1+\bar{3}\to\bar{2}+4$ is in the domain $t>0$ and $s,u<0$. Additive quantum numbers are conserved in both reactions. As an example, the amplitudes of the hadronic interactions $\pi^+ + \pi^0 \to \pi^+ + \pi^0$ and $\pi^+ + \pi^- \to \pi^0 + \pi^0$ as well as the ones of Møller ($e^-e^- \to e^-e^-$) and Bhabha ($e^-e^+ \to e^-e^+$) scattering are related by crossing symmetry.

Chew, Frautschi and Gribov applied the concepts of Regge to high-energy particle scattering [13, 14]. The resulting relativistic partial-wave amplitude $A(l,t)$ has simple poles at

$$l = \alpha(t)\ . \tag{2.5}$$

For fixed t and in the asymptotic limit of the centre-of-mass energy $s\to\infty$, each pole contributes to the scattering amplitude as

$$A(s,t) \underset{s\to\infty}{\sim} s^{\alpha(t)}\ . \tag{2.6}$$

However, not only simple singularities arise in the partial wave amplitude but also more complicated ones like cuts. A further detailed review on Regge theory can be found in [15–18].

Within this framework, the strong interaction is mediated by the exchange of virtual particles in the t-channel, as depicted in Fig. 2.1. These particles are clustered on a so-called Regge trajectory or Reggeon, which is often abbreviated as $\mathbb{R}$. This clustering combines particles lying on a trajectory in a Chew-Frautschi plot. In such a plot the ordinate shows angular momenta l which are equal to $\alpha(t)$. The Mandelstam variable t, which corresponds to the squared particle mass, is plotted on the abscissa. In Fig. 2.2, four approximately degenerate Regge trajectories for the particles ρ, ω, f_2 and a_2 are shown. While the trajectories have the same intercept, they have different parity, charge parity, G-parity, isospin I and signature ξ shown

---

[1] Mandelstam variables s,t,u in a two-body process $1+2\to 3+4$:
$s=(p_1+p_2)^2$, $t=(p_1-p_3)^2$, $u=(p_1-p_4)^2$ with $s+t+u=\sum m_i^2$

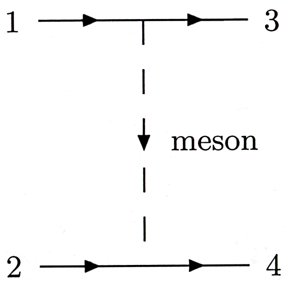

Figure 2.1.: Single meson exchange in the t-channel, taken from [17].

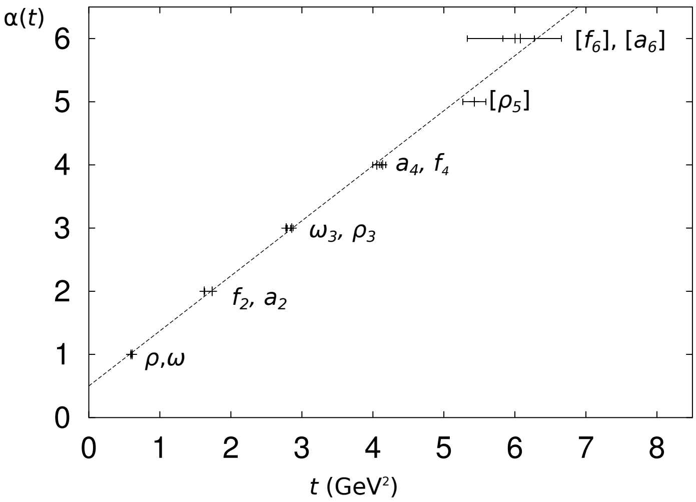

Figure 2.2.: Leading mesonic Regge trajectories, adapted from [15].

in Table 2.1. The signature quantum number is positive for trajectories of mesons with even spins and negative for odd spins. Trajectories of other particles, i.e. strange mesons or baryons, are found to have lower intercepts than the ones shown in Fig. 2.2.

2.1.1. Total Hadronic Cross Section

The scattering amplitude of a two-body process $1 + 2 \to 3 + 4$ is written in Regge theory as

$$A(s,t) = \beta(t)\eta(t)s^{\alpha(t)} , \tag{2.7}$$

with the residue $\beta(t)$ and $\eta(t)$ the signature factor which depends on the signature quantum number ξ of the exchanged trajectory. Using the optical theorem in (2.3), the total cross section from an exchange of a single trajectory is thus derived to be

$$\sigma_{\text{tot}} \underset{s\to\infty}{\simeq} \frac{1}{s} \operatorname{Im} A(s,t=0) \underset{s\to\infty}{\sim} s^{\alpha(0)-1} , \tag{2.8}$$

state	**P**	**C**	**G**	**I**	ξ
f_2	$+1$	$+1$	$+1$	0	$+1$
ρ	-1	-1	$+1$	1	-1
ω	-1	-1	-1	0	-1
a_2	$+1$	$+1$	-1	1	$+1$

Table 2.1.: Quantum numbers (parity, charge conjugation, G-parity, isospin and signature) of particles on the mesonic trajectory.

and for several contributing Regge trajectories

$$\sigma_{\text{tot}} \sim \sum_i A_i s^{\alpha_i(0)-1} \ . \tag{2.9}$$

For trajectories with intercepts smaller than one, Eq. 2.9 leads to a decreasing energy dependence of the total cross section. The experimentally measured hadronic cross section shows, however, a continuously decreasing behaviour up to $\sqrt{s} \sim 20\,\text{GeV}$ and an increase for higher energies. This behaviour is shown in Fig. 2.3 for the proton-proton and the proton-antiproton total cross section, together with a Regge-based fit function described in [19]. The total hadronic cross section at the LHC energy of $\sqrt{s} = 7\,\text{TeV}$ has recently been measured by the TOTEM collaboration to be 98 mb [20].

2.1.2. The Pomeron

In order to comply with the observed energy dependence of the total cross section at high energies, a trajectory with an intercept larger than one is needed. This trajectory is named Pomeron and is often abbreviated as $\mathbb{P}$. In contrast to the other trajectories, which are defined by well-known hadronic states, the particle content of the Pomeron is unknown. Candidates for the physical states defining the Pomeron trajectory are gluonic bound states, so-called glueballs. A Pomeron exchange is assumed to be compatible with the exchange of vacuum quantum numbers, i.e. parity $P = +1$, charge parity $C = +1$, G-parity $G = +1$, isospin $I = 0$ and a signature factor of $\xi = +1$. Donnachie and Landshoff fitted the available hadronic cross-section data for pp, p$\bar{\text{p}}$, π^-p, π^+p, K$^+$p and K$^-$p collisions to a power law [21] resulting in

$$\sigma_{\text{tot}} = X \cdot s^{0.08} + Y \cdot s^{-0.45} \tag{2.10}$$

with different prefactors X and Y for the different hadronic channels. From a comparison with Eq. 2.9, the intercept of the Pomeron trajectory is identified to be $\alpha_{\mathbb{P}}(0) = 1.08$. The corresponding slope $\alpha'_{\mathbb{P}} = 0.25\,\text{GeV}^{-2}$ is determined from fitting the t-dependence of elastic scattering data at a fixed energy [22].

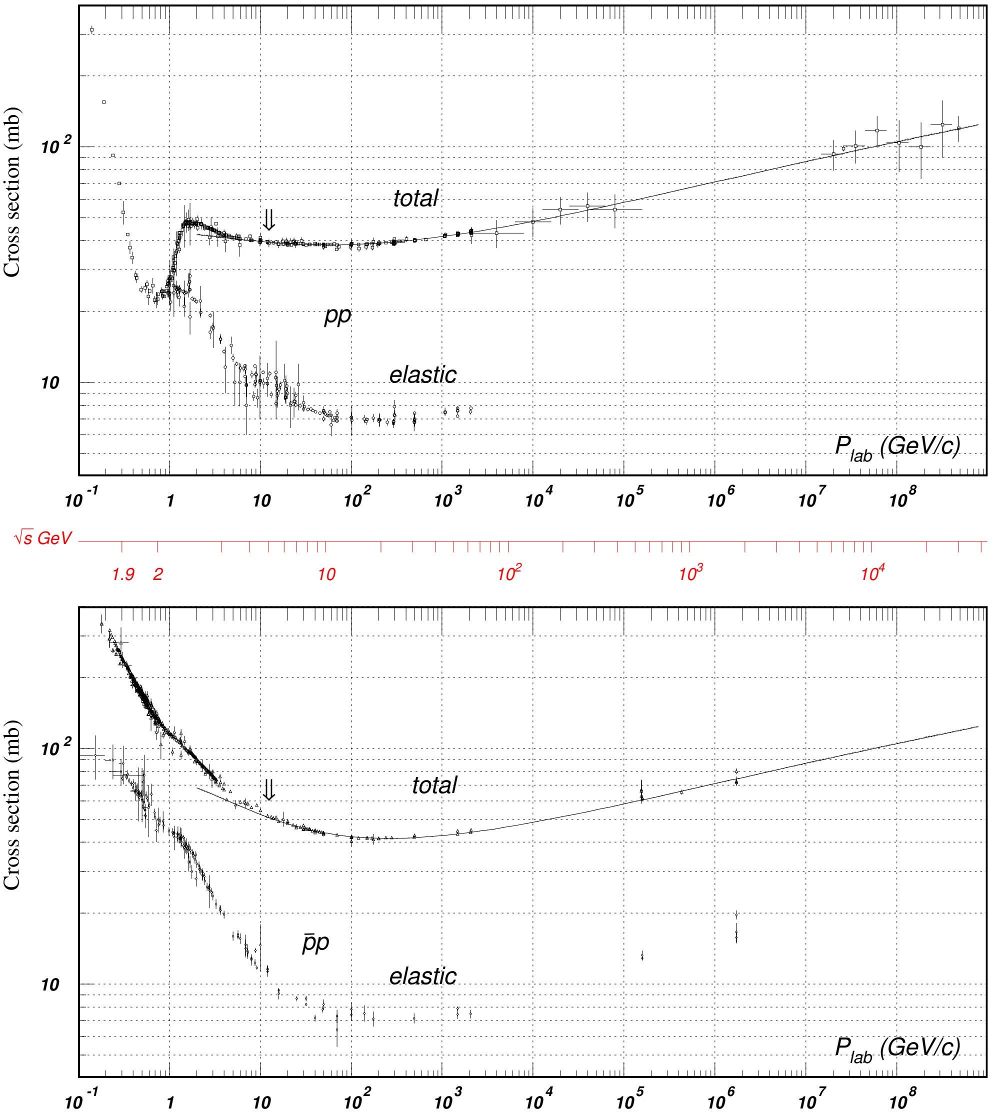

Figure 2.3.: Total and elastic cross sections in pp (upper figure) and p̄p (lower figure) collisions, taken from [19].

The nature of the Pomeron is presently not well understood. Close and Schuler find it to be compatible with a non-conserved vector current [23]. According to Nachtmann et al., this is in contradiction to principles known from Quantum Field Theory (QFT). In QFT, a vector couples with a different sign to particles and antiparticles, the Pomeron however does not make any distinction. In the Nachtmann-Ewerz-Maniatis (NEM) model, a rank-two tensor-like coupling is used for processes with an exchange of $C = +1$, and a vector-like coupling for a $C = -1$ exchange [24].

2.2. Diffractive Topologies

Diffractive reactions in hadronic physics are Pomeron-induced processes. Such hadronic interactions can be grouped into families of different topologies, characterised by the pseudorapidity distribution of the final state particles. A typical feature of diffractive interactions are regions in pseudorapidity η without activity, so-called pseudorapidity gaps. The resulting topologies are shown in Fig. 2.4.

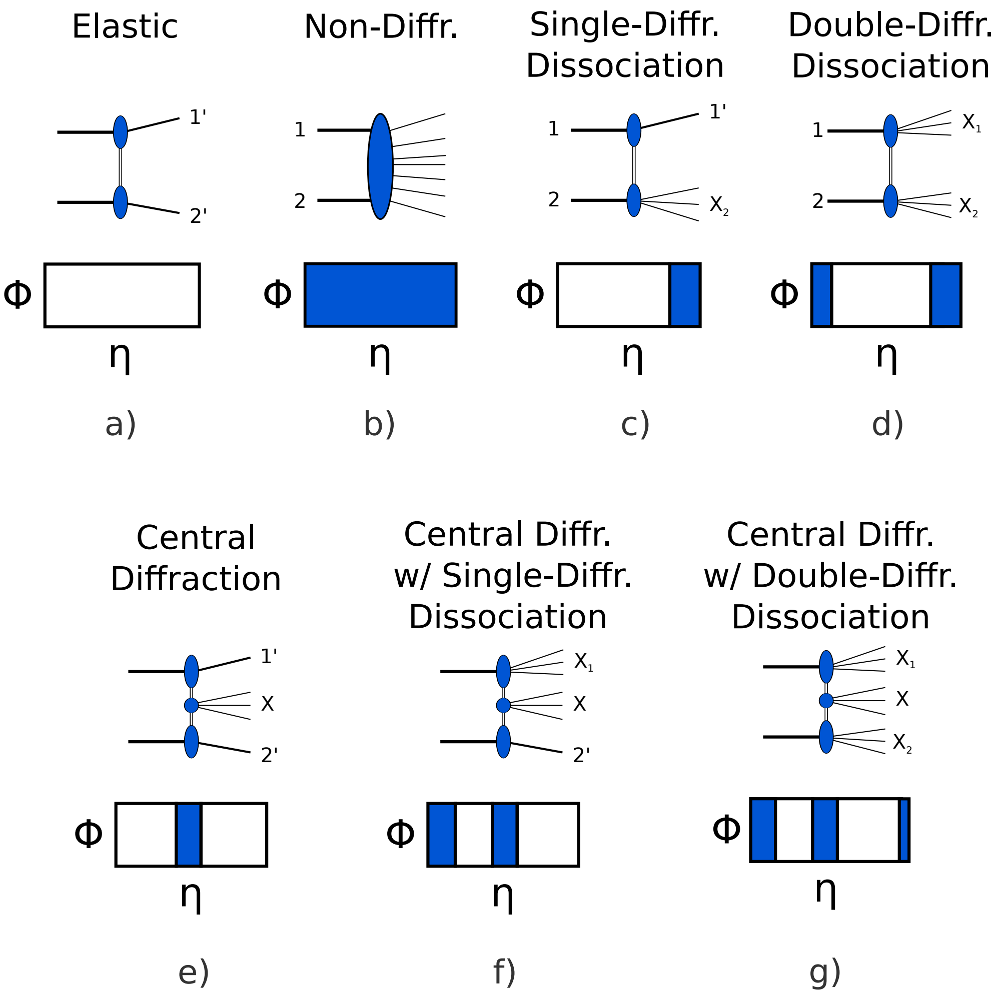

Figure 2.4.: Diffractive event topologies.

Elastic proton-proton scattering can be due to the electromagnetic or the strong interaction mediated by photon or Pomeron exchange, respectively. First such measurements at the LHC by the TOTEM collaboration resulted in 25 mb for the strong elastic scattering contribution [20]. Elastic scattering corresponds to drawing a) in Fig. 2.4.

About half of the total hadronic cross section of 98 mb is of non-diffractive origin, as depicted in part b) of Fig. 2.4. Even though there is no Pomeron exchange in this type of reaction, rapidity gaps can exist due to multiplicity fluctuations. These gaps of size $\Delta\eta$ are distributed according to

$$\frac{\mathrm{d}N}{\mathrm{d}\Delta\eta} \sim e^{-\Delta\eta} \; . \tag{2.11}$$

Due to the exponential suppression of gaps, large rapidity gaps are significantly suppressed in non-diffractive events.

In single- and double-diffractive dissociation, one or both of the two beam particles get excited by a Pomeron exchange and break up. At $\sqrt{s} = 7\,\mathrm{TeV}$, the corresponding cross sections have been measured to be 14 mb and 9 mb, respectively [25]. These processes correspond to drawing c) and d) in Fig. 2.4. For single-diffractive dissociation the momentum of the intact beam particle can be measured using forward detectors to characterise the event. Double-diffractive dissociation, however, can only be accessed via rapidity gaps, since the detection and energy measurement of all fragments of the beam remnants is beyond the capability of current detector technology. For single-diffractive dissociation, the gap in pseudorapidity is

$$\Delta\eta \simeq \ln\left(\frac{s}{M^2c^4}\right) = -\ln\left(\xi\right) \;, \tag{2.12}$$

with M the mass of the excited beam particle and ξ the fractional energy loss of the intact beam particle. For rather high diffractive masses M of about $100\,\mathrm{GeV}/c^2$, the gap reaches approximately to mid-rapidity for a centre-of-mass energy of 7 TeV. For smaller masses, the hadronic activity is narrowed to a more forward pseudorapidity range. The mass limits for detection in the ALICE experiment, described in Chapter 3, are about 6 and $13\,\mathrm{GeV}/c^2$ in the positive and negative pseudorapidity region, respectively. A similar expression can be obtained [25] for double-diffractive dissociation as well, which is found to be

$$\Delta\eta \simeq \ln\left(\frac{s s_0}{M_1^2 M_2^2 c^8}\right) \;, \tag{2.13}$$

with a scale s_0 taken to be $1\,\mathrm{GeV}^2$ and the diffractive masses of the two beam remnants M_1 and M_2.

Among the diffractive topologies shown in Fig. 2.4, the contribution of central diffraction to the total cross section is the smallest. PHOJET [26] predicts it to be 1.3 mb at a centre-of-mass energy of 7 TeV. According to a more recent PYTHIA8 tune [27], called Minimum-Bias Rockefeller (MBR) by Ciesielski and Goulianos [28], the cross section is $800\,\mu\mathrm{b}$ at this energy. Central diffraction, shown in drawings e), f) and g) of Fig. 2.4, can experimentally be identified by defining a double-gap topology condition. The three topologies e), f) and g) contribute differently as a function of the gap coverage. Central diffraction without diffractive dissociation of the protons can in principle be detected by using forward-proton tagging detectors.

2.3. The Pomeron Beyond Regge Theory

Beyond the phenomenological picture as Regge trajectory, the Pomeron can also be described in the framework of QCD. The lowest-order Feynman diagram representing a Pomeron exchange is a two-gluon exchange diagram. Two gluons are necessary to keep the interaction colour neutral. The Pomeron is obtained from perturbative QCD using the Balitsky Fadin Kuraev Lipatov (BFKL) equation [29–32]. Within the evolution in $\ln(s)$, an infinite number of colour-singlet ladders is summed. Such a ladder is shown in Fig. 2.5. The vertical lines are reggeized gluons (blue) coupled to the gluon rungs (black horizontal gluons) at effective vertices. Each of the contributing ladders has a different number of rungs. The result is a hard Pomeron with a trajectory intercept of $\alpha_{\mathbb{P}}^{\text{hard}}(0) \simeq 1.5$ for $\alpha_s = 0.2$. These findings raise the question whether the soft and hard Pomeron are distinct, or whether there is a smooth transition in between depending on the involved scale. An approach starting with a hard bare BFKL Pomeron is formulated by Khoze, Martin and Ryskin [33]. A smooth transition to the soft domain is achieved by the introduction of absorptive multi-Pomeron effects. These multi-Pomeron effects represent triple-Pomeron couplings and corrections from additional Pomerons coupling to the beam particle. These corrections lead to a shrinking intercept of the Pomeron trajectory in the soft regime. This model is implemented as ‘Soft Hard Reactions involving Multi-Pomeron Scattering (SHRiMPS)’ within the SHERPA Monte Carlo generator [34]. This approach is particularly elegant, since the model contains only a few parameters and most of them have a clear physics motivation.

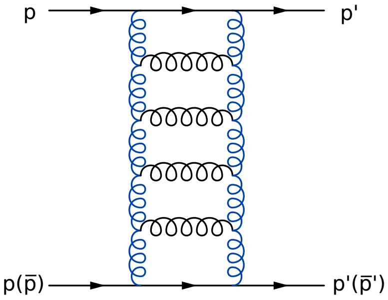

Figure 2.5.: Gluon ladder with vertical lines of reggeized gluons (blue) coupled to horizontal gluon rungs (black).

2.4. Central Diffraction

2.4.1. Properties

As described above, central diffraction is characterised by the fusion of two Pomerons leading to two large pseudorapidity gaps, as depicted in Fig. 2.6 for the example of meson pair production. In principle also Reggeon, photon and W-boson exchanges can show this topology, however the Pomeron dominates at high centre-of-mass energies [35]. Central systems which are not produced at mid-rapidity result in asymmetric gap configurations. For such events Reggeon-Pomeron interactions are the major contribution, since for the small gap the Reggeon contribution is less suppressed. Interactions involving photons are much more important in heavy-ion collisions, since the photon flux depends on the charge squared [36].

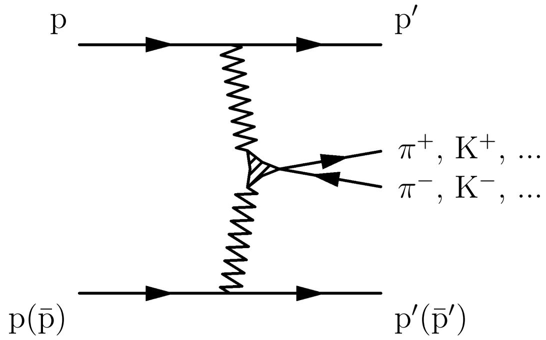

Figure 2.6.: Feynman diagram for central diffractive production of a meson pair, Pomerons displayed as zigzag lines.

The slope of the soft Pomeron trajectory is $\alpha'_{\mathbb{P}} \approx 0.25\,\mathrm{GeV}^{-2}$ as discussed in Section 2.1.2. In conjunction with the t-slope of the triple Pomeron vertex which is smaller than 1 GeV, this leads to a mean k_T in the Pomeron wave function on the order of $\sim 1\,\mathrm{GeV}$. This large k_T corresponds to a large effective temperature which should be reflected in a harder p_T-distribution of particles produced in central diffraction as compared to non-diffractive production. Furthermore, this large temperature should result in a reduced suppression of strangeness. Particle ratios such as K/π, η/π, η'/π and Λ/p are therefore expected to be enhanced in central-diffractive production as compared to non-diffractive production [37].

Double-Pomeron fusion is a gluon-rich environment and hence well-suited for glueball searches [38]. Such searches are possible studying $\pi^+\pi^-$ invariant-mass spectra by a Partial Wave Analysis (PWA), and by comparing the corresponding results from central diffractive to non-diffractive production. A review of the experimental status and concept can be found in [35].

2.4.2. Models

Depending on the scale, different models for central-diffractive production are used. For events with a hard scale much larger than Λ_QCD, a pQCD approach is suited. This hard scale can, for example, be a high mass or a high transverse momentum. Models based on Regge theory are used to describe soft events, as for example resonance production and the pion-pair continuum for invariant masses in the range

Table 2.2.: Mesons produced in central diffraction with quantum numbers $I^G = 0^+$ and $C = +1$ predicted by the NEM model.

$\mathbf{J^P}$	**Mesons**
0^-	η, $\eta'(958)$
0^+	$f_0(600)$, $f_0(980)$, $f_0(1500)$
1^+	$f_1(1285)$, $f_1(1420)$
2^+	$f_2(1270)$, $f_2'(1525)$
4^+	$f_4(2050)$

below about 2 GeV/c^2. Due to the presently low statistics, the ALICE measurement is restricted to an invariant-mass region in the soft domain.

A model able to describe the most abundant central diffractive reaction,

$$\mathrm{p} + \mathrm{p} \rightarrow \mathrm{p} + \pi^+\pi^- + \mathrm{p}$$

as well as Kaon pair production has been developed by Lebiedowicz and Szczurek [39]. Currently, this Regge-based model does not contain resonance production. Work on this, however, is ongoing and first results have been presented during the Diffraction Conference 2012 [40]. Furthermore, the resonance production approach contains different choices for the spin of the Pomeron. So far, a vector-like Pomeron according to Close and Schuler [23] and tensor-like Pomeron according to the NEM model [24] are included. The different Pomeron characteristics lead to different predictions for measurable quantities such as angular distributions and allowed quantum numbers of exclusively produced resonances. According to the NEM model the resonances shown in Table 2.2 can be produced in a double-Pomeron exchange. All these resonances have positive charge parity, an isospin of zero and positive G-parity.

2.4.3. History of Central Diffractive Measurements

With the availability of accelerators running at sufficiently high energies, the search for events with characteristics of a double-Pomeron exchange began. In the following, the most important milestones in measurements of central diffraction are summarised. A further detailed review can be found in [41].

Bubble Chamber Experiments

First searches for the double-Pomeron exchange were carried out in fixed-target experiments using bubble chambers at several places [42–46]. These studies were done using proton beams with momenta up to 205 GeV/c, corresponding to the centre-of-mass energy range of 2.5 to 20 GeV. However, it was difficult to extract the signal of two-pion central production from the background contamination by the diffractive dissociation reaction $\mathrm{p} + \mathrm{p} \rightarrow \mathrm{p} + (\mathrm{p}\pi^+\pi^-)$. Since all found events were consistent with diffractive dissociation, only upper limits for the central diffractive cross section could be derived.

Intersecting Storage Rings (ISR)

First experimental evidence for central diffraction was found by the ARCGM Collaboration [47] at the CERN Intersecting Storage Rings (ISR). The events were selected using forward proton tracking, and by requiring two tracks in the scintillator hodoscope covering the central region. Due to the lack of a magnetic field, no momentum measurement for the centrally produced system was possible. The measured cross section was almost constant in $\sqrt{s}$ within errors, decreasing from $(28.4 \pm 8.1)\,\mu$b at $\sqrt{s} = 31\,$GeV to $(16.8 \pm 3.1)\,\mu$b at $\sqrt{s} = 53\,$GeV and then slightly increasing to $(20.2 \pm 3.3)\,\mu$b at $\sqrt{s} = 62\,$GeV. These values match the phenomenological calculations by Desai et al. [48], which find the Pomeron contribution to dominate and Reggeon contribution to shrink from about $30 - 50\%$ of the total yield to less than 10% with increasing energy.

Furthermore the Split Field Magnet (SFM) collaborations CCHK, CHOV and CCHK measured cross sections and obtained invariant-mass distributions for two-track events [49–51]. In absence of Particle Identification (PID) all tracks were assumed to be pions.

The most comprehensive study on invariant-mass distributions from double-Pomeron exchange was done by the Axial Field Spectrometer (AFS) collaboration in the R807 experiment [52, 53]. Deploying forward proton tagging and gap-tagging detectors, a data sample of about 89 000 central-diffractive events at $\sqrt{s} = 63\,$GeV was recorded. Besides the two-particle channels $\pi^+\pi^-$, K^+K^- and $\mathrm{p\bar{p}}$, also the four-particle channel $\pi^+\pi^-\pi^+\pi^-$ was studied. The $\pi^+\pi^-$ invariant-mass spectrum is shown in Fig. 2.7. This spectrum is characterised by the absence of a $\rho(770)$ signal and a sharp drop at $1\,\mathrm{GeV}/c^2$. Although several attempts were made to find a glueball within this invariant-mass spectrum, there was no clear evidence found.

Fixed Target Experiments

After the shutdown of the ISR, there was a series of fixed target experiments studying central diffraction. Due to the high luminosities available, these experiments collected a large number of events. However, at the Omega spectrometer at CERN (WA76, WA91 and WA102), only a maximum centre-of-mass energy of about 29 GeV was reached. As a result, contributions from $\mathbb{RR}$- and $\mathbb{RP}$-exchanges lead to a prominent ρ-signal in the $\pi^+\pi^-$ invariant-mass distribution. Nevertheless, the data were found to match the production model based on the Pomeron behaving as

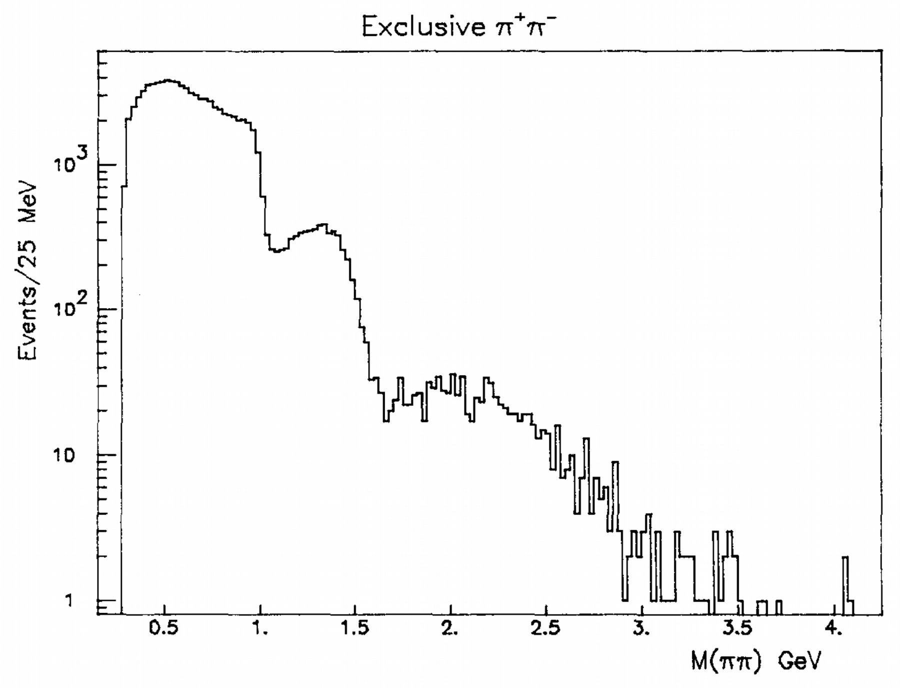

Figure 2.7.: Two pion invariant mass for central-diffractive events, obtained by the AFS collaboration at ISR in pp collisions at $\sqrt{s} = 62\,\mathrm{GeV}$, taken from [53].

a non-conserved vector current by Close and Schuler [23]. Furthermore, a search for glueballs in the invariant-mass spectra was done by a partial wave analysis without a conclusive result, however. Further measurements were carried out at Fermilab by the E960 collaboration [54], as well without a clear evidence for glueball.

CERN Proton-Antiproton Collider $Sp\bar{p}S$

Even though built to search for the W and the Z boson, UA1 also measured central diffraction using the double-gap topology at $\sqrt{s} = 630\,\mathrm{GeV}$ in proton-antiproton collisions [55]. The measurement was focused on jets and multiplicity distribution in double-Pomeron events. Moreover, UA8 measured central diffraction with forward detectors and help of the UA2 detector in the central region [56]. The measured cross section of about 3 mb for the central-diffractive mass range $2 \lesssim M \lesssim 8\,\mathrm{GeV}/c^2$ is unexpectedly large, however.

COMPASS

In 2008 and 2009, the fixed-target experiment COMPASS at the CERN SPS took data with a $190\,\mathrm{GeV}/c$ proton beam corresponding to a centre-of-mass energy of $\sqrt{s} \approx 19\,\mathrm{GeV}$. Both the slow and the fast proton were detected. An event is defined to be central-diffractive, if the two-pion system is within $-0.25 < x_F < +0.25$. Here, x_F denotes Feynman's x-variable[2]. Due to the low centre-of-mass energy, a noticeable Reggeon contribution is expected, which is the origin of a clear ρ-peak in the di-pion invariant-mass distribution. In order to search for glueballs, a partial-wave analysis is applied and first results have been presented [57].

RHIC

Recently, the STAR collaboration at the Relativistic Heavy Ion Collider (RHIC) has installed Roman Pots in order to measure central diffraction via forward proton tagging. Each of the four stations per side contains a four-layer silicon-strip detector which provides full azimuthal coverage, and an acceptance of $0.003 < -t < 0.03\,\mathrm{GeV}^2$ at $\sqrt{s} = 200\,\mathrm{GeV}$. Furthermore, the Roman Pots can be used for triggering and for measuring the transverse momentum p_T of the beam remnants. In the analysis, the transverse momenta of the two beam particles and the central tracks are summed. This p_T-sum distribution of central unlike-sign particles is found to peak at zero as expected for the signal of exclusive production due to transverse-momentum conservation. The corresponding like-sign distribution arising from incompletely detected events does not peak at zero. The cut on low p_T-sum is therefore an excellent measure to reduce the background. Together with the analysis method, the corresponding invariant-mass distribution has been presented at the Diffraction Conference 2012 [58].

Tevatron

Besides publications on central-exclusive production of dijets by DØ and by the Collider Detector at Fermilab (CDF), CDF in particular put special effort on the measurement of χ_c meson production as a standard candle in the search for central-exclusive Higgs production. In the last week of Tevatron running, in September 2011, an energy scan was done. CDF recorded data during this period by using a double-gap trigger. This double-gap data sample contains a large dataset of about 90 million events at the top energy of 1.96 TeV, 22 million at 900 GeV and 9 million at 300 GeV. The CDF detector geometry results in a central region of 2.6 units with a gap of 4.6 units on both sides. First results on invariant mass distributions and cross sections have been presented during the Diffraction Conference 2012 [59].

---

[2] Feynman x: $x_F = p_z/p_z^{\mathrm{max}}$

3. The ALICE Experiment

The ALICE experiment [60] is primarily designed for the exploration of heavy-ion collisions at LHC energies. In the design of ALICE, large emphasis was put on the capabilities of ALICE to cope with high particle densities of up to $\mathrm{d}N/\mathrm{d}\eta \approx 8000$ (at time of planning the highest anticipated multiplicity density), and on the study of the soft particle bulk. These design goals lead to a highly granular detector. Furthermore, the material budget in the central region is the lowest among the four main LHC experiments. A particle in ALICE has to traverse 11-13% of radiation length until it leaves the Time-Projection Chamber (TPC) [61] in contrast to about 40% before the calorimeters of ATLAS [62] and CMS [63]. A solenoidal magnetic field of 0.5 T allows tracking of lower p_{T} as compared to ATLAS [62] and CMS [63] which use fields of 2 T and 3.8 T, respectively. ALICE exploits a variety of particle-identification techniques. These ALICE features additionally make a proton-proton physics programme possible, which is complementary to the one of ATLAS and CMS. Because of the TPC drift time of approximately 90 μs, the maximum possible instantaneous luminosity is about $5 \cdot 10^{30}\,\mathrm{cm}^{-2}\mathrm{s}^{-1}$.

3.1. Detectors

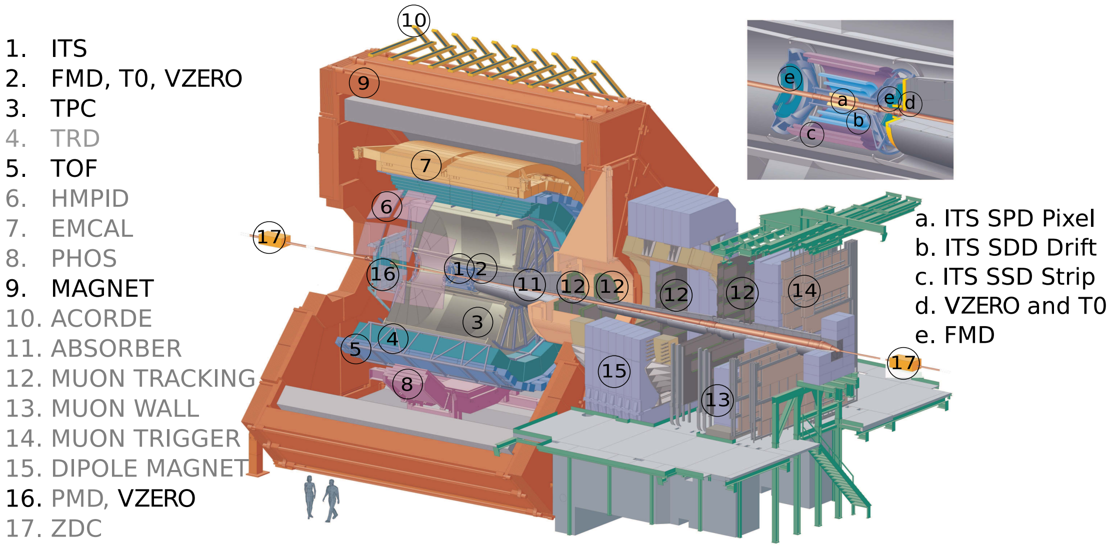

Figure 3.1.: ALICE detector cut view with relevant detectors highlighted, adapted from [60].

The general detector layout is shown in Fig. 3.1. The detector subsystems relevant for the data analysis presented in this thesis are described in the following. The muon arm (items 11 to 15 in Fig. 3.1) is located at a pseudorapidity of -2.5 to -4.0. Positive and negative pseudorapidity are referred to as A-side and C-side, respectively. The overall tracking and PID capabilities are described in separate sections. Further information on the detector systems can be found in [60].

3.1.1. Central Barrel

The Inner Tracking System (ITS)

The Inner Tracking System (ITS) is built deploying a combination of silicon detector technologies. The detector is composed of six cylindrical detector layers which are located at radial positions ranging from 4 cm to 43 cm. The innermost two layers are the Silicon Pixel Detector (SPD). The first layer has an extended pseudorapidity coverage of $|\eta| < 1.98$ and the second one covers $|\eta| < 1.4$. The first and second layer are read out by $20(40) \times 20$ chips in the $(r\varphi)$ and z-direction. Each of these 1200 chips is responsible for several thousand detector cells and provides a FastOR trigger signal. This FastOR trigger signal is fired if at least one detector cell of a readout chip indicates a hit. These signals can be combined to more complex trigger signals, which are then sent to the Central Trigger Processor (CTP). Possible applications are, for example, multiplicity based triggers. The next two layers outwards in radial direction are made of silicon drift detector arrays (SDD) ranging from -0.9 to 0.9 in pseudorapidity. The two outermost layers are silicon strip detectors (SSD) covering $|\eta| < 0.97$. The SDD and SSD detectors together provide four $\mathrm{d}E/\mathrm{d}x$ samples for PID.

The main task of the ITS is to locate primary and secondary vertices and to contribute to the ALICE tracking capabilities. The ITS provides tracking in the dead zones of the TPC and standalone tracking for soft tracks below the p_{T}-threshold of the TPC. Additionally, it further constrains TPC tracks with the help of additional track points leading to an improved spatial and momentum resolution. Finally, it provides PID for particles at low momenta as discussed below.

Time-Projection Chamber (TPC)

The main tracking and particle identification device is the Time-Projection Chamber (TPC) located at a radial position from 0.85 m to 2.5 m and extending from -2.5 m to 2.5 m in z-direction. The total gas volume of $88\,\mathrm{m}^3$ is segmented in two halves by the central drift electrode. A top priority is the reduction of space-charge effects resulting from the expected highest multiplicity densities in heavy-ion collisions. Furthermore, the gas mixture is optimised for fast drift speed, low diffusion and minimal multiple scattering. The chosen mixture is Ne/CO_2/N_2 (85.7-9.5-4.8) [64], a so-called 'cold gas', which is highly sensitive to environmental conditions, such as temperature and pressure. The resulting drift time is about $90\,\mu$s. For a luminosity of $5 \cdot 10^{30}\,\mathrm{cm}^{-2}\mathrm{s}^{-1}$, corresponding to an inelastic proton-proton interaction rate of 350 kHz, tracks of up to 30 events overlap in the gas volume. The detector is read out with a maximum rate of 1 kHz using Multi-Wire Proportional Chambers (MWPCs) located at the end caps. The MWPCs are segmented 18-fold azimuthally and double in radial direction, with smaller pads at the inner chambers. The boundary regions of the readout chambers lead to dead zones in which particles cannot be detected. Overall, a maximum of 159 pad rows in radial direction can provide track points and $\mathrm{d}E/\mathrm{d}x$ information. The maximum rapidity for tracks traversing the whole detection volume is $|\eta| = 0.9$, while for a pseudorapidity of $0.9 < |\eta| < 1.5$ the track points decrease to one half.

The Time-of-Flight Detector (TOF)

Deploying multi-gap resistive-plate chambers (MRPCs), the Time-of-Flight detector (TOF) provides timing measurements with a resolution of $\sigma_t \approx 120\,\mathrm{ps}$ in proton-proton collisions depending on the accuracy of the collision-time determination. This timing information can be used for particle identification in the intermediate momentum range. Located at a radial position of 3.8 m, the detector covers a pseudorapidity range of $|\eta| < 0.9$. Furthermore, due to its fast electronics, the TOF detector can generate trigger signals, which for example can be based on a multiplicity condition or on a back-to-back coincidence in the detector.

3.1.2. Forward Detectors

The VZERO Detector

The VZERO detector is a forward scintillator hodoscope which consists of two subdetectors on the A- and C-side. Since the muon arm and its absorber are installed on the C-side, the VZERO detectors are not placed symmetrically with respect to the origin. While VZERO-A is located 3.4 m away, VZERO-C is at 0.9 m. The resulting pseudorapidity coverage is $2.8 < \eta < 5.1$ and $-3.7 < \eta < -1.7$, respectively. Both detectors consist of 32 scintillators each, which are arranged in four rings. The pseudorapidity coverage of the rings is shown in detail in Table 3.1. The readout of the scintillators is done with wavelength-shifting fibres and photomultiplier tubes. Besides being the main trigger detector, VZERO provides in addition centrality and event-plane information in heavy-ion collisions. Beam-gas background can be rejected by exploiting the arrival time of particles in an event.

Table 3.1.: Pseudorapidity acceptance of the individual V0 rings.

Ring	VZERO-A η_{max}/η_{min}	VZERO-C η_{max}/η_{min}
0	$5.1/4.5$	$-3.7/-3.2$
1	$4.5/3.9$	$-3.2/-2.7$
2	$3.9/3.4$	$-2.7/-2.2$
3	$3.4/2.8$	$-2.2/-1.7$

The Forward Multiplicity Detector (FMD)

The Forward Multiplicity Detector (FMD) is a highly granular silicon-strip detector covering the ranges $-3.4 < \eta < -1.7$ and $1.7 < \eta < 5.03$. The composition and location of its subdetectors are shown in Fig. 3.2. The inner and outer rings consist of 10 and 20 sectors each of which is subdivided into 512 and 256 strips, respectively. Its major task is the forward measurement of the multiplicity density $\mathrm{d}N/\mathrm{d}\eta$. Due to the substantial influence of secondaries, the FMD signal can be used for the $\mathrm{d}N/\mathrm{d}\eta$ determination only with software-based corrections. These secondaries originate from scatterings of primary particles with the material in between the interaction point and the detector. Another application of FMD is to obtain centrality and event-plane information. However, FMD has no trigger capabilities in contrast to VZERO, since its readout electronics is not suited to derive a fast trigger signal.

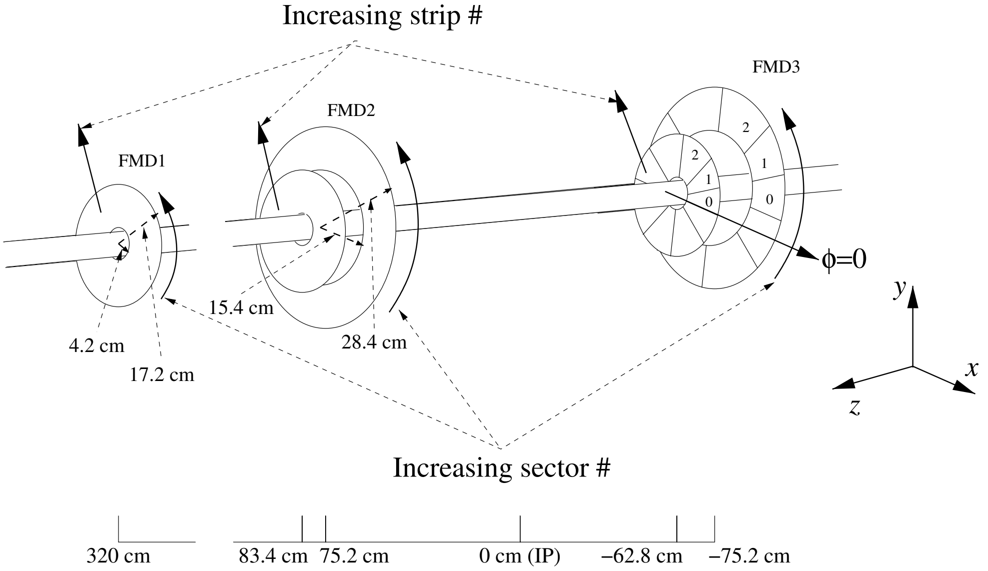

Figure 3.2.: Positions of the FMD subdetectors, taken from [60].

3.1.3. Pseudorapidity Coverage

Fig. 3.3 shows the pseudorapidity coverage of the detectors described above. These detectors are relevant in the analysis of central-diffractive double-gap events. Tracking and PID are restricted to the pseudorapidity range $|\eta| < 0.9$. Detectors outside of the central barrel do not have tracking capabilities, and thus cannot distinguish the signals originating from the primary or a secondary vertex, nor identify pileup, i.e. more than one interaction.

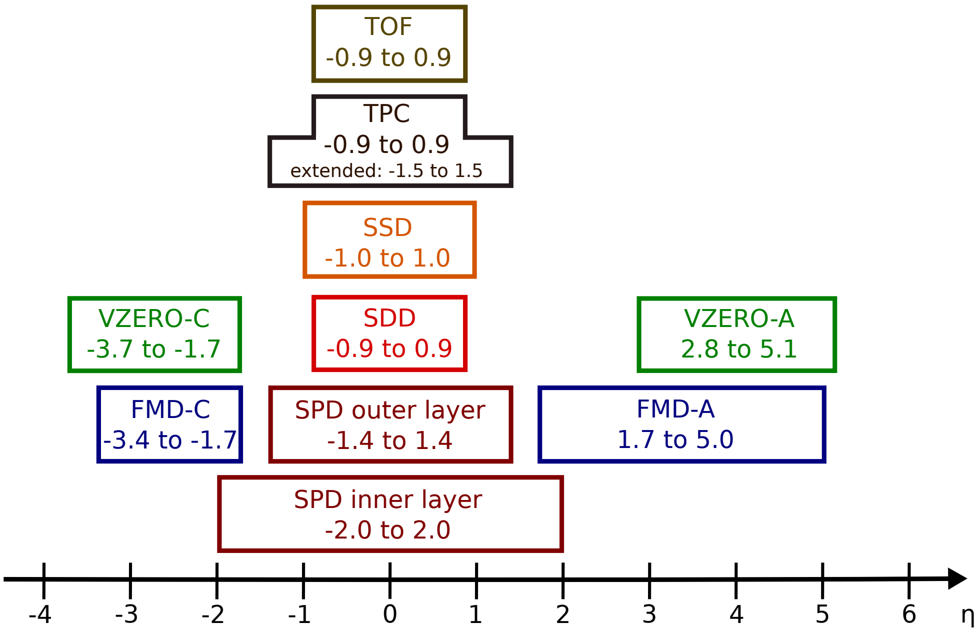

Figure 3.3.: Pseudorapidity coverage of the ALICE detectors used in the double-gap analysis.

3.2. Trigger System and Data Acquisition

In order to meet the bandwidth capabilities of the Data Acquisition system (DAQ), only a selection of the interactions can be read out. This selection is done online using the Central Trigger Processor (CTP) and optionally also the High-Level Trigger (HLT). The HLT can also optionally compress the event data.

The trigger signals in the CTP have to pass the three stages L0, L1 and L2. At L0 level, only simple trigger conditions can be applied due to the time window of 1.2 μs until the arrival at the detectors after an interaction. This includes for example the minimum-bias trigger which is fired if there is activity in at least one of the detector signals from VZERO at A- or C-side or the SPD FastOR trigger. In order to measure rare processes, the intermediate trigger level L1 can be used for more sophisticated hardware-based triggers, since it is distributed about 8 μs after the interaction. All events are currently accepted at L2-level. In addition, the past-future protection can be activated at this level. This trigger is fired about 100 μs after the interaction and results in the event readout from the front-end electronics. Because of the different trigger rates, a pre-scaling is available to balance relative rates of events in order to improve the statistics of very rare triggers. Depending on the operating mode, the event is then either directly passed on to the DAQ or further processed by the HLT.

The HLT can be used to improve the purity of triggered events. In the HLT, software-based partial event reconstruction is possible, which can provide, for example, track reconstruction and vertexing. Since not only the number of detector hits but also the vertex position and associated tracks can be determined by using the HLT, pileup vertices or events without primary vertex can be rejected. High-multiplicity events can therefore be distinguished from pileup and beam-background events.

3.3. Vertex and Track Reconstruction

During the reconstruction of ALICE data, the vertexing and tracking is carried out in several iterations. Due to their relevance for the double-gap analysis, the vertexing and tracking are described here in further detail.

The tracking is done using a Kalman filter [65, 66] which provides simultaneous track recognition and fitting. It starts with seeds in the TPC outer parts and proceeds radially inwards. If the algorithm successfully reaches the inner TPC wall, the flag ‘TPCin’ is set. The tracking is then continued within the ITS trying to prolong the track as closely as possible to the SPD vertex. This SPD vertex is determined separately from track points in the two SPD layers. After reaching the innermost ITS layer the flag ‘ITSin’ is set. Subsequently, the ITS standalone tracking starts based on the remaining ITS clusters from inside radially outwards to track particles which are too soft or decay within the ITS and hence do not reach the TPC. Tracks traversing the dead regions of the TPC can be found in this way. The standard tracking is then restarted from the innermost ITS layer outwards and, after successfully reaching the outer walls of the detectors, the corresponding flags ‘ITSout’, ‘TPCout’, ‘TRDout’ and ‘TOFout’ are set. Finally, the track is propagated inwards again and, after successfully passing the detectors, the track is flagged ‘TOFrefit’, ‘TRDrefit’, ‘TPCrefit’ and ‘ITSrefit’. These flags are part of the track-quality determination during the offline analysis. The track points of the TOF and the Transition Radiation Detector (TRD) are only used to match the PID information to a track and not for fitting. The tracking efficiency using ITS and TPC is about 80% at a momentum of 0.3 GeV/c, and increases to almost 90% for higher momenta [60]. The transverse momentum resolution for tracks fitted using ITS and TPC is about 1% for tracks up to a few GeV/c of momentum [60]. The transverse momentum resolution of the ITS standalone tracking is 6% in the range 200 − 800 MeV/c and the tracking is extended down to transverse momenta 80 MeV/c for pions [67]. After the track reconstruction is completed, the primary vertex is recalculated based on the track information.

3.4. Particle Identification (PID)

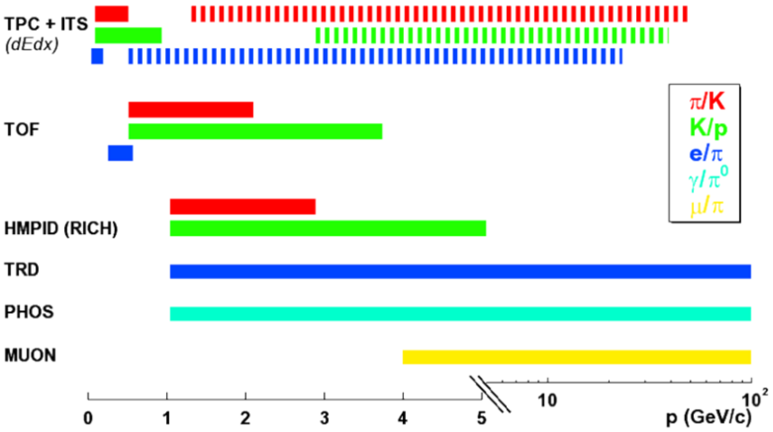

Figure 3.4.: PID separation capabilities of the different detectors in ALICE as a function of momentum, based on simulations described in [68].

As already mentioned above, ALICE exploits several methods to achieve Particle Identification (PID). An overview on the PID capabilities of the different involved detectors can be found in Fig. 3.4. Due to the low central-diffractive cross section of about 1% of the total cross section, the invariant-mass distribution is limited to a few GeV/c^2 in the presently available minimum-bias data sample. The use of TPC, ITS and TOF is hence sufficient for the PID determination of the corresponding tracks.

In Fig 3.5 the energy-loss dE/dx is shown as a function of the particle momentum. The black curves are splines interpolating the most likely energy loss as a function of the momentum for different particle species. Due to the crossing of these lines, there are momentum ranges, for example in the TPC at about 1 GeV/c for pions and kaons shown in Fig. 3.5b), where a PID decision is not possible. Depending on the purity requirements and the relative abundance, one can still use the PID information. Usually, all tracks within a range of $\pm 3\sigma$ of a spline are assigned to

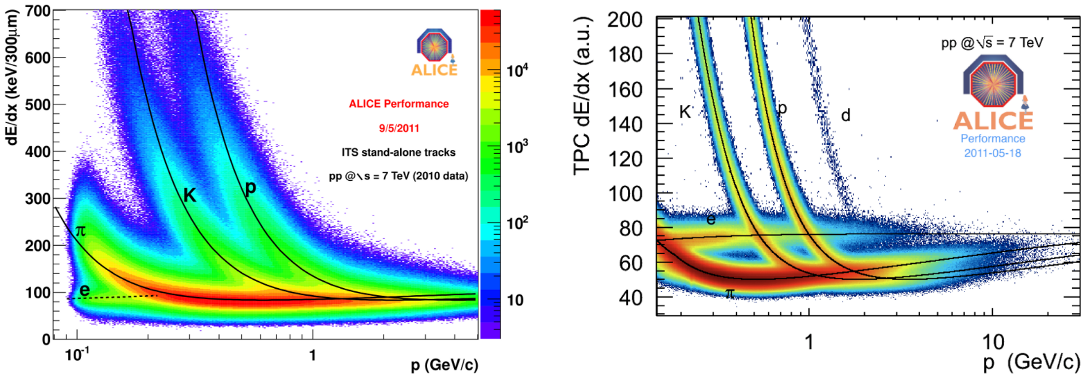

(a) (b)

Figure 3.5.: dE/dx spectrum of the ITS (left) and TPC (right) in proton-proton collisions at $\sqrt{s} = 7\,\text{TeV}$.

the particle type generating the spline. Here, σ is defined as

$$\sigma = \frac{\mathrm{d}E/\mathrm{d}x_{\text{measured}} - \mathrm{d}E/\mathrm{d}x_{\text{theo}}}{\sigma_{\mathrm{d}E/\mathrm{d}x}} \;, \tag{3.1}$$

with the resolution of the energy measurement $\sigma_{\mathrm{d}E/\mathrm{d}x}$. This resolution is about 5−7% depending on the track quality for the TPC [69]. The ITS reaches a resolution of 11% [60]. If one is interested in high purity or in a rare species like electrons, one needs to exclude the crossing areas. Exclusion cuts are difficult to correct for efficiency since the relative positions and the signal distributions have to be matched with a very high precision in the MC simulation of the detector. In order to access a momentum range affected by a crossing, a detector combination with complementary PID capabilities needs to used.

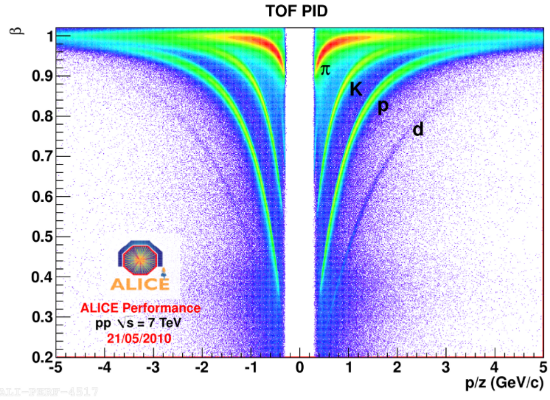

Figure 3.6.: TOF signal as a function of particle velocity β and momentum per charge.

In the momentum range up to about 450 MeV/c and 1 GeV/c, the ITS can provide 3σ-separation of pions from kaons and of kaons from protons. The TPC can unambiguously identify pions in the range of approximately 250 MeV/c to 800 MeV/c.

The TOF PID capability of measuring the velocity β as a function of the magnetic rigidity (proportional to momentum per charge) is complementary to the PID capability of ITS and TPC. TOF is able to separate kaons from pions at momenta of up to about 2.5 GeV/c, and protons from kaons up to 4.5 GeV/c, as presented in Fig. 3.6. However, the particles need a minimum momentum of about 300 MeV/c to be efficiently detected by TOF, which is a drawback as compared to the identification by TPC and ITS.

4. Analysis of Double-Gap Events

In this chapter, the analysis of double-gap events is discussed. This analysis concentrates on three topics. First, the cross section for events with double-gap topology is obtained. Second, the gap fraction is evaluated as a function of the multiplicity, and the influence of the multiplicity distribution on the gap fraction is analysed. Third, the two-track invariant-mass distributions in double-gap and no-gap events are compared.

4.1. Double-Gap Topology in ALICE

The double-gap topology is determined in several steps. First of all, central activity is required to be seen by a FastOR signal of the SPD within a pseudorapidity range of $-0.9 < \eta < 0.9$. The condition of a double-gap can be defined with the help of information from VZERO, FMD, SPD and TPC detectors.

4.1.1. VZERO Detector

The VZERO detector can provide a signal at L0-trigger level. Such a signal is available for both the A- and C-side, and is defined by the logical-OR of the 32 detector channels as described in Chapter 3. The signal of each of the 32 detector channels is read out for L2-accepted events, and an offline L0-signal can be reconstructed in the offline analysis. The VZERO trigger efficiency can therefore be monitored by comparing the values of the on- and offline L0-trigger bits. A straightforward definition of the rapidity gap spanning the range of VZERO is the requirement of absence of the VZERO offline L0-trigger bit. Due to the four-fold segmentation in pseudorapidity of the VZERO as discussed in Chapter 3, the gap size can be varied on both A- and C-side in steps of about half a pseudorapidity unit.

4.1.2. FMD Detector

The FMD detector does not provide a signal at L0-trigger level. In the offline analysis, however, trigger bits can be reconstructed indicating activity in any of the detector channels, similarly as in the VZERO detector. These reconstructed trigger bits allow a variation of the gap size on both A- and C-side due to the geometrical segmentation of the FMD.

4.1.3. SPD Detector

The SPD gap-condition is evaluated in the offline analysis based on the information from the SPD FastOR signals. As described in Chapter 3, the coverage of the SPD is $-2.0 < \eta < 2.0$ and $1.4 < \eta < 1.4$ for the inner and outer layer, respectively. This range is split in three sections. The forward ones at $0.9 < \eta < 2.0$ and $-2.0 < \eta < -0.9$ are used for the definition of A- and C-side gap, respectively, and the region $-0.9 < \eta < 0.9$ for the central activity. Due to the fact that the SPD FastOR consists of 1200 contributing chips, in principle also the size of these gaps can be varied. The two SPD layers are located at a radial distance of only 4 cm and 7 cm to the interaction point. Therefore they are both very sensitive to shifts of the vertex position in z-direction leading to a sizeable change in pseudorapidity coverage, which is discussed below.

4.1.4. TPC Detector

The use of the TPC information in the evaluation of pseudorapidity gaps has many aspects, and is therefore not as straightforward as the gap definition based on VZERO, FMD and SPD detector described above. The TPC information can contribute to the gap definition in the pseudorapidity range $|\eta| > 0.9$. This range is, in principle, covered by the SPD providing the FastOR for the definition of a gap. The addition of the TPC information can, however, cover the SPD regions which are dysfunctional due to dead or masked-out FastOR chips. The fraction of such dead or masked-out FastOR chips is, as presented below in Fig. 4.8, on the order of 25%. The TPC information can therefore substantially improve the purity of gaps. The possible improvement of the gap purity can be studied by analysing events which satisfy the gap conditions of VZERO, FMD and SPD as described above. Such events can contain tracks in the pseudorapidity ranges of $\eta > 0.9$ and $\eta < -0.9$ due to the SPD FastOR efficiency of about 75%, described below. The Distance of Closest Approach (DCA) distribution of such tracks to the primary vertex is shown in Fig. 4.1 for both the A- and C-side of ALICE. The distributions for both sides clearly peak at the origin due to tracks originating from the primary vertex. The continuum extending to large DCA values in transverse and longitudinal directions is generated by background tracks which do not originate from the event vertex. The use of the tracks shown in Fig. 4.1 has to be limited therefore to those tracks which originate from the event vertex. The canonical choice to select primary tracks in ALICE for proton-proton data in 2010 is a maximum DCA_z of 2 cm. This is also approximately the value at which the two DCA distributions shown in Fig.4.1 start to differ. A value of 0.1 cm is chosen for DCA_{xy}, the distance in the transverse plane. This value is compatible with the cut applied to select low-momentum primaries with ITS-TPC track cuts. The different cuts are described in detail below.

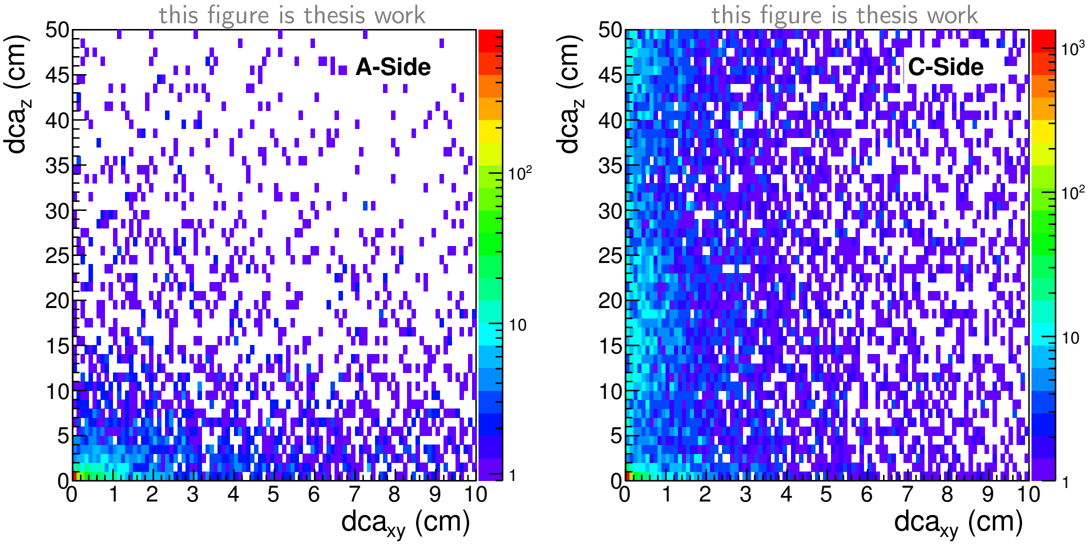

Figure 4.1.: DCA$_z$ vs. DCA$_{xy}$ distribution of tracks destroying the TPC double gap on either A-side (left) or C-side (right) in events with a VZERO-FMD-SPD double gap.

In Fig. 4.1 the distributions of A- and C-side show clear differences. On the A-side, the width of the DCA distribution is on the order of 1 cm in both the transverse and longitudinal direction. On the C-side, the width of the transverse distribution is also about 1 cm. However, the longitudinal DCA distribution on the C-side extends to values as large as 50 cm. A possible origin for these large values is the absorber of the muon arm. Tracks which have to cross the muon absorber on the C-side traverse a substantial amount of material. The associated multiple scattering and energy loss straggling introduce a considerable worsening of the resolution in the reconstruction of the tracks. In addition, hadronic interactions of primaries and background particles in the muon absorber lead to an enhanced production of secondaries. The material budget is much lower on the A-side and therefore less secondaries are expected.

Furthermore, ALICE is not designed for tracking outside $|\eta| < 0.9$. This extended range can only be used with a reduced track length in the TPC, and with a reduced number of ITS track points. As a consequence, the tracking efficiency is decreasing with increasing absolute values of the pseudorapidity. However, for the majority of the physics analyses, an efficiency flat in pseudorapidity is needed. In these analyses, tracking is only used within the range $|\eta| < 0.9$. Consequently, the range outside $-0.9 < \eta < 0.9$ is not as well understood as the central range.

4.1.5. Detector Combinations

In the following, different combinations of the detectors described above are used for the gap definition. These combinations are VZERO standalone, VZERO-FMD, VZERO-FMD-SPD and VZERO-FMD-SPD-TPC. In order to clearly state the corresponding gap type, all figures involving gap conditions contain a little drawing as shown in Fig. 4.2 for the example of the VZERO double gap. It indicates the positioning of the central activity (blue), the gaps (white), and the pseudorapidity range for which there is no information (grey) for the VZERO double-gap.

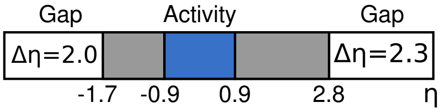

Figure 4.2.: Gap Indicator for the VZERO double gap.

4.1.6. Influence of the z-Vertex Position on the Pseudorapidity Coverage

As the interactions are not located exactly at the origin of the detector coordinate system, but spread within the so-called interaction diamond, the influence of the vertex position on the detector pseudorapidity has to be taken into account. In Fig. 4.3 the vertex position distribution in x, y and z of minimum-bias events is shown. While the interactions are displaced a few millimetres and spread over fractions of millimetres in x and y, the range in z is many centimetres. The standard z-vertex cut in ALICE restricts the vertex position to ±10 cm, since this range exhibits best coverage for tracking within the pseudorapidity range of $-0.9 < \eta < 0.9$. For the purposes of this analysis, however, a continuous coverage also in the more

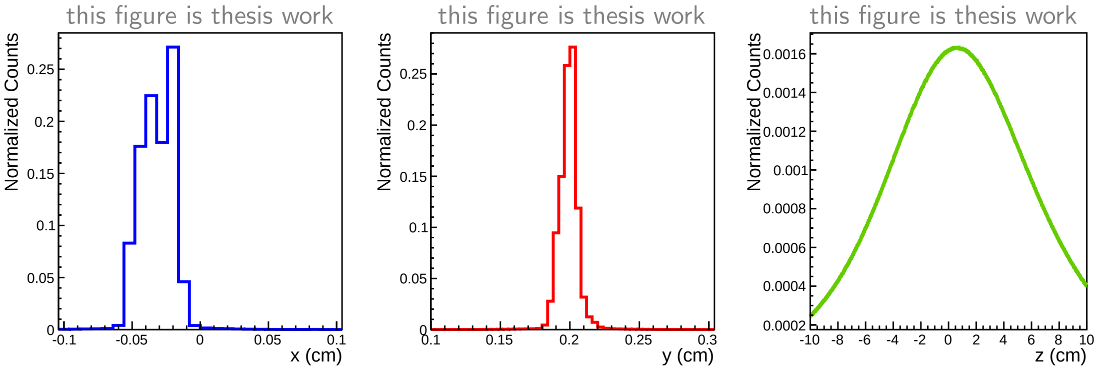

Figure 4.3.: Vertex position distributions in x (left), y (centre) and z (right).

forward pseudorapidity range is crucial. The pseudorapidity coverage of the different detector systems described above was therefore studied as a function of the z-vertex position as shown in Fig. 4.4.

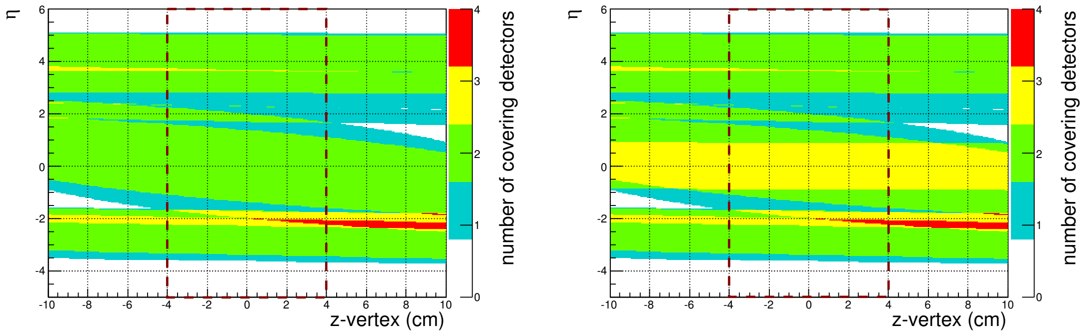

(a) VZERO, FMD and SPD

(b) VZERO, FMD, SPD and TPC

Figure 4.4.: Pseudorapidity coverage as a function of the vertex-z position for the combination of VZERO, FMD and SPD (left) as well as VZERO, FMD, SPD and TPC (right); colours indicate the number of detectors covering a pseudorapidity.

The influence of the vertex position is most striking for the innermost SPD layer, due to its small radial distance of only 3.9 cm. There is no noticeable influence on the TPC, whose outside edges are at a radial distance of 2.58 m. For a continuous detector coverage in pseudorapidity, a z-vertex cut of ± 4 cm is applied.

A large fraction of the pseudorapidity range is covered by two or more detectors, and inefficiencies of single detectors can therefore be compensated. However, the double coverage can lead to an increased probability of accidentally destroyed gaps due to noise and secondary particle production.

4.2. Transverse Momentum Threshold of the Gap-Tagging Detectors

As the quality of the gaps and also the detection of the central activity is crucial for this analysis, the single-track efficiency at a given transverse momentum is determined by a Monte Carlo simulation. The single-track efficiency is crucial, since for this analysis it is only necessary to know whether a particle traversed the detector. This simulation is necessary, as the threshold is mainly determined by the energy loss of the particles. The geometrical threshold can be calculated from the radial position of the detector and the track curvature in the solenoidal magnetic field. A pion, for example, needs to have a transverse momentum $p_{\mathrm{T}} > 3\,\mathrm{MeV}/c$ in order to reach the first layer of the SPD, which is located at a radial distance $r = 3.9\,\mathrm{cm}$.

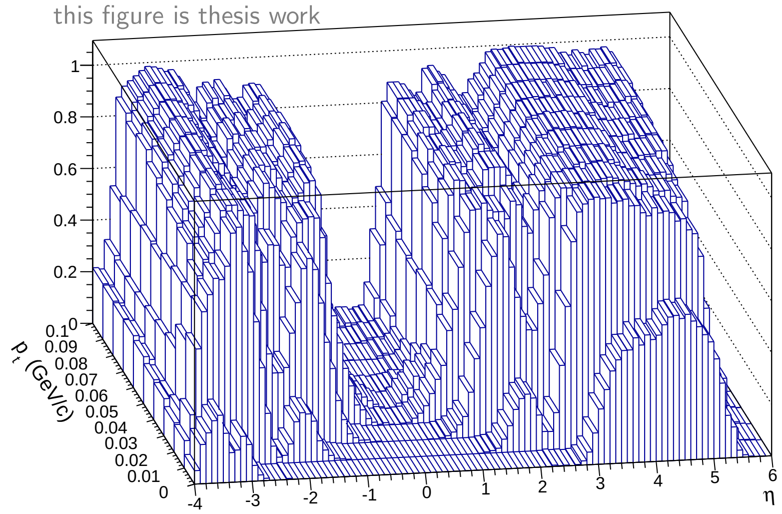

Figure 4.5.: Single track efficiency for gap-tagging detectors.

On the other hand, a p_{T}-threshold can be estimated by considering the energy loss $\mathrm{d}E/\mathrm{d}x$ in the beam pipe which consists of 0.8 mm Beryllium. The minimal kinetic energy of a proton to cross this amount of material is about 5 MeV [70]. In first order, the energy loss of pions and protons are equal, as it is dominated by the electromagnetic interaction of the electric charge with the electrons of the beam-pipe material. The resulting p_{T}-threshold for pions to traverse the beam pipe is about 40 MeV/c at $\eta = 0$. This value is much larger than the value derived from the track curvature. Furthermore, the amount of material to be crossed is highly dependent on the pseudorapidity of the particle. The p_{T}-threshold is therefore totally dominated by the energy loss mechanisms in the traversed material.

The simulation for the single-track gap efficiency contains the ITS, FMD and VZERO as well as the surrounding infrastructure like the beam pipe and support structures. All outer detectors and the active parts of the muon arm are disabled to keep the computing time reasonable. Every simulated event contains a single pion track. The choice of pions is justified, as the analysis focuses on hadronic events in which pions are the most abundant particles. The simulation contains a total of one million events uniformly distributed in pseudorapidity and p_{T}. It is done in 100 bins for the pseudorapidity interval of $-4 < \eta < 6$ and in 10 bins spanning a p_{T}-range of 0 to 100 MeV/c. In Fig. 4.5 the single track efficiency is shown as function of pseudorapidity η and transverse momentum p_{T}. The average detection probability in the p_{T}-range of 30 to 100 MeV/c is found to be 87% and 79% at A-side and C-side, respectively. The 50% efficiency threshold is reached at a transverse momentum of about 17 MeV/c. This threshold is significantly lower than the threshold of 200 MeV/c used in the ATLAS rapidity-gap cross section measurement [71].

Although the p_{T}-thresholds of the involved detectors are rather low, one has to keep in mind that for pseudorapidity values covered by VZERO and FMD the total momentum can be up to two orders of magnitude larger than the transverse momentum. This leads to a better acceptance and efficiency at low p_T, because the influence of the energy loss is reduced.

4.3. Dataset

The analysis carried out within this thesis is based on data from proton-proton collisions at a centre-of-mass energy of 7 TeV measured by the ALICE experiment. There are two datasets, one minimum-bias dataset from 2010 and a triggered dataset from 2011. The results shown below are based on the minimum-bias dataset.

The minimum-bias data were taken with an interaction trigger consisting of at least a single hit in VZERO-A, VZERO-C or the SPD FastOR trigger. This trigger is called $\mathrm{MB}_{\mathrm{OR}}$. The minimum-bias dataset was taken in four different periods called LHC10b, LHC10c, LHC10d and LHC10e. Technical stops and LHC machine-development runs are scheduled in between the data-taking periods. The data from the different periods are therefore analysed separately in order to identify possible systematic effects, which are due to changes in detector or beam conditions.

In addition to the $\mathrm{MB}_{\mathrm{OR}}$ condition, a trigger $\mathrm{MB}_{\mathrm{AND}}$ exists. This trigger is defined by a hit in each of VZERO-A *and* VZERO-C. The $\mathrm{MB}_{\mathrm{AND}}$ trigger is used for the luminosity determination using van-der-Meer scans.

Double-gap events constitute only a small fraction of minimum-bias data, and the analysis of double-gap events from minimum-bias triggered data does therefore not allow to accumulate a large statistics sample. Hence in 2011 a double-gap trigger was introduced. This trigger, called CDG5-I, imposes the double-gap condition at L0-level, using VZERO-A and VZERO-C for the detection of gaps and the SPD FastOR trigger and a TOF trigger bit for the central activity. A further detailed discussion can be found in Appendix A.

In addition to the experimentally measured data, also Monte Carlo data samples are analysed in this thesis. These MC data sets are anchored to the detector working conditions during the data taking. In ALICE, the two generators PHOJET [26] and PYTHIA6 [72] are used for the simulation of proton-proton collisions. PHOJET contains central diffraction within its standard minimum-bias tune, which is described in [73]. This model of central-diffraction contains only non-resonant particle production. In PYTHIA, central-diffraction is introduced in the recently released version 8.170 [27], which however was not available at the time of this analysis. Furthermore, a small sample is generated with tuned versions of these generators. During this tuning, the description of single- and double-diffractive dissociation was adjusted to the data measured by ALICE. The central-diffraction channel is deactivated in the tune. A detailed discussion of these tuning efforts is given in the ALICE publication on the inelastic cross-section measurement [25].

4.4. Run Selection

First of all, only runs with global quality flag 1 from the run condition table in MonALISA [74] are selected. In order to get rid of runs which show problematic behaviour in the relevant gap detectors, a method based on the gap fraction is developed. The gap status of the three gap-tagging detectors is evaluated for every event and stored in a histogram. These gap fractions are then extracted run-wise for double-gap events in VZERO, FMD and SPD as well as the combinations VZERO-FMD and VZERO-FMD-SPD and compared within a run period. An iterative algorithm determines the average and removes all outliers outside 3σ of the mean within a run period. This iteration is repeated until the mean value is stable. The run is only selected when the gap-fraction for every single detector and for all detector combinations are found to be within a range of 3σ of the respective period mean. The resulting gap fractions with the corresponding 3σ-ranges are shown in Fig. 4.6 and Fig. 4.7. Furthermore, a small fraction of runs is excluded, for which an inconsistency of active SPD FastOR channels in the data and from the Offline Condition DataBase in the following abbreviated as (OCDB) is found.

The run selection criteria for the data described above are also applied to the existing Monte Carlo data samples. Of particular interest is the output of the generators which are tuned to match the analysed single- and double-diffractive cross sections in ALICE. However, only a limited sample of such MC data is available, and thus the above-mentioned selection cannot be used.

A summary on the datasets and the corresponding runs can be found in Appendix C.

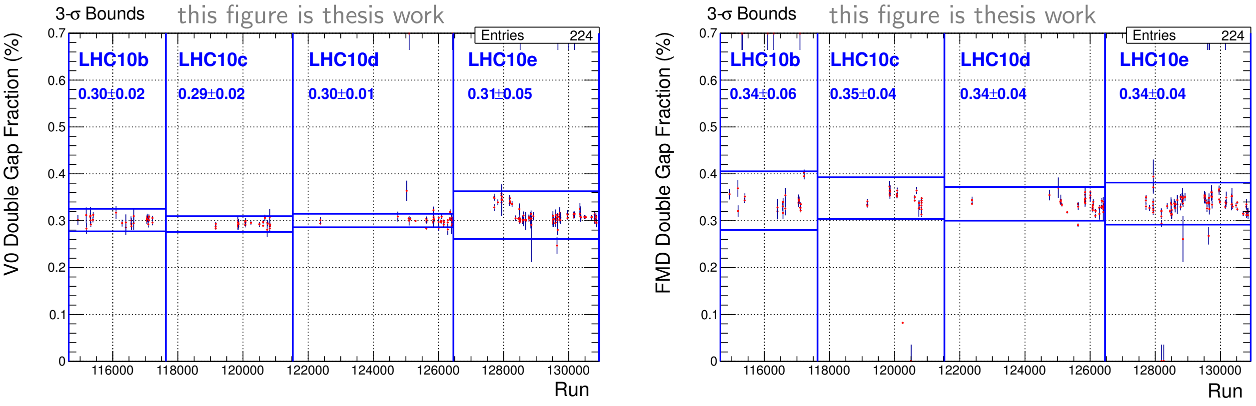

(a) VZERO gap fraction

(b) FMD gap fraction

Figure 4.6.: Gap fraction of the detectors involved in the analysis.

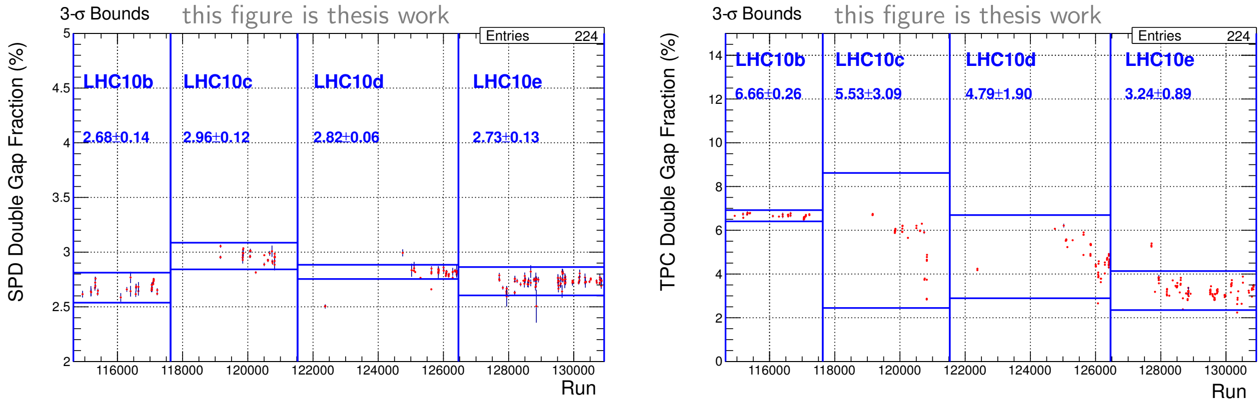

(a) SPD gap fraction (b) TPC gap fraction

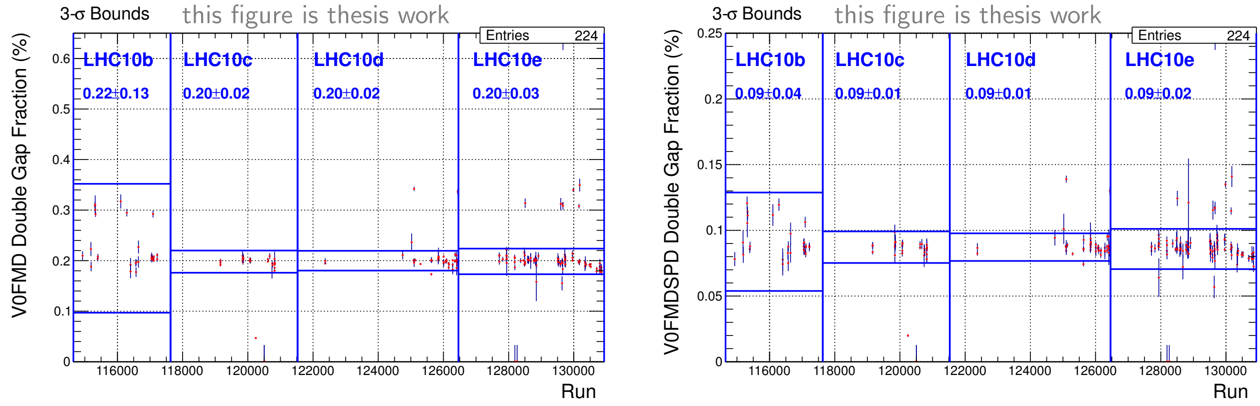

(c) VZERO-FMD gap fraction (d) VZERO-FMD-SPD gap fraction

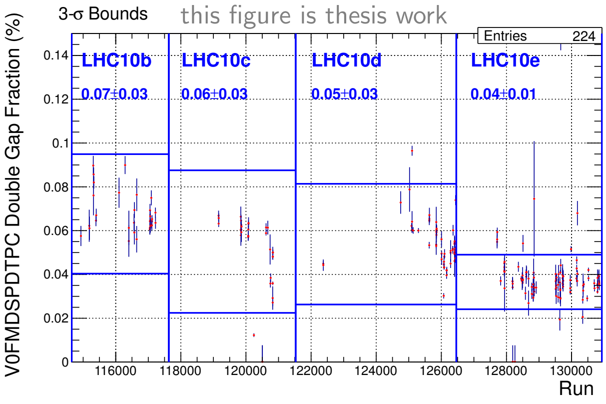

(e) VZERO-FMD-SPD-TPC gap fraction

Figure 4.7.: Gap fraction of the detectors involved in the analysis (continued).

4.5. Event Selection

First, the standard physics selection is applied which removes beam-induced background and selects minimum-bias triggered events. A vertex from either tracks or SPD tracklets is required. Furthermore, this vertex is required to originate from a z-position within $\pm 10\,\mathrm{cm}$ and $\pm 4\,\mathrm{cm}$ for the invariant-mass study and the cross-section analysis, respectively. The restriction to the interaction diamond in x and y is done implicitly during the reconstruction. Furthermore, pileup is removed by using additional vertices found with the help of SPD tracklets. The fraction of events with pileup is found to be 2.3%.

For the invariant-mass distributions, further restrictions are studied. These additional conditions contain a z-cut of $\pm 4\,\mathrm{cm}$ and a cut on the maximum distance of the vertices obtained using global tracks and SPD tracklets. A detailed discussion of the cuts is given in the description of the two-body analysis in Chapter 4.8.

4.6. Double-Gap Cross Section

The quantitative observable accessed most easily is the inclusive double-gap cross section. In the analysis, the integrated luminosity $\mathcal{L} = \int L \; \mathrm{d}t$ is determined for every run. The number N_i of events of type i is related to the corresponding cross section σ_i by

$$N_i = \mathcal{L} \cdot \sigma_i \; . \tag{4.1}$$

In ALICE the minimum-bias cross section $\sigma_{\mathrm{MBand}} = 54.3 \pm 1.9\,\mathrm{mb}$ is determined by a van-der-Meer scan [25]. The integrated luminosity in a run can therefore be calculated with the information of this minimum-bias cross section σ_{MBand} in conjunction with the number of $\mathrm{MB}_{\mathrm{AND}}$ events N_{MBand}, as depicted in Eq. 4.2.

$$\mathcal{L} = \int L \; \mathrm{d}t = \frac{N_{\mathrm{MBand}}}{\sigma_{\mathrm{MBand}}} \tag{4.2}$$

The number of *measured* double-gap events N'_{DG} in a run of integrated luminosity $\mathcal{L}$ is related to the double-gap cross section σ_{DG} by

$$N'_{DG} = \epsilon \cdot N_{DG} = \epsilon \cdot \mathcal{L} \cdot \sigma_{DG} \; . \tag{4.3}$$

In Eq. 4.3, a factor ϵ is included to account for the efficiency of identifying double-gap events. N_{DG} is the *true* number of double-gap events in the corresponding sample. The different contributions for the efficiency ϵ are discussed in Chapter 4.6.1. Using Eq. 4.2 and 4.3 the double-gap cross section σ_{DG} is given by

$$\sigma_{DG} = N'_{DG} \cdot \frac{1}{\epsilon} \cdot \frac{1}{\mathcal{L}} = \frac{N'_{DG}}{N_{\mathrm{MBand}}} \cdot \sigma_{\mathrm{MBand}} \cdot \frac{1}{\epsilon} \; . \tag{4.4}$$

4.6.1. Systematic Biases and Uncertainty Estimation

In the following, the statistical uncertainty of the double-gap cross section defined by Eq. 4.4 is discussed, and the origins of various systematic biases are identified.

The efficiency factor ϵ of the gap determination can in principle be obtained from MC data, however this is a rather involved analysis. Due to possible decays, scattering and energy loss in the detectors, it is incorrect to do the gap determination on MC truth information on primary tracks at the vertex. Instead, it has to be done at the stage of the individual detectors taking secondary particles into account as well. Furthermore, for a reliable determination of ϵ, the material as well as the detector response and noise has to be understood and has to be simulated very precisely. An alternative method to determine the gap-efficiency and other systematic biases is based on data-driven studies. These studies are more straightforward to do and allow to disentangle the possible contributions more easily.

Luminosity Determination

First of all, the minimum-bias cross section σ_{MBand} has a measurement uncertainty of 3.5% [25]. Furthermore, the statistical error of N_{MBand} is negligible since N_{MBand} is much larger than N_{DG}.

Event Selection

The event selection itself should not introduce a bias, since only the position of the interaction is restricted. However, there is a fraction of events without a reconstructed vertex. These events amount to about 9% of the events after physics selection. These events are most-likely due to beam-gas or low-mass single- or double-diffractive dissociation interactions. While beam-gas and single-diffractive dissociation interactions are unlikely to cause an $\mathrm{MB}_{\mathrm{AND}}$ trigger, it is more likely for double-diffractive dissociation interactions. Comparing the fraction of events with coincident activity in VZERO-A and VZERO-C ($\mathrm{MB}_{\mathrm{AND}}$ triggers) before and after event selection cuts including pileup rejection, this fraction is enhanced from about 84% to 90%. The change of the relative abundance by 6% of $\mathrm{MB}_{\mathrm{AND}}$ events provides an estimate for the error introduced by the event selection. In order to reduce this error, one can estimate the fraction of physics events for which the vertexing is not successful and obtain the vertex distribution from the kinematics truth of the MC generator. Using the vertexing efficiency and the distribution of the vertices, the amount of physics events without a proper vertex can be determined. In summary, the event selection biases the ratio of ${}^{N'_{DG}}/_{N_{\mathrm{MBand}}}$ by 6%.

Probability to Miss the Central Activity

Due to the fact that the acceptance as well as the efficiency are not perfect, the central activity can be missed. This leads to a reduced efficiency ϵ smaller than one and therefore a systematic shift to a lower cross section. From OCDB and a data analysis done run-by-run, which is shown in Fig. 4.8, the efficiency contribution of the SPD FastOR signals is analysed. Runs are excluded which do not show the same number of active channels from both sources. The average efficiency is determined to be $75.4 \pm 2.1\%$ by weighting the FastOR efficiency of every run with its number of events. A double-gap topology event does not produce an $\mathrm{MB}_{\mathrm{OR}}$ trigger if none of its central tracks produces a FastOR signal. The corresponding probability can be estimated by re-binning the track multiplicity distribution into bins of even multiplicities. In central-diffractive events only even numbers of tracks are expected due to charge conservation. For each bin representing events with n tracks the probability $P_{\mathrm{FastOR}}(n)$ of not generating a FastOR response is given by

$$P_{\mathrm{FastOR}}(n) = (1 - \epsilon_{\mathrm{FastOR}})^n \tag{4.5}$$

with the efficiency of the FastOR $\epsilon_{\mathrm{FastOR}} = 0.75$. The probability of missing a double-gap event can subsequently be calculated by

$$P_{\mathrm{Miss\_Activity}} = \sum_n P_{\mathrm{DG}}^{\mathrm{Mult}}(n) \cdot P_{\mathrm{FastOR}}(n) \tag{4.6}$$

with $P_{\mathrm{DG}}^{\mathrm{Mult}}(n)$ the rebinned normalised track multiplicity distribution. The double-gap topology events have few tracks, hence it is enough to consider the first three bins representing track multiplicities of $n = 2$, 4 and 6. The resulting systematic bias consists in a decrease of the double-gap cross section σ_{DG} of 5.2%.

Probability to Miss a Particle in the Gaps

A minimum-bias event is wrongly identified as double-gap event if none of its tracks in the gap region is seen by the detectors. The probability $P_{\mathrm{No\_Signal}}(n)$ of an event with n tracks in the gap range not to be detected is

$$P_{\mathrm{No\_Signal}}(n) = (1 - \epsilon_{\mathrm{Single\_Track}})^n \; . \tag{4.7}$$

Here, $\epsilon_{\mathrm{Single\_Track}}$ represents the single-track efficiency of the gap-tagging detectors as discussed in Chapter 4.2. The probability $P_{\mathrm{No\_Signal}}$ of identifying a minimum-bias event as a double-gap event can be calculated by convoluting the normalised track multiplicity distribution $P_{\mathrm{Gap}}^{\mathrm{Mult}}(n)$ in the gap with the probability $P_{\mathrm{No\_Signal}}(n)$:

$$P_{\mathrm{No\_Signal}} = \sum_{n=1}^{\infty} P_{\mathrm{Gap}}^{\mathrm{Mult}}(n) P_{\mathrm{No\_Signal}}(n) \tag{4.8}$$

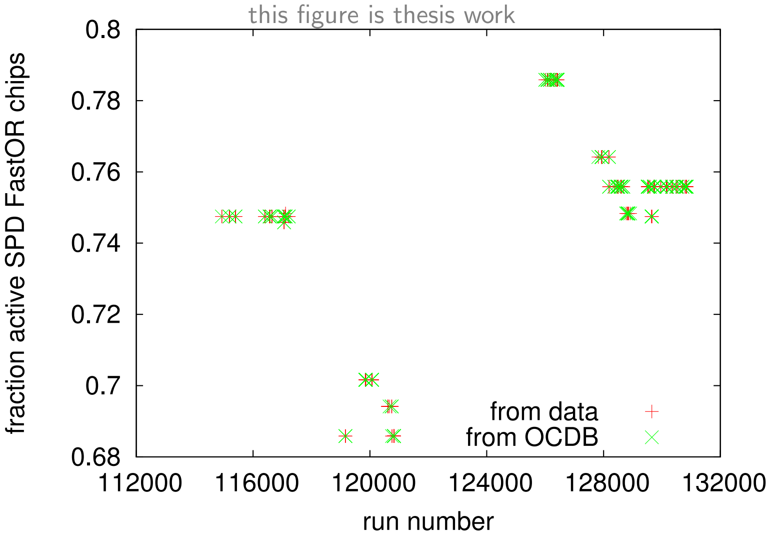

Figure 4.8.: Fraction of active SPD FastOR chips, inconsistent runs are excluded.

The track multiplicity distribution at the forward pseudorapidity ranges is not well known. An estimate for $P_{\mathrm{No\_Signal}}$ can, however, be calculated by using the well-known multiplicity distribution at mid-rapidity. The charged track density $\mathrm{d}N/\mathrm{d}\eta$ is measured to decrease from mid-rapidity to forward-rapidity. The distribution is however measured in a range of 1.8 units of rapidity, while the gap-size is 4.2 and 2.8 at A- and C-side. This estimate for $P_{\mathrm{No\_Signal}}$ of 4.9% represents therefore an upper bound.

Uncorrelated Systematic Contribution

The analysed data might be affected by systematic biases of unknown origin. This uncorrelated systematic error is estimated by using the spread of the cross-section period means $\sigma_{DG}(period)$ using Eq. 4.9 and the resulting error of the overall mean $\sigma_{DG}(overall)$ is then described by Eq. 4.10

$$\Delta\sigma_{DG}(period, uncorr.\ syst.) = \sqrt{\frac{1}{4-1}\sum_{i=1}^{4}\left[\sigma_{DG}(period) - \sigma_{DG}(year)\right]^2} \tag{4.9}$$

$$\Delta\sigma_{DG}(overall, uncorr.\ syst.) = \sqrt{\frac{1}{4}} \cdot \Delta\sigma_{DG}(period, uncorr.\ syst.) \tag{4.10}$$

Overview of the Systematic Errors

The different uncertainties and biases for the cross section measurement are summarised in Table 4.1. Adding the contributions linearly leads to an error of ±16%.

Table 4.1.: Systematic contributions to the cross-section uncertainty.

	Syst. Error
event selection	±6%
luminosity determination	±3.5%
central inefficiency	−5.2%
gap inefficiency	+4.9%
uncorrelated systematic error	±1.3%

4.6.2. Averaging and Statistical Error Calculation

The double-gap cross section is determined on a run-by-run basis after pileup rejection

$$\sigma_{DG}(run) = \frac{N'_{DG}}{\mathcal{L}}\frac{1}{\epsilon} = \frac{N'_{DG}}{N_{\mathrm{MBand}}} \cdot \sigma_{\mathrm{MBand}} \cdot \frac{1}{\epsilon} \tag{4.11}$$

with N'_{DG} and $\mathrm{N}_{\mathrm{MBand}}$ the numbers of double-gap and minimum-bias events, respectively, and σ_{MBand} the minimum-bias cross section as explained in Chapter 4.6. The statistical error on the double-gap cross section is

$$\Delta\sigma_{DG}(run) = \sqrt{\frac{N'_{DG} \cdot N_{\mathrm{MBand}} + {N'_{DG}}^2}{N^3_{\mathrm{MBand}}}} \cdot \sigma_{\mathrm{MBand}} \cdot \frac{1}{\epsilon} \tag{4.12}$$

The mean of a run-period p is then determined using a weighted average over all runs r in the corresponding period. The run-dependent weight is

$$w_r = {}^{1}\!/_{\Delta\sigma_{DG}(r)^2} \tag{4.13}$$

leading to

$$\sigma_{DG}(p) = \frac{\sum_r \sigma_{DG}(r) \cdot w_r}{\sum_r w_r} \ . \tag{4.14}$$

The corresponding statistical error is then calculated according to

$$\Delta\sigma_{DG}(p) = \sqrt{\frac{1}{\sum_r w_r}} \ . \tag{4.15}$$

In the same way as combining the runs to the period mean, the cross section averaged over all four data-taking periods $\sigma_{DG}(overall)$ is calculated.

4.6.3. Cross Section Derived from Data

Currently, the best gap condition is the VZERO-FMD-SPD double-gap, since it has the maximum gap size, although asymmetric, and is not as background dependent as gap conditions including TPC information. The resulting double-gap cross section is $44.0 \pm 0.1(stat.) \pm 7.0(syst.)\,\mu$b. In order to estimate detector-dependent effects, not only the VZERO-FMD-SPD double gap is analysed, but in addition the VZERO, the VZERO-FMD and the VZERO-FMD-SPD-TPC gap. The cross section for the VZERO-FMD-SPD-TPC double-gap is about 9% smaller than for the VZERO-FMD-SPD double-gap, although the gap sizes are the same. This reduction is due to tracks which are not seen by the SPD FastOR trigger and are detected by the TPC. This effect amounts for about 5% of the difference. In addition, the background sensitivity of the TPC leads to a further decrease of the cross section by about 4%.

The cross section is shown in Fig. 4.9 as a function of the run number with the period means as indicated by the red lines, the statistical error of the period mean indicated by the small red error bars and the uncorrelated systematic error estimated from the spread of the period means as filled red boxes. The overall mean and its corresponding errors are shown in blue.

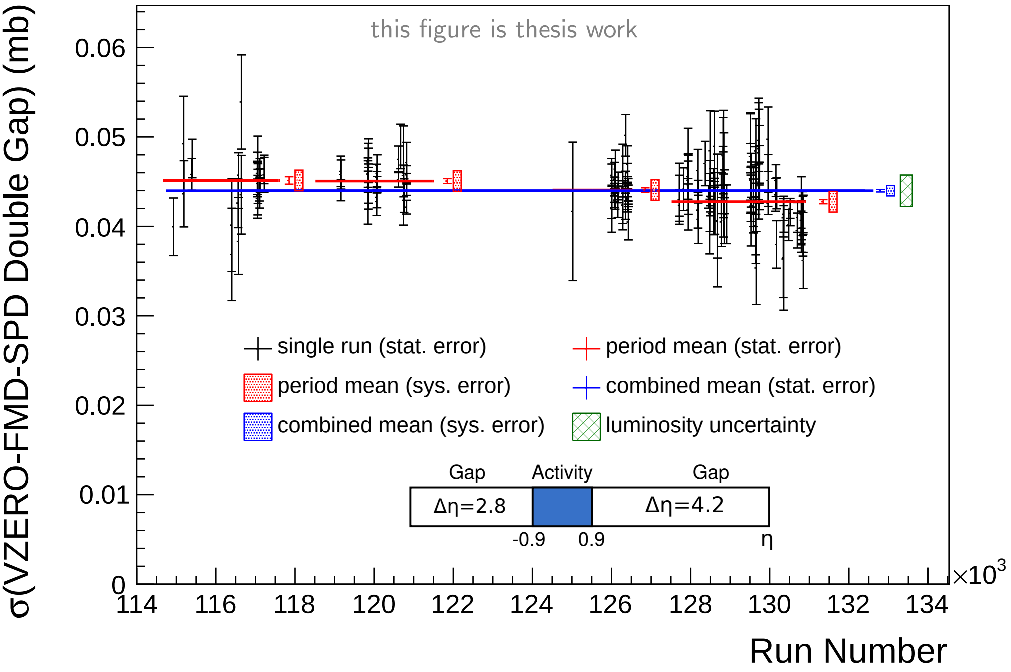

(a) VZERO-FMD-SPD double-gap cross section

Figure 4.9.: Double-gap cross section obtain from data, for events with VZERO-FMD-SPD gap.

Furthermore, the dependence of the cross section on μ, the average number of visible interactions per bunch-crossing, is plotted in Fig. 4.10. There is no significant dependence on μ, hence pileup effects are negligible.

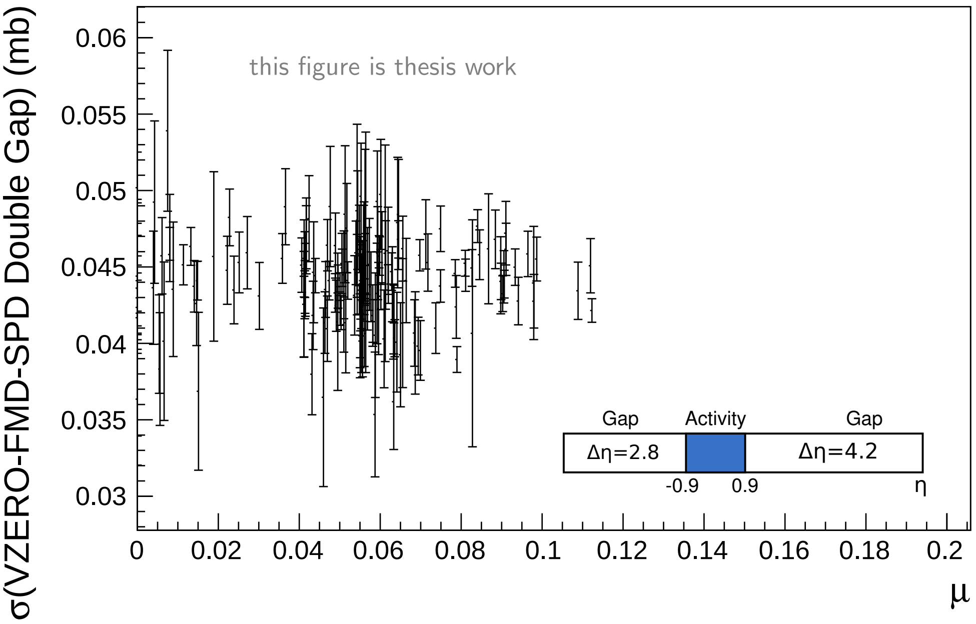

Figure 4.10.: VZERO-FMD-SPD double-gap cross section as a function of the mean number of visible interactions per bunch crossing μ.

Additionally, the dependence of the cross section on the instantaneous peak luminosity L is analysed. While the value of μ is obtained from reconstructed data, the value of L is determined from trigger input rates and machine information. Furthermore, μ is calculated per run, while L is only available per LHC fill. Since a fill can contain a series of runs, and the luminosity decreases over time, several runs are assigned to the same value of L, although the actual value is lower. The corresponding plot is shown in Fig. 4.11. There is no dependence of the double-gap cross section on the luminosity within the statistical errors of the individual runs.

4.6.4. Cross Sections Derived from MC

Background from Non-Diffractive and Diffractive-Dissociation Events

In order to estimate the fraction of the double-gap signal originating from diffractive dissociation and from hadronic inelastic events, the predictions of MC generators are studied. These generators do not contain central diffraction, and are tuned to match the data [25]. For this comparison, the tuned MC productions LHC11h{2,3,4}a

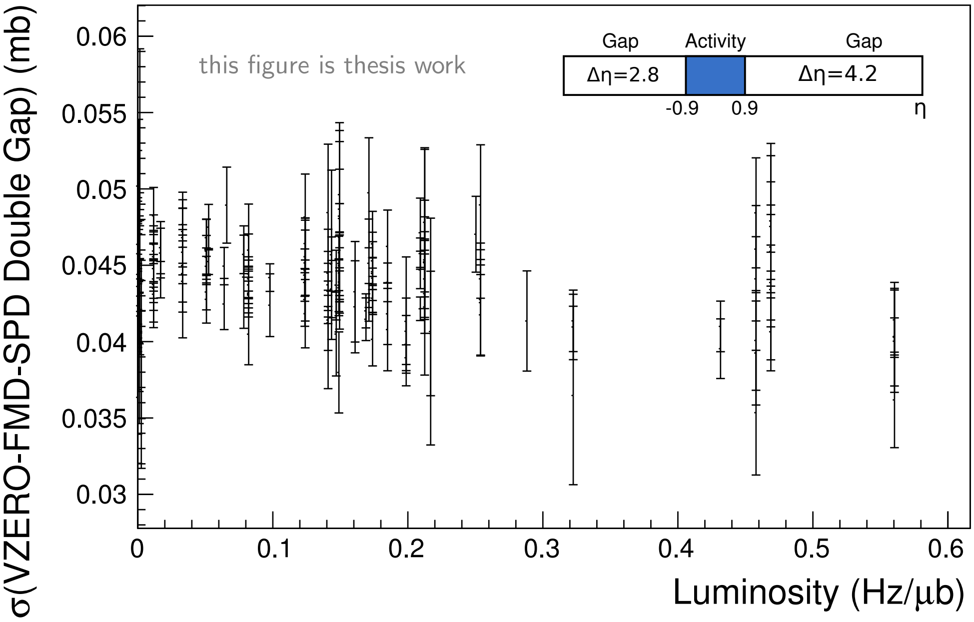

Figure 4.11.: VZERO-FMD-SPD double-gap cross section as function of the instantaneous peak luminosity L.

and LHC11h{2,3,4}b are used, which are generated with PYTHIA6 and PHOJET, respectively. The double-gap cross sections are derived by processing these MC productions by the identical analysis task as for the measured data. The cross section for tuned PYTHIA and tuned PHOJET are $20.0 \pm 0.4(stat.) \pm 3.2(syst.)$ μb and $3.32 \pm 0.17(stat.) \pm 0.53(syst.)$ μb, respectively, and are shown in Fig. 4.12. The processes accounting for this cross section seen in PYTHIA (PHOJET) are 25(22)% of non-diffractive origin, 60(47)% single-diffractive dissociation and 15(31)% from double-diffractive dissociation. Although both generators are tuned for diffractive dissociation, the resulting double-gap cross sections differ by about a factor of six. This discrepancy could result from the different multiplicity distribution in the forward region. In order to study these distributions, the FMD-forward-multiplicity task[1] is used. The corresponding $\mathrm{d}N/\mathrm{d}\eta$ distributions are shown in Fig. 4.13. The mean multiplicity in the two forward regions on A- and C-side ranging from 1.8 to 5.0 and -3.4 to -1.8 in pseudorapidity is calculated by using linear fits to these regions. The resulting values in the generators are significantly lower than what is obtained from the data. This matches with observations for mid-rapidity, which are already published [75].

The MC estimates for the contribution of diffractive-dissociation channels to the

---

[1] documentation and source code can be found at `https://twiki.cern.ch/twiki/bin/viewauth/ALICE/FMDHowToUseTheData` and `$ALICE_ROOT/PWGLF/FORWARD/analysis2/AddTaskForwarddNdeta.C`, respectively

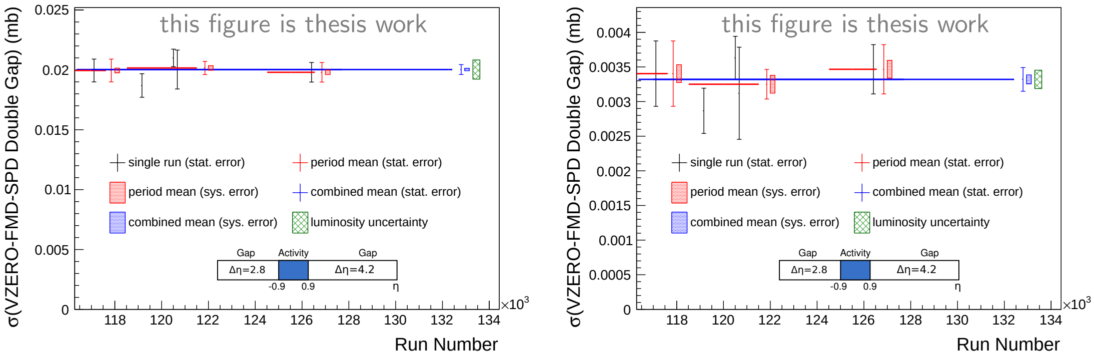

(a) tuned PYTHIA6

(b) tuned PHOJET

Figure 4.12.: Cross section for double-gap events using the VZERO-FMD-SPD double gap seen in MC data.

double-gap topology are therefore only meaningful if the predicted forward multiplicities are rescaled to match the measured data. Such a rescaling can be achieved by modelling the multiplicity distribution in the gap region by a negative binomial distribution $P(n, \langle n \rangle, k)$ as shown in Eq. 4.16.

$$P(n, \langle n \rangle, k) = \frac{\Gamma(k+n)}{\Gamma(k)\Gamma(n+1)} \left[\frac{\langle n \rangle}{k + \langle n \rangle} \right]^n \times \left[\frac{k}{k + \langle n \rangle} \right]^k \tag{4.16}$$

The negative binomial distribution $P(n, \langle n \rangle, k)$ denotes the probability of having n tracks within a rapidity interval which contains $\langle n \rangle$ tracks on average. The factor k is a parameter which is fitted to data and found to be $k \sim 1.3$ [76]. Within the binomial distribution, the occurrence of a gap is described by the probability of multiplicity zero. The probability of a double-gap is described by the product of the gap production probability on A- and C-side with assumption of independent gap formation on A- and C-side. Such an assumption is justified for the MC predictions which do not contain central diffraction.

$$P(\text{double gap}) = P(\text{gap A}) \times P(\text{gap C}) \tag{4.17}$$

The probability for multiplicity zero can be calculated for the average gap multiplicity $\langle n \rangle$ as measured in the data and seen in the generators. The ratio of these two numbers defines a rescaling factor. The number of double-gap events seen in the MC productions are subsequently multiplied by the rescaling factor. This rescaling results in a corrected cross section of 6.5 μb and 1.5 μb for PYTHIA6 and PHOJET, respectively. The results from these MC generator studies indicate that only about 10% of the double-gap cross section seen in the data can be understood to arise from known hadronic processes.

In addition, the double-gap fraction seen in the MC data strongly depends on the tuning for single- and double-diffractive dissociation which was done without considering central diffraction.

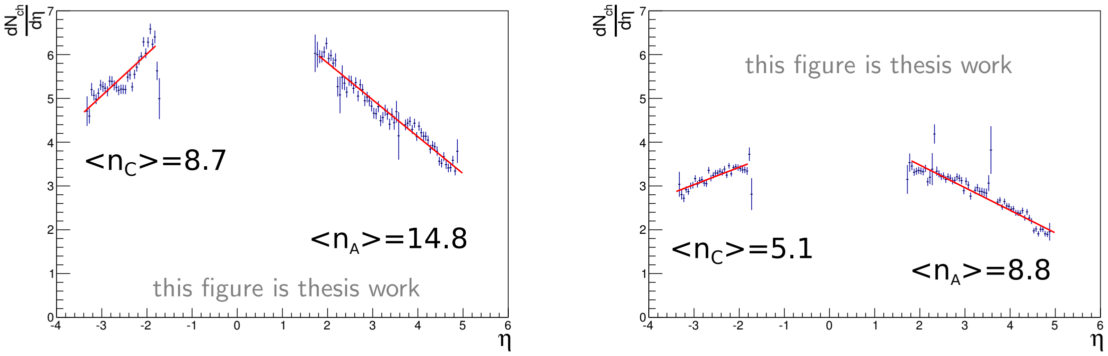

(a) data (b) tuned PYTHIA

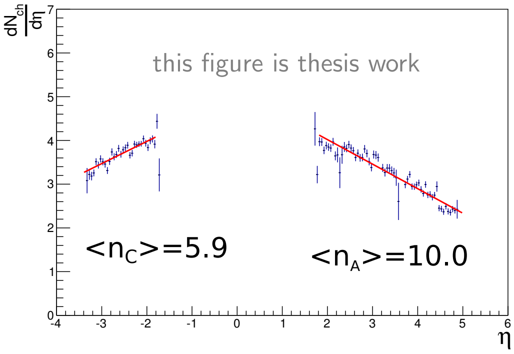

(c) tuned PHOJET

	$\langle n_{\mathrm{A}} \rangle$	$\langle n_{\mathrm{C}} \rangle$
Data	14.8	8.7
Tuned PYTHIA	8.8	5.1
Tuned PHOJET	10.0	5.9

Figure 4.13.: $\mathrm{d}N/\mathrm{d}\eta$ distributions for data, tuned PYTHIA and tuned PHOJET with an estimated mean multiplicity on A- and C-side.

For an improved understanding of the differences of the two MC generators, a more detailed study of the multiplicity distributions and the underlying mechanisms is needed. First of all, this study should include the overall $\mathrm{d}N/\mathrm{d}\eta$ distributions spanning the complete ALICE coverage in pseudorapidity. Moreover, the correlation of the multiplicity distribution within the gaps should be studied in the event generator output in order to check for possible correlations of gaps on A- and C-side. Furthermore, the distributions obtained with our special productions should be compared to current tunes by ATLAS and CMS.

Acceptance of the Double-Gap for Central Diffraction

In order to obtain the cross section for central diffraction from the double-gap topology condition, the acceptance of the double-gap topology has to be evaluated for both central diffractive events and for background processes. However, only one dataset with central diffraction based on PHOJET is available. Unfortunately, this data sample is not tuned to match the single- and double-diffractive contributions seen in the data and, additionally, the multiplicity distributions are not tuned. This dataset cannot be used to obtain a reliable signal-to-background ratio. Furthermore, the development of PHOJET is discontinued and it is not clear how well PHOJET describes the central-diffractive particle-production mechanisms, as no comparisons to other experiments exist. Nevertheless, the double-gap analysis is applied on a dataset which contains only central-diffractive PHOJET events. PHOJET predicts a central diffractive cross section of 1.3 mb. Surprisingly, only about 4 μb end up as VZERO-FMD-SPD double-gap events as shown in Table 4.2. The vertex is successfully reconstructed for only 72% of these events. Of those events, only 48% have a vertex within $|z| < 4$ cm. The double-gap topology based selection results in a further substantial reduction shown in Table 4.2. The double-gap cross section from data exceeds the corresponding PHOJET value by about an order of magnitude. A possible explanation for this could be a high probability for central diffraction with asymmetric gaps in PHOJET.

Table 4.2.: Statistics flow for the analysis of a pure central-diffractive event sample, generated using PHOJET.

Analysis Step (Event Class)	**#Events**	**Fraction**	**Corresponding Cross Section**
Input	489206		1.3 mb
w/ Vertex	350166	72%	
w/ Vertex within Range	169679	35%	
w/ VZERO-DG Double-Gap	14667	2.9%	38 μb
w/ VZERO-FMD-SPD Double Gap	1425	0.3%	3.9 μb

Another estimate of the signal-to-background ratio can be obtained by using the gap fractions for signal and minimum-bias events. Here, the gap fraction is defined as the ratio of the number of events satisfying the double-gap condition to the number of events within the primary-vertex range $|z| < 4$ cm. The VZERO-FMD-SPD gap fraction is $8.4 \cdot 10^{-3}$ for the central-diffractive PHOJET events. The corresponding value for the diffractive dissociation tuned PYTHIA6 is $1 \cdot 10^{-4}$. These numbers indicate that the definition of the VZERO-FMD-SPD gap condition results in an enhancement of central diffractive events by a factor of almost 100. However, taking into account that the inelastic cross section is about 73 mb and the central-diffractive in PHOJET 1.3 mb, only about 2% of the initially produced events are from central diffraction, leading to about 60% central-diffractive in the double-gap event sample. This value is, however, significantly lower than the $\sim$ 90% estimated in the cross section analysis. The reason for this difference is the insufficient description of the data by the MC generators.

4.7. Gap-Fraction Multiplicity Dependence

As mentioned above in Chapter 4.6.4, the multiplicity distribution influences the gap probability. The gap fraction within a multiplicity bin is an important observable which can be compared to the predictions of models. For this analysis, the full double-gap using VZERO, FMD, SPD and the TPC is used.

4.7.1. Track Selection

While the cross section analysis is done totally inclusive and multiplicity-independent, this study of the gap fraction and the invariant-mass study presented in Chapter 4.8 is done for two-track events. The selection of good tracks is based on track points from ITS and TPC by using the following selection criteria:

1. track within $|\eta| < 0.9$
2. at least 70 TPC clusters
3. χ^2 per TPC cluster smaller than 4
4. no kink daughters, i.e. no daughter tracks from leptonic kaon and pion decays
5. TPCrefit flag (see Chapter 3.3)
6. ITSrefit flag (see Chapter 3.3)
7. ITS clusters: kSPD, kAny, i.e. a hit in at least one SPD layer
8. maximum DCA to vertex in xy-plane as function of p_T: $0.0182 + 0.0350/p_\mathrm{T}^{1.01}$, distance in cm, p_T in GeV/c
9. DCA to z-Vertex smaller than 2 cm

These tracks are called 'normal' tracks in the following discussion.

In order to become sensitive to soft tracks, ITS standalone tracks are defined, in addition to the combined ITS-TPC tracks. These tracks, henceforth referred to as soft tracks, are selected with the following cuts:

1. $|\eta| < 0.9$
2. ITSstandalone flag, i.e. no track in TPC that could be matched
3. ITSrefit flag (see Chapter 3.3)
4. at least 4 ITS clusters
5. one SPD hit
6. ITS-χ^2 smaller than 1

7. maximum DCA to vertex in xy-plane as function of p_T: $0.0595 + 0.0182/p_\mathrm{T}^{1.55}$, distance in cm, p_T in GeV$/c$

Tracks which have ITS and TPC clusters are additionally reconstructed by the ALICE software using their ITS track points only. These tracks are called 'ITS pure standalone' tracks. From the viewpoint of this analysis, these tracks contain redundant information, and are hence not used. The remaining tracks do not fulfil the quality requirements above. However, these tracks indicate that the corresponding event is not fully detected. Such an event should hence be excluded. Furthermore, this concept is extended to ITS tracklets which are not assigned to tracks. Tracklets are based on clusters in the two ITS SPD layers and their information is used to reconstruct tracks.

From here on, the ensemble of normal and soft tracks is referred to as combined tracks. The possible improvement in multiplicity response of combined as compared to normal tracks is studied with a subsample of the PYTHIA6 MC sample LHC10f6a. The reconstructed multiplicity is shown in Fig. 4.14 for combined tracks (left) and for normal tracks (right). It is apparent that the response function is closer to the diagonal for the combined tracks. Since the multiplicity response is not perfect, an unfolding should be applied to all multiplicity-dependent quantities. As this unfolding is not yet implemented in this analysis, in the following only the uncorrected raw multiplicity values are used. Furthermore, the single-track p_T-threshold is reduced when soft tracks are introduced. This can be seen in Fig. 4.15, which shows the p_T-distribution for two track events, for the combined tracks (red) and the normal tracks (blue).

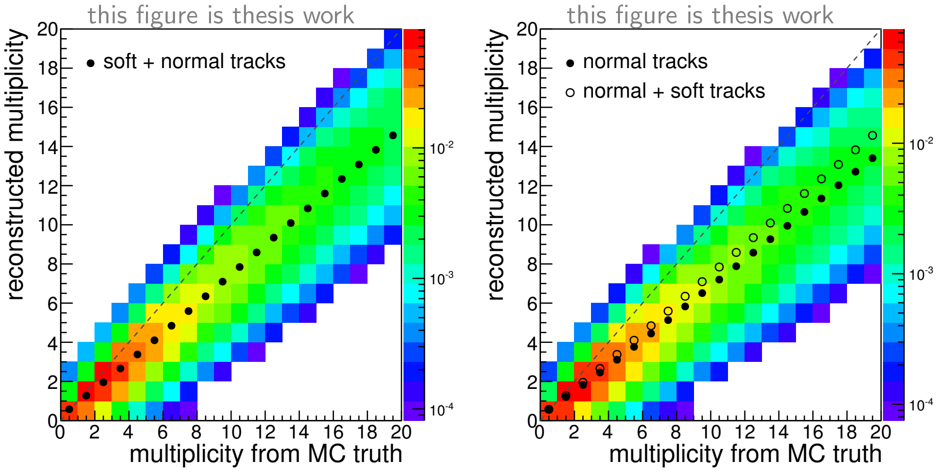

Figure 4.14.: Reconstructed multiplicity as function of the true number of charged primary tracks, response using combined track cuts (left) and normal tracks only (right).

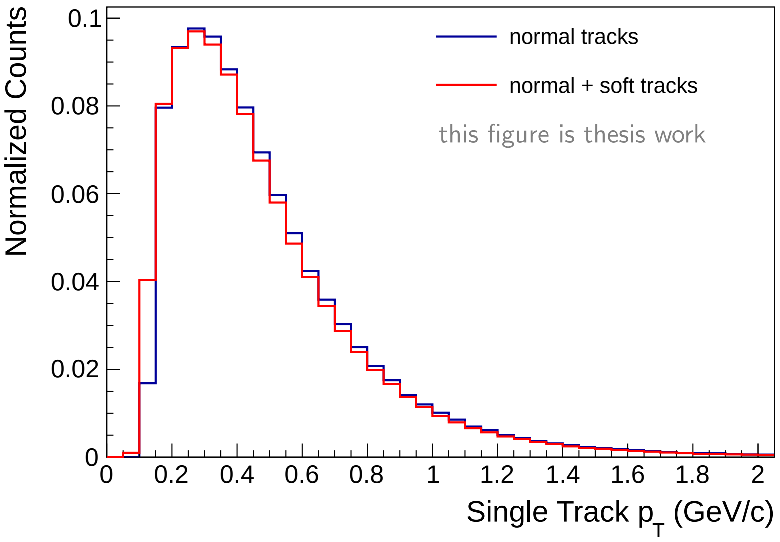

Figure 4.15.: p_T-distribution for single tracks in two-track events using the normal cuts and the combination of soft and normal tracks.

4.7.2. Double-Gap Fraction as Function of Multiplicity

As mentioned above, the multiplicity distributions of the Monte Carlo generators do not reproduce the data. In order to compare the results from data, PYTHIA6 and PHOJET despite of this inconsistency, the gap fraction can be analysed in multiplicity bins. The number of combined tracks is used for the charged multiplicity. The corresponding distribution is shown in Fig. 4.16. The gap fraction is calculated according to

$$R_{DG}(n_{ch}) = \frac{N_{DG}(n_{ch})}{N_{\mathrm{MinBias}}(n_{ch})} \ , \tag{4.18}$$

with $N_{\mathrm{MinBias}}(n_{ch})$ the number of events with multiplicity n_{ch} after the vertex cut $|z| < 4\,\mathrm{cm}$ and the pileup rejection, as described in Chapter 4.5, and the corresponding double-gap events $N_{DG}(n_{ch})$. The black filled circles are obtained from data of 2010. PYTHIA6 without tuning (orange triangles) is closest to the data. After tuning to match the diffraction dissociation contributions (blue full rectangles), the performance however becomes worse. All the tuned gap fractions are decreased as compared to no tuning. PHOJET including central diffraction (green open circles) is systematically lower than the tuned PYTHIA6 sample. Without central diffraction (cyan open rectangles), the discrepancy increases to more than an order of magnitude and becomes worse after tuning (red full triangles). The tuned datasets run out of statistics for multiplicities above five. The gap fraction for the central-diffractive PHOJET events are shown with blue open triangles. The bottom part of Fig. 4.16 shows the ratio of the MC predictions to the data. An even-odd staggering is visible in this presentation. More detailed studies of these data are necessary for an improved understanding of the origin of this staggering.

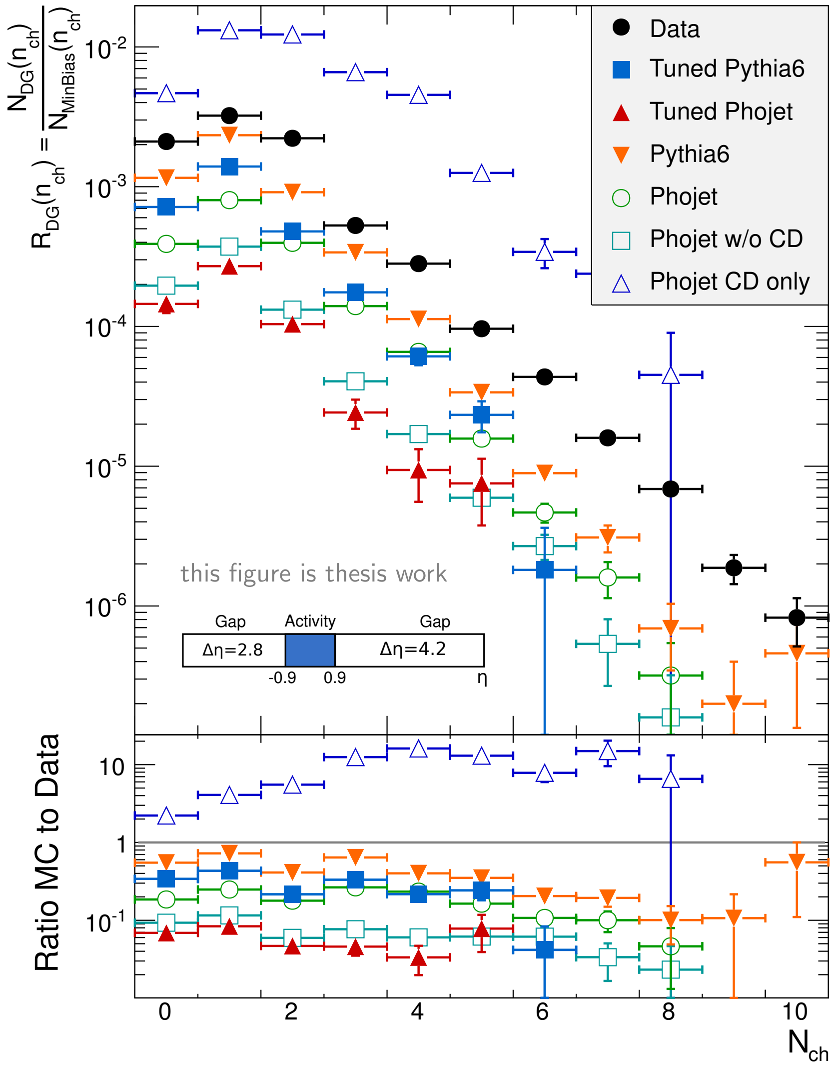

Figure 4.16.: Double-gap fraction as function of multiplicity.

4.7.3. Double-Gap Fraction per Multiplicity in a Minimum-Bias Event

The raw multiplicity distributions within $|\eta| < 0.9$ are shown in Fig. 4.17. As shown on the left-hand side, PYTHIA6 overestimates the likelihood of low multiplicities and underestimates at large multiplicities. PHOJET minimum-bias data show the opposite behaviour. Since a low multiplicity should lead to a higher gap probability, this could be a reason for a higher double-gap cross section in PYTHIA6 as compared to PHOJET. The central-diffractive events of PHOJET are clearly shifted to lower multiplicities than the minimum-bias events. Very interesting is the fact, that the pure central-diffractive dataset of PHOJET has the correct probability for the track multiplicity of one and two in the events with double gap as shown in the plot

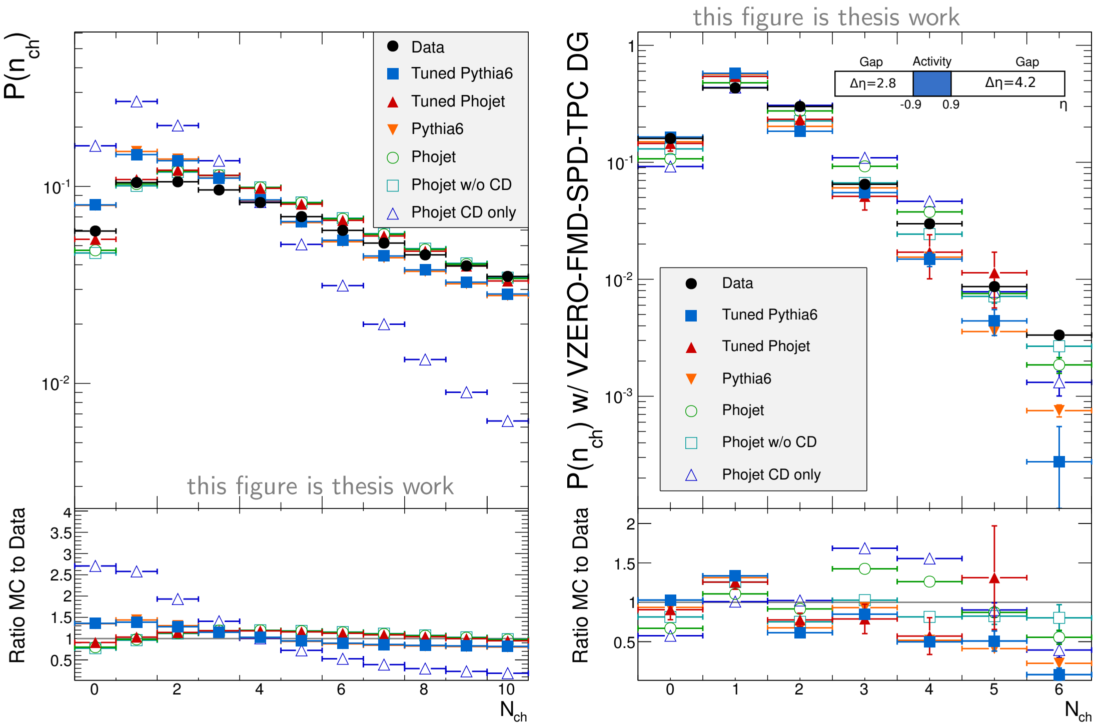

Figure 4.17.: Raw multiplicity distributions from the combination of soft and normal tracks for the different datasets without gap requirement (left) and VZERO-FMD-SPD-TPC double-gap events (right).

on the right-hand side of Fig. 4.17. The other datasets underestimate the two-track likelihood and overestimate the one for a single track.

Furthermore as discussed in Chapter 4.6.4, the multiplicity distributions in the forward regions differ as well. While we cannot change the forward multiplicity distributions in the forward regions after the MC production, we can instead adjust the relative contribution of the multiplicity classes to the overall gap fraction. This is done by convoluting the double-gap fraction as a function of the multiplicity of the different MC datasets with the raw multiplicity distribution from data. The resulting distributions in Fig. 4.18 show the likelihood to find a double-gap event of a given multiplicity in an average event of the corresponding data sample using the intrinsic multiplicity distribution of the different samples and the one from data. The integrated values are given in Table 4.3 .

For most of the MC datasets, the use of the multiplicity distribution from data leads to a lower double-gap fraction. For the PHOJET data sample containing only central diffraction, the raw multiplicity distribution from minimum-bias data is not the best choice, since central diffractive events are assumed to be of lower multiplicity. The tremendous change of the double-gap fraction due to the adjusted multiplicity distribution, however, substantiates the large influence of the multiplicity and confirms the need for multiplicity-oriented tuning of our MC generators.

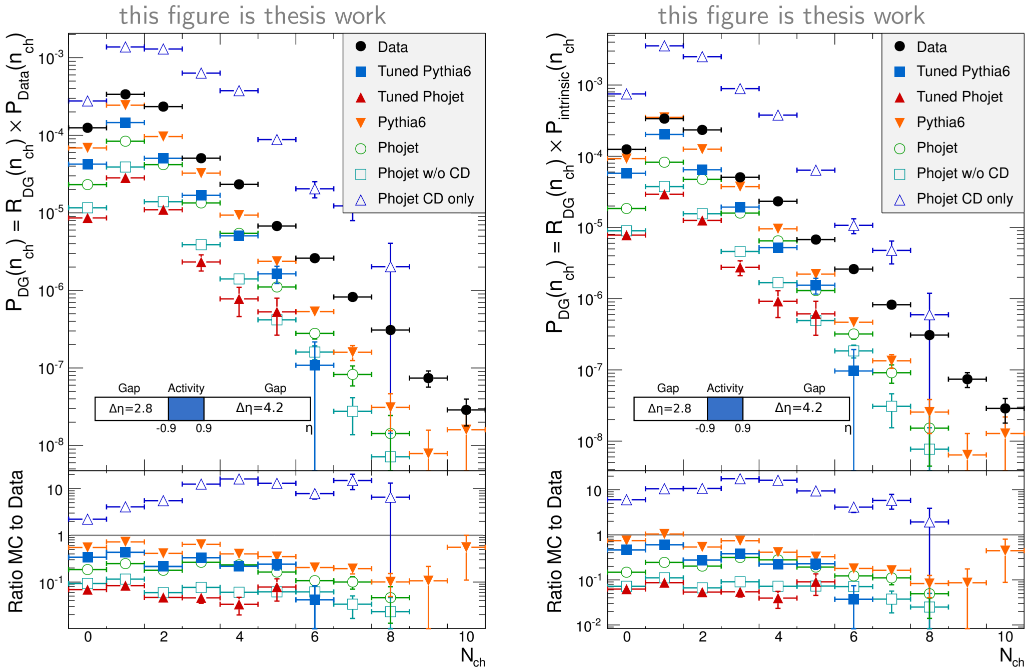

(a) multiplicity distribution from data (b) intrinsic multiplicity distribution

Figure 4.18.: Probability to find a double-gap event of a certain multiplicity in an average event of the corresponding sample.

Table 4.3.: Comparison of the double-gap fraction integrated over multiplicity for different datasets using the intrinsic and the multiplicity distribution obtained from data.

	VZERO-FMD-SPD-TPC Double-Gap Fraction	
Dataset	$P(n_{ch})$ from data	intrinsic $P(n_{ch})$
Data	$7.81 \cdot 10^{-4}$	$7.81 \cdot 10^{-4}$
Tuned PYTHIA6	$2.62 \cdot 10^{-4}$	$3.51 \cdot 10^{-4}$
Tuned PHOJET	$5.15 \cdot 10^{-5}$	$5.39 \cdot 10^{-5}$
PYTHIA6	$4.54 \cdot 10^{-4}$	$6.19 \cdot 10^{-4}$
PHOJET	$1.69 \cdot 10^{-4}$	$1.72 \cdot 10^{-4}$
PHOJET w/o CD	$7.04 \cdot 10^{-5}$	$6.91 \cdot 10^{-5}$
PHOJET CD only	$4.08 \cdot 10^{-3}$	$8.15 \cdot 10^{-3}$

4.8. Two-Body Study

Beyond the study of inclusive single-track observables, central diffraction can be examined for many-body observables. The simplest of such observables can be studied in two-track events. These two-body observables are used to study the qualitative differences in central exclusive systems as compared to inelastic-hadronic production. In the following, the impact of different selection criteria on the background and, finally, qualitative differences of double-gap and no-gap data are discussed. Furthermore, the influence of the selection on the number of available events is analysed. The invariant-mass distributions are not corrected for acceptance and efficiency.

First of all, the invariant-mass distribution for two-track events is evaluated for different gap conditions. Unless specified otherwise, particle identification is not used, and the particles are assumed to be pions. Each mass distribution is given for unlike-sign as well as like-sign pairs. Like-sign pairs can result from two-pair production. One track of each pair can be missed due to the finite detector acceptance. If the two undetected tracks are of the same charge, then the two measured tracks will combine to a like-sign pair. This combinatorial background contributes equally to the like and unlike-sign pair distribution if the detector acceptance is

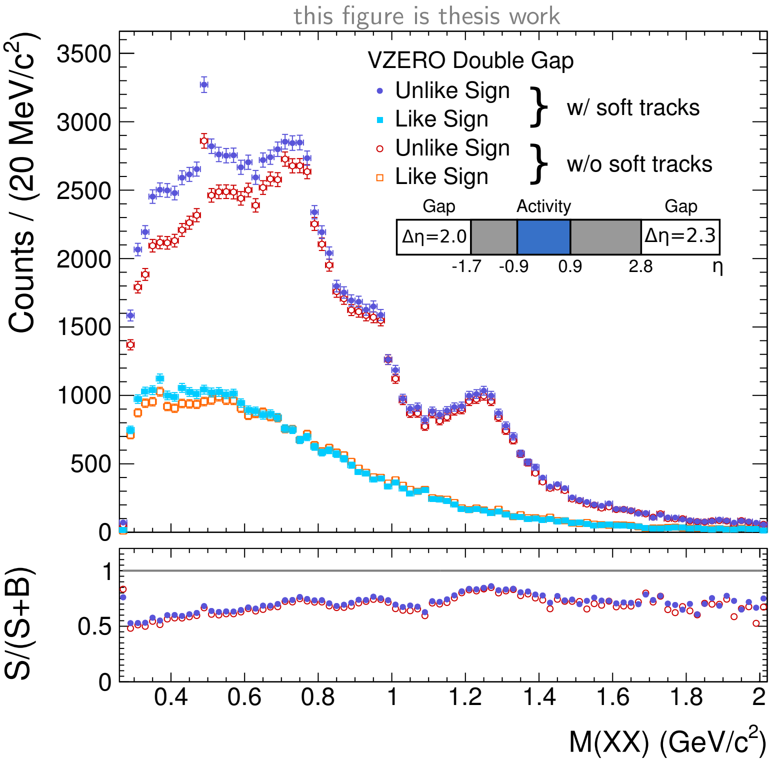

Figure 4.19.: Invariant-mass distribution for two-track events with a VZERO double gap.

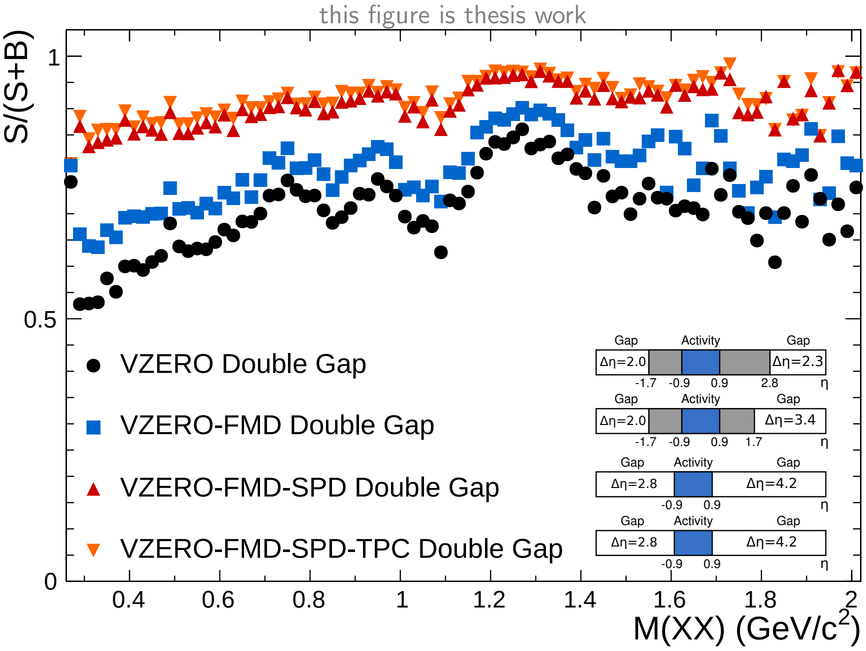

Figure 4.20.: Comparison of the $S/(S+B)$-ratio for different gap conditions.

charge-symmetric. The unlike-sign distribution therefore contains the signal and the background whereas the like-sign distribution contains only background. The combinatorial background in the unlike-sign pair distribution can therefore be corrected on a statistical basis by subtracting the like-sign pair distribution.

In Fig. 4.19 the invariant-mass distribution is shown for VZERO double-gap two-track events with normal track cuts (open symbols) and for the combined track cuts (full symbols). The ratio of signal to signal-plus-background $S/(S+B)$ is shown at the bottom of Fig. 4.19. In the unlike-sign invariant-mass distribution several resonances structures are visible. The spectrum obtained using the combined track cuts shows an enhancement especially at low invariant masses as compared to the spectrum from normal tracks. Due to the improved multiplicity response, all further invariant-mass distributions are based on the combined track cuts. An overview of the number of events with a certain gap condition and further cuts can be found in Table 4.4.

The ratio $S/(S+B)$ is shown in Fig. 4.20 for different gap conditions. This ratio is substantially improved from the VZERO gap (black circles) to VZERO-FMD gap (blue rectangles) to VZERO-FMD-SPD gap (red triangles). The influence of the TPC is not as prominent as for the other detectors, and the $S/(S+B)$ for the VZERO-FMD-SPD-TPC double-gap (orange triangles) is only slightly better than for the VZERO-FMD-SPD gap. The number of two-track events with double gap is reduced by about a factor of 2 from $2.2 \cdot 10^5$ to $1.1 \cdot 10^5$ events when changing from VZERO to the full double-gap. The resulting invariant-mass distribution with the full double-gap is shown in Fig. 4.21. Compared to the spectrum of the

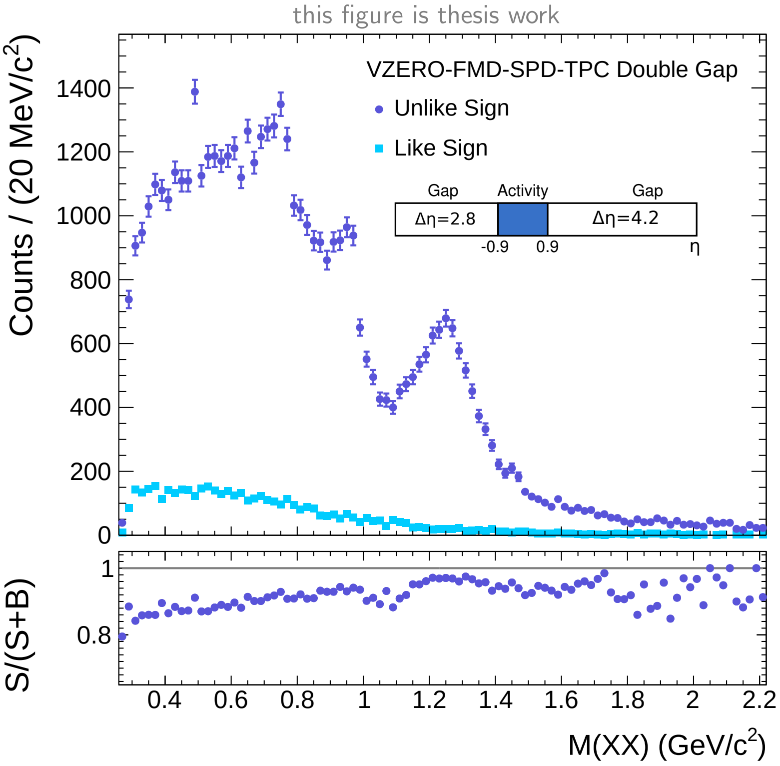

Figure 4.21.: Invariant-mass distribution for two-track events with a VZERO-FMD-SPD-TPC double gap.

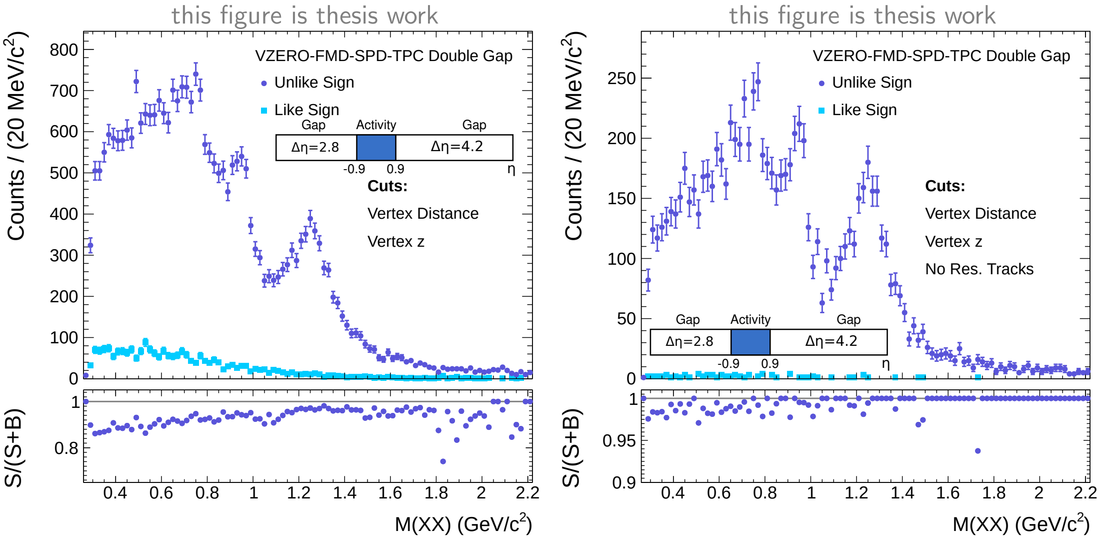

Figure 4.22.: Invariant-mass distribution for two-track events with a VZERO-FMD-SPD-TPC double gap, with vertex coincidence cut and z-vertex restricted to $\pm 4\,\mathrm{cm}$ (left and right) and no tracks rejected by cuts in the event (right).

VZERO gap shown in Fig. 4.19, the $S/(S+B)$ ratio is improved by about a factor of 1.3 on average. Furthermore, the resonances at the invariant masses of just below $1\,\mathrm{GeV}/c^2$ and at approximately $1.3\,\mathrm{GeV}/c^2$ become more prominent.

The purity of the two-track distribution can be further enhanced by a condition on the maximum distance between the vertex of tracks and the vertex of SPD tracklets. This condition avoids that two different vertices are accepted as primary vertex by the algorithms. However, the influence of this cut is marginal, as events with two vertices are already reduced by the pileup rejection in the event cuts. One remaining reason for a large distance of the vertices is the resolution being deteriorated by dead detector channels. About 7% of the events are removed by such a coincidence cut of maximum vertex distance 0.5 cm.

Furthermore, the vertex range in z can be restricted from ±10 cm to ±4 cm, as is done in the cross-section study to achieve a continuous gap coverage. This results in a reduction of statistics by a factor of about 1.6, however the like-sign background is more reduced as shown on the left-hand side of Fig. 4.22

The purity of the data sample can further be enhanced by rejecting events containing track candidates which do not pass the track cuts. Removing all these events leads to an event sample as shown in Fig. 4.22 (right). Compared to the previous invariant-mass spectrum on the left of Fig. 4.22, the K_s contribution is eliminated within the

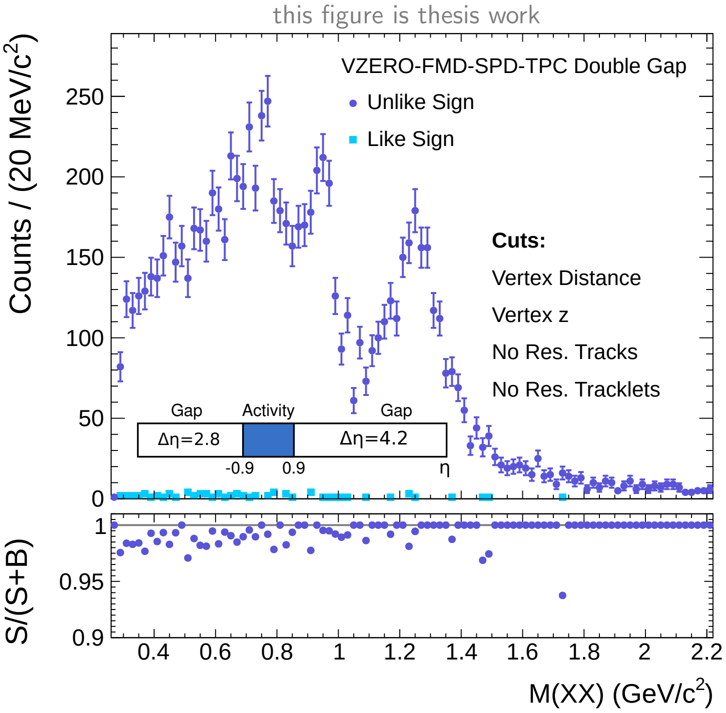

Figure 4.23.: Invariant-mass distribution for two-track events with a VZERO-FMD-SPD-TPC double gap.

statistical errors. Considering not only rejected tracks but also SPD tracklets not assigned to a track, one can still slightly increase the purity. The corresponding plot is shown in Fig. 4.23. While the rejection of events with tracks removed by cuts decreased the event sample by about a factor 2.8, this tracklet cut reduces the sample only by about 0.5%.

The double-gap events with the SPD tracklet cut described above are shown in Fig. 4.24 together with the corresponding distribution of no-gap events. The invariant-mass distribution of double-gap events shown in Fig. 4.24 shows a clear enhancement at an invariant mass just below $1\,\mathrm{GeV}/c^2$ and $1.3\,\mathrm{GeV}/c^2$. Possible candidates for these peaks are the $f_0(980)$ and the $f_2(1270)$ resonances with masses of $980 \pm 10\,\mathrm{MeV}/c^2$ and $1281.8 \pm 0.6\,\mathrm{MeV}/c^2$, respectively, as listed in the PDG [19]. Both resonances mainly decay into two pions. The width of about $185\,\mathrm{MeV}/c^2$ matches approximately in the case of the $f_2(1270)$. The correct framework for extracting the parameters of overlapping resonances is a Partial Wave Analysis

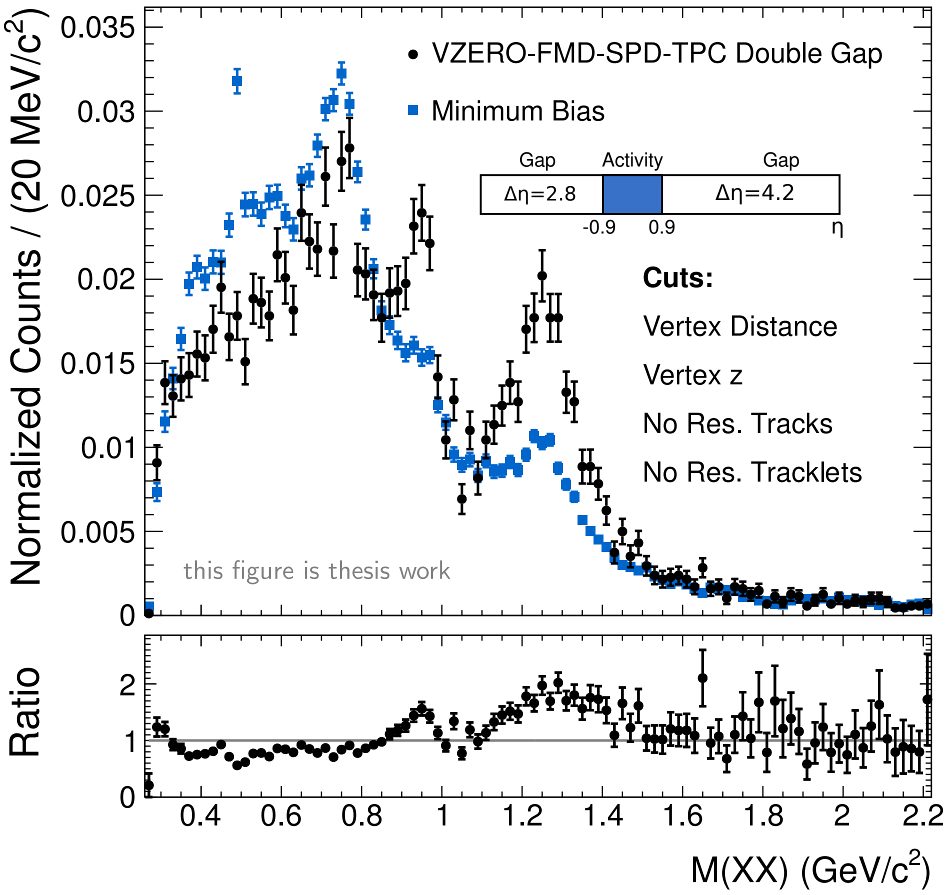

Figure 4.24.: Comparison of events with the full double-gap and vertex-distance, vertex-z cuts as well as no rejected tracks nor tracklets to the invariant-mass distribution of two-track minimum-bias events.

(PWA). Such an analysis would not only identify the resonances, but additionally estimate the fraction of the non-central-diffractive contribution, as for example states produced in a double-Pomeron exchange should not have negative charge parity. With the presently available statistics of more than $2 \cdot 10^4$ two-track double-gap events passing the most stringent selection, a PWA should be feasible. Furthermore, such an analysis can be applied to the datasets with looser cuts, in order to get a more quantitative measure of the background than the unlike-sign invariant-mass distribution.

The region below an invariant mass of $800\,\mathrm{MeV}/c^2$ is difficult to interpret, since acceptance and efficiency decrease, which is further discussed in detail below.

Table 4.4.: Overview of the two-track event statistics with unlike-sign (ULS) and like-sign (LS) charge combination and after like-sign subtraction (ULS-LS) in data and the MC simulation generated PYTHIA6 and PHOJET, as well as the central-diffractive data from PHOJET.

	Data				**Pythia6**			
	ULS	**LS**	**ULS-LS**	**ULS/LS**	**ULS**	**LS**	**ULS-LS**	**ULS/LS**
V0 Double Gap	220240	68457	151783	3.2	654811	324533	330278	2.0
V0-FMD Double Gap	162088	38308	151783	4.2	86760	29450	57310	2.9
V0-FMD-SPD Double-Gap	110721	11336	99385	9.8	43244	9152	34092	4.7
V0-FMD-SPD-TPC Double Gap	107250	9449	97801	11.4	40515	7911	32604	5.1
V0-FMD-SPD-TPC Double Gap Vtx. Dist. Cut	99788	8831	90957	11.3	37842	7404	30438	5.1
V0-FMD-SPD-TPC Double Gap Vtx. Dist. Cut, Vtx. z Cut	63227	4945	58282	12.8	23988	4566	19422	5.3
V0-FMD-SPD-TPC Double Gap Vtx. Dist. Cut, Vtx. z Cut, No Res. Trks.	22606	196	22410	115.3	8234	574	7660	14.3
V0-FMD-SPD-TPC Double Gap Vtx. Dist. Cut, Vtx. z Cut, No Res. Trks, No Res. Trklts.	22522	183	22339	123.1	8154	559	7595	14.6

	Phojet				**Phojet Central Diffracction Only**			
	ULS	**LS**	**ULS-LS**	**ULS/LS**	**ULS**	**LS**	**ULS-LS**	**ULS/LS**
V0 Double Gap	468413	293044	175369	1.6	12908	1997	10911	6.5
V0-FMD Double Gap	42720	17695	25025	2.4	8430	1276	7154	6.6
V0-FMD-SPD Double-Gap	30833	10613	20220	2.9	3040	97	2943	31.3
V0-FMD-SPD-TPC Double Gap	20646	7312	13334	2.8	3013	91	2922	33.1
V0-FMD-SPD-TPC Double Gap Vtx. Dist. Cut	14904	2644	12260	5.6				
V0-FMD-SPD-TPC Double Gap Vtx. Dist. Cut, Vtx. z Cut	9850	1818	8032	5.4				
V0-FMD-SPD-TPC Double Gap Vtx. Dist. Cut, Vtx. z Cut, No Res. Trks.	13919	2157	11762	6.5				
V0-FMD-SPD-TPC Double Gap Vtx. Dist. Cut, Vtx. z Cut, No Res. Trks, No Res. Trklts.	9215	1439	7776	6.4				

4.8.1. Acceptance and Efficiency

Due to the solenoidal magnetic field of $B = 0.5\,\mathrm{T}$, a minimal p_T of a particle of about $300\,\mathrm{MeV}/c$ is needed for TOF to become efficient as shown in Fig. 3.6. In principle, the tracking works at lower p_T, however, at a decreased efficiency. This reduction of efficiency can be seen, for example, in a plot of pair p_T versus invariant mass. This reduction of efficiency becomes clearly evident in Fig. 4.25 for pairs of low mass and low p_T, even though soft tracks are included. Full efficiency at $p_\mathrm{T} = 0\,\mathrm{MeV}/c$ is only reached for pair masses which are larger than about $800\,\mathrm{MeV}/c^2$.

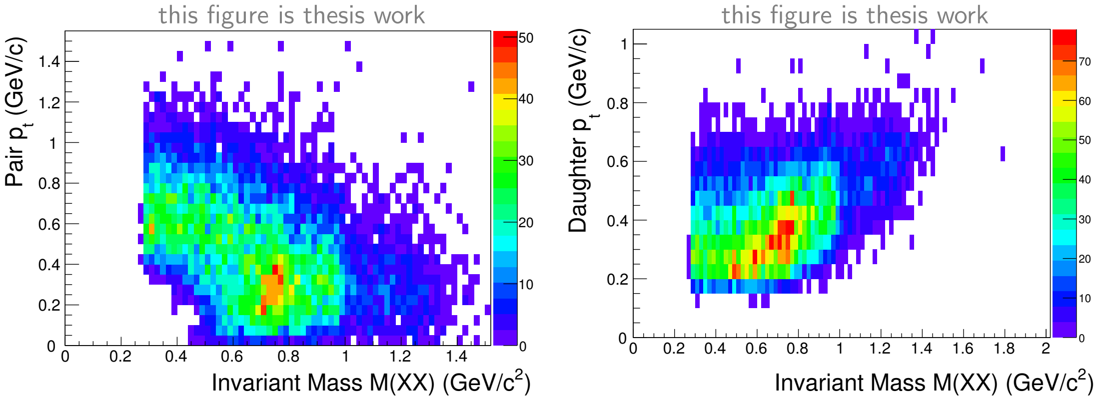

Figure 4.25.: Pair p_T vs pair invariant mass(left), single track p_T vs pair invariant mass, both for events with VZERO-FMD-SPD-TPC double-gap.

A reduced magnetic field in the central barrel would improve the p_T-threshold of TOF, for example. However, the reduced magnetic field would not help if the p_T-threshold is dominated by the energy loss in the material budget, as presented for example in Fig. 4.5. The reduced B-field leads, in addition, to an increased background seen by the detectors according to test measurements.

4.8.2. Particle Identification (PID)

For a double-gap analysis requiring a high-purity pion sample, Particle Identification (PID) is needed. In the following such capabilities are studied. In the analysis task the combination of ITS, TPC and TOF is implemented. ITS information is only used for soft tracks. In this case the identification is done by using an inclusion cut of 3σ around the pion line. The normal tracks are identified by using TPC and TOF. Two selections are done for these tracks. The first one is based on an inclusion combined with an exclusion at the crossings, both with ranges of 3σ. The second selection is only based on an inclusion cut of a 3σ-range requiring TOF and TPC.

While exclusion cuts enhance the purity in comparison to standalone inclusion cuts, they also lead to a loss of statistics. In addition, the momentum distribution is biased in the crossing region. Therefore, the description of the energy loss dE/dx in the detectors is crucial, due to the resulting positions of the crossings. An incorrect position of the crossings would lead to a wrong acceptance and efficiency correction.

The overview of the statistics of the double-gap two-track pairs after PID is shown in Fig. 4.26. Only events with unlike-sign tracks and with full double gap and a vertex-z within 4 cm are taken into account. The assignment of the tracks to particle one and two is done randomly. The colours indicate the relative abundance of a PID combination in the overall event sample, while the numbers are the absolute numbers of unlike-sign pairs with the corresponding PID. More than half of the events are identified to be two-pion events, using the tighter cuts combining in- and exclusion. The abundance of kaon pairs is lower by two orders of magnitude. Particles, which are not identified are assigned to the category ‘X’. Most of them are paired with a pion, also about twice the number of events with a kaon pair show a kaon and an unidentified track, however.

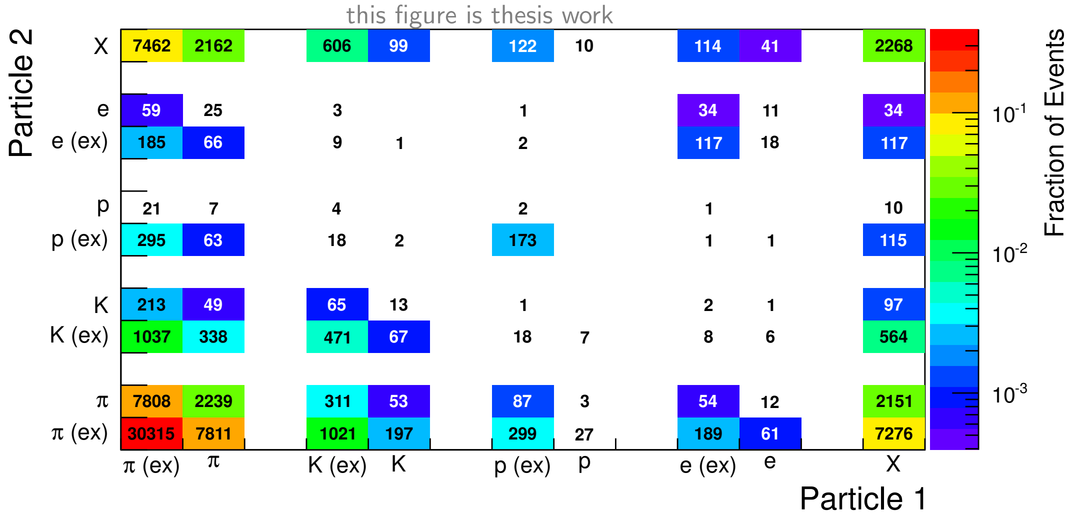

	π (ex)	π	K (ex)	K	p (ex)	p	e (ex)	e	X
X	7462	2162	606	99	122	10	114	41	2268
e	59	25	3		1		34	11	34
e (ex)	185	66	9	1	2		117	18	117
p	21	7	4		2		1		10
p (ex)	295	63	18	2	173		1	1	115
K	213	49	65	13	1		2	1	97
K (ex)	1037	338	471	67	18	7	8	6	564
π	7808	2239	311	53	87	3	54	12	2151
π (ex)	30315	7811	1021	197	299	27	189	61	7276

Figure 4.26.: Overview on the statistics of pions, kaons, protons and electrons using two types of PID cuts, in events with full double-gap and vertex-z within ±4 cm, particles identified using a combination of in- and exclusion cuts are labelled ‘(ex)’.

The track pairs are categorised in the analysis framework into three groups per particle. The first one contains track pairs in which both tracks are identified using inclusion and exclusion cuts. The second category consists of all events where both tracks are identified as the same particle at least using inclusion cuts. The third category contains all events with one identified and one unidentified track.

Since the statistical errors are significant, the PID is not used with choice of the most stringent gap cuts. In order to study kaon pairs, another gap selection and cut would be needed to optimise the statistics. The present statistics of kaon pairs would not allow a PWA.

4.8.3. Monte Carlo Studies

The same tool chain used to analyse the data is applied to the MC simulated data. Due to the small number of double-gap events observed in the MC minimum-bias samples, only the VZERO-FMD-SPD-TPC gap condition without the additional vertex and residual track and tracklet cuts is analysed. The corresponding results are shown in Fig. 4.27. Both the spectrum obtained from PYTHIA6 and from central-diffractive PHOJET events do not show the same prominent resonance structures as shown in Fig. 4.24 at an invariant mass of $1\,\mathrm{GeV}/c^2$ and at $1.3\,\mathrm{GeV}/c^2$. Furthermore, the differences between the double-gap events and the events without a gap requirement are not as striking as in the data. However, below an invariant mass of $800\,\mathrm{MeV}/c^2$ both mass distributions show a similar shape as observed in the data. These findings support the notion that this invariant-mass range is strongly affected by acceptance effects. The invariant-mass distribution from PHOJET minimum-bias data is not significantly different from the one of PYTHIA6 or the pure central-diffractive PHOJET sample. Overall, the MC generators do not succeed in reproducing the two-track invariant-mass distribution neither for double-gap nor for no-gap events. Resonances are visible in the data, independent of the gap requirements, whereas the large statistical errors of the MC data sample do not allow to make conclusive statements.

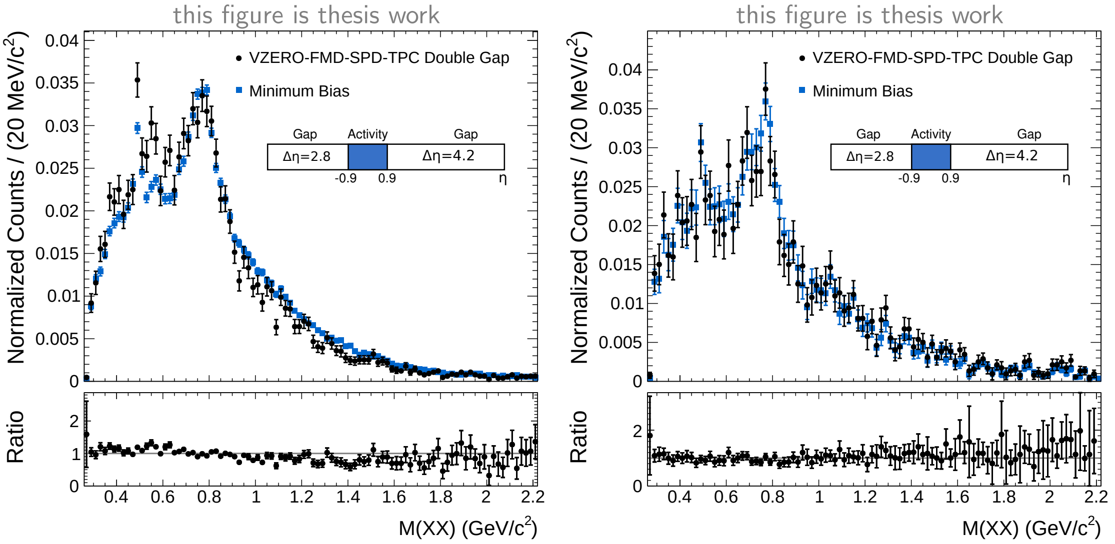

Figure 4.27.: Comparison of VZERO-FMD-SPD-TPC double-gap events to a minimum-bias two-track invariant-mass distribution for PYTHIA6 minimum bias events (left) and PHOJET central-diffractive events (right).

5. Results and Discussion

In the following, the results of analysing double-gap events from minimum-bias data are discussed. In addition, possible improvements for the double-gap analysis are outlined.

5.1. Double-Gap Cross Section

The double-gap cross section analysed from different run periods in 2010 is measured to be $44.0 \pm 0.1(stat.) \pm 7.0(syst.)\,\mu$b. This value of $44\,\mu$b represents the bare value as extracted from the data. No corrections have been applied to this value.

The uncertainty of the derived cross section is clearly dominated by the systematic error. The different contributions to the systematic error are discussed in Chapter 4.6.1, and summarised in Table 4.1.

The largest contribution to the systematic error is about 6% and results from the event selection. This bias can be studied using two different approaches. First, the fraction of events without a vertex can be evaluated using MC simulations from different generators. This fraction can be used to correct for the bias introduced by requiring a vertex in the event selection. An estimate for the uncertainty of this correction can be derived using the deviation of the event fraction without a vertex in data and different MC samples. Second, the evaluation could be done using random vertex positions for events without a vertex. Future detailed studies might therefore be able to reduce this bias of currently 6%.

A systematic uncertainty of 3.5% originates from the determination of the ALICE proton-proton luminosity at $\sqrt{s} = 7\,\mathrm{TeV}$ [77]. This uncertainty is analysed from data recorded with single-bunch beams. Corresponding data have also been taken with multiple-bunch beams, but are not yet analysed. The multiple bunch approach averages over many bunches, and hence improves the uncertainty related to the use of one bunch only. It is expected that the luminosity at $\sqrt{s} = 7\,\mathrm{TeV}$ can be determined with the multi-bunch data with an accuracy of 2%, similarly as for $\sqrt{s} = 2.76\,\mathrm{TeV}$ where the luminosity is known at the level of 1.8%. The uncertainty of the luminosity determination can still be reduced if the presently limiting factor, the length scale calibration, is better understood. It is expected that future luminosity measurements are possible with an accuracy of 1% [78].

The systematic error resulting from the efficiency of the central detectors is derived to be 5.2%. This value reflects the efficiency of the SPD FastOR at L0-trigger level, which is about 75% on average. The necessary corrections are calculated by assuming a uniform particle distribution, and thereby all particle correlations due to decay kinematics and energy-momentum conservation are neglected. The resulting bias is therefore only approximate. However, this bias tends to zero when the SPD FastOR efficiency approaches 100%, and hence the associated uncertainty will disappear. For the currently available dataset, the double-gap cross section could be studied as a function of the FastOR efficiency by masking out a fraction of the FastOR chips in the offline analysis. This information could be used to extrapolate the cross section to a fully efficient SPD FastOR.

Inefficiencies of the gap detectors lead to a systematic error of 4.9%. This number is derived by approximating the forward multiplicity distributions by the ones at mid-rapidity, and by convoluting with the single-track efficiency as determined by MC simulations. The approximation used here is necessary since the FMD information is taken from the $\mathrm{d}N/\mathrm{d}\eta$-analysis task which only provides the mean multiplicity. The use of the measured multiplicity distribution in the gap region would result in a more reliable estimate of the cross-section bias due to the gap inefficiency.

The uncorrelated systematic errors in the cross section evaluation are estimated by analysing the averages of different run periods. The resulting value is 1.3%, which is small compared to the contributions described above. This small value illustrates that the double-gap analysis presented in this thesis leads to stable results.

The two MC generators which are used to estimate the hadronic background in the double-gap sample, PYTHIA6 and PHOJET, differ in their prediction by a factor of six. Even after correcting for improved forward multiplicity distributions, the PYTHIA and PHOJET double-gap background predictions of $6.5\,\mu$b and $1.5\,\mu$b differ by a factor of about four. These numbers indicate, however, that only about 10% of the experimentally measured double-gap cross section is accounted for by known non-central diffractive processes. These findings represent strong evidence that the existence of central diffraction at LHC energies is established by the double-gap condition already in the most inclusive observable, the double-gap cross section.

Events with a double-gap topology can arise from Pomeron as well as from Reggeon contributions as discussed in Chapter 2.2. Reggeon contributions are exponentially suppressed with increasing gap sizes. The dependence of the double-gap cross section on the gap-size should therefore reveal the Pomeron and Reggeon contributions, respectively. Such an analysis is possible by using the segmentation of the detectors in pseudorapidity. With the current detector setup, a maximum of three gap sizes of 0.8, 1.4 and 2.8 units in pseudorapidity, symmetrically arranged on A- and C-side, are possible. Different gap sizes will result in a variation of the contributions of dissociation channels of central diffraction shown in f) and g) of Fig. 2.4. For the gap sizes above, this variation is, however, expected to be small as compared to the cross section variation resulting from the suppression of the Reggeon exchanges. Alternatively, asymmetric gap configurations can be studied. Here, the gap-size is taken to be the maximum on one side and the dependence of the cross section on the gap size on the other side is analysed.

5.2. Gap-Fraction Multiplicity Dependence

The results obtained in the double-gap cross-section analysis indicate a background of non-central diffractive origin of about 10%. An improved understanding of this contamination is possible by studying the background differentially in multiplicity. In addition to the differences in the raw multiplicity distributions observed in the cross section analysis, further differences are found. Not only the multiplicity distributions deviate, but also the probability for a gap within a multiplicity bin. Neither PYTHIA nor PHOJET succeed in a good description of the data, but nevertheless have to be used for simulating the detector response needed for efficiency and acceptance correction. Better efficiency and acceptance corrections are therefore only possible when the description of forward physics and of central diffraction is considerably improved in these MC generators.

The even-odd staggering observed in Fig 4.16 needs further studying. Due to charge conservation, a measured odd number of tracks in double-gap events indicates that at least one track is not detected due to detector acceptance and efficiency. The finite detector acceptance and efficiency are, however, also reflected in the ratio of like-sign to unlike-sign pairs studied in the invariant-mass distributions. The multiplicity bins shown in Fig 4.16 contain all possible charge combinations. Further study of the even-odd staggering is therefore possible by applying conditions on the total charge of the tracks.

In addition to studying the multiplicity distributions in the central barrel, also the multiplicity distribution in the forward region should be analysed further. This information should be used as input for a multiplicity-based tuning of the Monte Carlo generators.

5.3. Two-Body Study

The strong evidence for central diffraction found in the double-gap cross section is further studied differentially in two-body observables. In particular, the two-track invariant mass is well suited for such differential studies. The definition of wider gaps clearly results in a suppression of the invariant-mass background as evidenced in the reduction of the mass spectrum of like-sign pairs. The comparison of the unlike-sign two-track invariant-mass distribution of double-gap events to the corresponding distribution of no-gap events shows a prominent enhancement of structures at masses just below $1\,\mathrm{GeV}/c^2$ and at about $1.3\,\mathrm{GeV}/c^2$. The distributions from the MC generators do not show these structures, and do not significantly differ for double- and no-gap events. An improved understanding of the PHOJET prediction for the two-track invariant-mass spectrum of double-gap events is only possible when the generator includes the production of resonances, in addition to the presently implemented mass continuum.

6. Summary and Outlook

In this thesis, a basic framework for analysing double-gap topology events is developed. The most important aspect in this framework is the definition of a pseudorapidity gap. This information is provided individually for VZERO, FMD, SPD and TPC gap on an event-by-event basis. Conditions on the z-position of the vertex, on the distance between track and SPD vertex, and in addition conditions on residual tracks and SPD tracklets are defined. These conditions can be used to maximise the purity of double-gap events.

First results for properties of double-gap topology events are presented. The double-gap cross section is measured to be $44.0 \pm 0.1(stat.) \pm 7.0(syst.)\,\mu\text{b}$ for a double-gap topology defined by activity within the pseudorapidity range $|\eta| < 0.9$, and a gap on A- and C-side of 4.2 and 2.8 units, respectively. No corrections are applied to this cross-section value. The background contribution from inelastic, single- and double-diffractive dissociation processes is estimated to be on the order of 10% based on the prediction of MC generators. The discrepancies of the multiplicity distributions seen in data and the generators illustrate the need for improving the MC generators to match the experimentally measured multiplicity distributions.

Furthermore, the relative abundance of gaps as function of multiplicity is studied and compared to MC generators. The generators fail to describe the data especially for double-gap two-track events. The evaluation of the average gap fraction using the measured raw multiplicity distribution shows the strong multiplicity dependence of the double-gap fraction.

Moreover, the invariant-mass distribution of two-track double-gap events is studied. For the most stringent gap definition, the invariant-mass distribution has a background of less than 1% at masses $M_{\text{inv}} > 0.8\,\text{GeV}/c^2$ as evidenced by the comparison to the like-sign distribution. The unlike-sign distribution shows clear structures just below $1\,\text{GeV}/c^2$ and at $1.3\,\text{GeV}/c^2$. The two structures are tentatively associated with the resonances $f_0(980)$ and $f_2(1270)$. The central mass and the width of these resonances can be extracted by a PWA. The mass range for $M_{\text{inv}} < 0.8\,\text{GeV}/c^2$ is strongly affected by a p_{T}-dependent pair-acceptance threshold and no conclusive statements can therefore be made.

The double-gap measurement would greatly profit from a detector coverage larger in pseudorapidity. The coverage on A- and C-side is presently limited to about 60% and 40% of the beam rapidity at $\sqrt{s} = 7\,\text{TeV}$, respectively. The planned extension of the pseudorapidity coverage includes the detector ADA on A-side and ADD on C-side. Each of these two detectors will add about 2 units of pseudorapidity coverage. However, the detectors are planned to be positioned about 8 m and 18 m away from the interaction point at A- and C-side, respectively. At C-side, the detectors are located behind the muon absorber, leading to a large amount of material in front of them.

A complementary approach to the identification of central diffraction is the tagging of forward protons. If the forward scattered proton is fully measured, then the proton kinematics at the interaction point can be reconstructed. The fractional energy loss and the scattering angle of the proton can therefore be calculated. The kinematics information of the two outgoing protons in double-gap events allows consistency checks for reducing the background. For high central diffractive masses, the missing mass as reconstructed from the information of the protons has to match the invariant mass of the central system. For lower central-diffractive masses, such as measured in ALICE, conservation of transverse momentum can be applied to the final state which consists of the two protons and the central system. The power of such a condition is used by the STAR collaboration in the analysis of Roman-pot triggered events. The detection of forward scattered protons is, however, challenging since special beam-optics settings are needed for optimal measurements of the forward protons.

A. Triggered Double-Gap Dataset

The accumulation of a large double-gap data sample is not very efficient in minimum-bias data taking due to the small cross section of central diffraction in proton-proton collisions. However, the double-gap topology can be imposed at L0 trigger level. The central activity is defined by using the SPD FastOR trigger and by a TOF trigger bit representing a TOF multiplicity larger than two. The online VZERO L0 trigger signal for no activity is used to identify the gaps. Such a trigger was implemented in the data-taking periods LHC11e and LHC11f in 2011. This trigger, called CDG5-I, is part of the rare trigger setup in ALICE. A total of $3.1 \cdot 10^6$ double-gap triggers were taken. However, only $0.8 \cdot 10^6$ of the events are recorded under good run conditions and hence suited for physics analysis. This data sample contains approximately the same number of VZERO double-gap events as are found in the analysis of the minimum-bias events presented in this thesis. The evaluation of the more stringent gap conditions leads, however, to a systematically decreased number of events in the CDG5-I triggered data. An overview of the statistics is listed in Table A.1. The TPC gap condition is imposed without a DCA-cut reducing the background sensitivity. As shown in Table A.1, only 4.9% of the CDG5-I triggered events satisfy the VZERO-FMD gap condition, as compared to 65% in the minimum-bias triggered events in 2010. This reduction of VZERO-FMD accepted events reflects a substantial deterioration of the run conditions in 2011. This degradation of run conditions is further examined in the empty-event study presented below.

Table A.1.: Overview of the event statistics with different double-gaps in minimum-bias and CDG5-I triggered data.

Double Gap	**Minimum-Bias**			**CDG5-I**		
	Events	**Fraction**	**Reduction**	**Events**	**Fraction**	**Reduction**
VZERO	846179			782931		
VZERO-FMD	552210	65%	1.5	38050	4.9%	20
VZERO-FMD-SPD	165030	19.5%	3.3	13231	1.7%	2.9
VZERO-FMD-SPD-TPC	81689	9.7%	2.0	986	0.1%	

A.1. Empty-Event Study

In order to study the data quality in terms of noise and beam background, an empty-event study is done. Empty events are triggered in crossings of empty bunches. This triggering is done using beam masks which indicate whether a position in the beam is filled with a bunch of particles. Ideally, these triggers should not show any activity in the detectors. The contamination of these events is shown in Table A.2. While in LHC10b the number of contaminated events is totally negligible, the contamination is clearly increasing in LHC10c to LHC10e. While the SPD FastOR signals show almost constant activity of 5%, FMD has an excess in LHC10c at C-side and seems to increase from period LHC10d to LHC10e. Most of the events with activity in 2010 showed single hits. In data taking in 2011, the background and noise situation deteriorates considerably. More than 50% of the empty events show noise, and also the hit multiplicity increases.

Table A.2.: Fraction of empty events with detector signals for different data-taking periods.

	10b	**10c**	**10d**	**10e**	**11e**	**11f**
FMD Hits A-side ($\eta > 0.9$)	$1 \cdot 10^{-5}$	0.3%	0.1%	2.7%	84%	62%
FMD Hits C-side ($\eta > 0.9$)	$1 \cdot 10^{-5}$	14%	0.4%	2.7%	85%	62%
SPD FastOR A-side ($\eta > 0.9$)	$1 \cdot 10^{-5}$	5%	5%	4%	52%	51%
SPD FastOR C-side ($\eta > 0.9$)	$1 \cdot 10^{-5}$	5%	4%	5%	53%	56%

The increased contamination in 2011 can have several reasons. Due to the higher beam current, the amount of beam-induced background is significantly increased. Furthermore, possible detector problems can contribute to the contamination.

A.2. Data Quality and Usability

The CDG5-I trigger suffers from several problems. As shown in Table A.1, the relative number of events with the VZERO-FMD-SPD-TPC double-gap is drastically reduced as compared to the minimum-bias data. This reduction is most-likely due to detector problems and an increased beam-induced background. The number of CDG5-I triggered events is approximately equivalent to the number of VZERO double-gap events found in the minimum-bias triggered events. As a result, this dataset cannot be used to reasonably increase the statistics for a double-gap analysis. The double-gap is very sensitive to beam-induced background, and further data taking is only useful with low beam-background.

B. ESD Preselection

In ALICE all data are written to the same stream, independent of their trigger type. This data stream is reconstructed event by event and stored in the Event Summary Data (ESD) format. The ESD events contain basically all available detector information. As a consequence, the size of an ESD event is about 1 MB for proton-proton collisions. Such an event size leads to a tremendous amount of data throughput per analysis pass. Due to the single-data-stream concept, analyses only interested in rare triggered events have to read a lot of uninteresting events. This single-stream concept leads to large overhead and slow processing. The same situation arises when rare events are analysed from the minimum-bias dataset.

The general solution to this problem is to derive Analysis Object Datas (AODs) from the ESDs. These AODs contain only a minimal subset of the event information. This subset is adjusted according to the needs of specific analyses. As a result, the AOD events are of very small size. However, due to the reduced information in the AOD events, the decision on the relevant detector data has to be taken. This is in particular a problem for analyses which depend on intricate information, such as the gap information. A systematic study for optimising the gap definition is therefore not possible based on AODs.

A different approach to this situation is the so-called ESD preselection. Exact copies of interesting events are stored during the ESD preselection. The important aspect is to keep the structure of the new ESDs identical to the original ones. The ESDs and the preselected ESDs can therefore be analysed by the same analysis code. Additional preprocessed information can be added to the preselected ESDs. The result of the preselection is a smaller dataset containing all the events of interest.

B.1. Implementation

In AliRoot, the analysis is done using classes derived from AliAnalysisTask. The AliAnalysisTask provides the functionality to access the input data. The selection and cloning of interesting events can be done with the corresponding user code. The ESD data is implemented in ROOT as a TTree. The TTree data structure contains the functionality needed to clone a selection of entries. Furthermore, the IO-concept of the AliAnalysisTask is capable of writing TTrees via its output slots. Several such tasks are chained during the analysis process. All these tasks access the same event information in memory in the same order as they are chained. This event information in memory is neither refreshed after being accessed by a task, nor

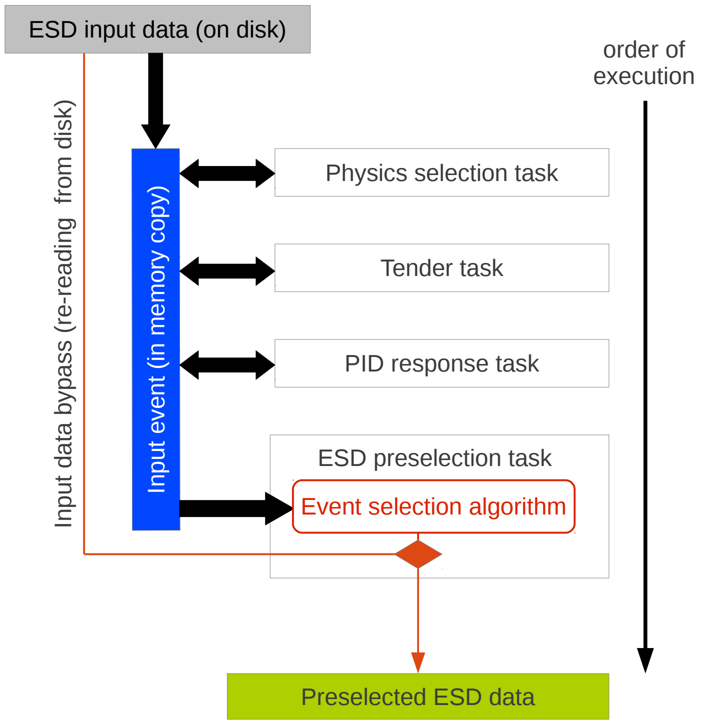

Figure B.1.: Data flow in the ESD preselection.

write-protected. Hence, the task in front of the chain can access and manipulate the data before the following tasks have access. This feature is used, for example, to add additional information to the data. In ALICE, there are currently three major applications for preprocessing tasks. First of all, the physics selection is run in order to discriminate beam-beam interactions from background. The second task is the tender, which is used to circumvent problems in the reconstructed data. Not all software problems or later improvements of the software framework justify a further reconstruction pass, however, the data are corrected using only the tender. Third, PID information is calculated online and cached to reduce the execution time of the single user tasks. For the selection of interesting events, these three tasks are mandatory. As a result, the user task can only access the manipulated data. This organisation of task chaining is contradictory to the concept of preselection where an unmodified copy of the ESD event is needed. Such an unmodified copy can, however, be created by cloning the ESD input-tree structure. The interesting events are re-read from disk into a separate location in memory, from which the new cloned tree containing only interesting events is fed. This procedure is needed, since a modified ESD would lead to incompatibility of the toolchains for preselected and normal ESDs. The main structure of the ESD preselection for double-gap events is shown in Fig. B.1.

However, not only real data has to be preselected, but also MC generated data. The

MC data contain not only the ESD tree but additional files. One file (`galice.root`) contains the event header, which describes how the generator parameters are initialised. These event headers are stored in a tree and can hence be easily processed. Another file (`Kinematics.root`) is used to store kinematics output of the event generator and the information on secondary particles created during the propagation through the detector. The third additional file (`TrackRefs.root`) contains references from the kinematics output to the reconstructed tracks. The organisation of the second and third file is incompatible with the IO-concept of the AliAnalysisTask. However, the output files can be created directly without using an IO-slot of the analysis task, and their internal structure can be rebuilt manually. A further consequence of the internal structure of `Kinematics.root` and `TrackRefs.root` is that these two files cannot be merged with ROOT's standard tools. Therefore, the amount of input events has to be adjusted in order to reach a reasonable number of events in the preselected ESD files.

C. Datasets

The following datasets and corresponding runs are used for the analysis presented in this thesis. Further information on the data samples can be found in MonALISA at `http://alimonitor.cern.ch/production/raw.jsp` for measured data and at `http://alimonitor.cern.ch/job_details.jsp` for Monte Carlo data.

C.1. Data

LHC10b.pass2

`114931, 115186, 115193, 115393, 115401, 116402, 116403, 116562, 116571, 116574, 116643, 116645, 117048, 117050, 117052, 117053, 117059, 117060, 117063, 117099, 117109, 117112, 117116, 117220, 117222`

LHC10c.pass2

`119159, 119161, 119163, 119844, 119845, 119846, 119849, 119853, 119856, 119862, 120067, 120069, 120072, 120073, 120076, 120079, 120616, 120617, 120671, 120741, 120750, 120758, 120822, 120824, 120825, 120829`

LHC10d.pass2

`126004, 126007, 126008, 126073, 126078, 126081, 126082, 126088, 126090, 126097, 126158, 126160, 126168, 126283, 126284, 126351, 126352, 126359, 126404, 126405, 126406, 126407, 126408, 126409, 126422, 126424, 126425, 126432`

LHC10e.pass2

`127714, 127718, 127822, 127933, 127935, 127936, 127937, 127942, 128185, 128186, 128189, 128191, 128452, 128483, 128486, 128494, 128495, 128503, 128504, 128609, 128611, 128615, 128678, 128820, 128823, 128824, 128835, 128836, 128843, 128855, 128913, 129512, 129513, 129514, 129520, 129527, 129528, 129540, 129586, 129587, 129650, 129652, 129653, 129659, 129723, 129725, 129726, 129729, 129735, 129736, 129738, 129742, 129961, 130149, 130157, 130178, 130342, 130343, 130354, 130356, 130517, 130519, 130696, 130704, 130793, 130795, 130798, 130799, 130834, 130840, 130844, 130847, 130848`

C.2. Phojet

LHC10d2

114931, 115193, 115393, 116102, 116288, 116402, 116403, 116562, 116571, 116643, 117050, 117052, 117059, 117063, 117092, 117109, 117112, 117116, 117220

LHC10d4a

119159, 119161, 119163, 119841, 119842, 119844, 119845, 119846, 119849, 119853, 119856, 119859, 119862, 120067, 120069, 120072, 120073, 120076, 120079, 120244, 120503, 120504, 120505, 120616, 120617, 120671, 120741, 120750, 120758, 120820, 120821, 120822, 120823, 120825, 120829

LHC10f6

125023, 125085, 125097, 125100, 125134, 125296, 125628, 125630, 125632, 125633, 125842, 125843, 125844, 125847, 125848, 125849, 125850, 125851, 125855, 126004, 126007, 126008, 126073, 126078, 126081, 126082, 126088, 126090, 126097, 126158, 126160, 126168, 126283, 126284, 126285, 126359, 126403, 126404, 126405, 126406, 126407, 126408, 126409, 126422, 126424, 126425, 126432

LHC10e21

128263, 128778, 128913, 129599, 129639, 129641, 129654, 129659, 129666, 129723, 129725, 129726, 129729, 129735, 129736, 129738, 129742, 129744, 129959, 129960, 129961, 130149, 130157, 130158, 130172, 130178, 130342, 130343, 130356, 130375, 130480, 130517, 130519, 130520, 130601, 130608, 130696, 130704, 130793, 130795, 130798, 130799, 130834, 130840, 130842, 130844, 130847, 130848

C.3. Pythia6

LHC10d1

115393, 116102, 116288, 116402, 116403, 116562, 116571, 116574, 116643, 117050, 117052, 117059, 117063, 117092

LHC10d4

119159, 119161, 119163, 119841, 119844, 119845, 119846, 119853, 119856, 119859, 119862, 120067, 120069, 120072, 120073, 120076, 120079, 120244, 120503, 120505, 120616, 120617, 120671, 120741, 120750, 120758, 120820, 120821, 120822, 120823, 120825, 120829

LHC10f6a

`124751, 125023, 125085, 125097, 125100, 125134, 125849, 125850, 125851, 125855, 126004, 126007, 126073, 126078, 126081, 126082, 126160, 126283, 126284, 126285, 126351, 126407, 126422, 126424, 126425, 126432`

LHC10e20

`127719, 128913, 129599, 129641, 129654, 129659, 129666, 129723, 129725, 129726, 129729, 129735, 129736, 129738, 129742, 129744, 129959, 129960, 129961, 130149, 130157, 130158, 130172, 130178, 130342, 130343, 130354, 130356, 130375, 130480, 130517, 130519, 130520, 130601, 130608, 130696, 130704`

C.4. Tuned Phojet

LHC11h2b

`117112`

LHC11h3b

`120671, 120505, 119161`

LHC11h4b

`126407`

C.5. Tuned Pythia6

LHC11h2a

`117112`

LHC11h3a

`120671, 120505, 119161`

LHC11h4a

`126407`

D. Acronyms and Technical Terms

AFS	Axial Field Spectrometer
ALICE	A Large Ion Collider Experiment
ATLAS	A Toroidal LHC ApparatuS
AOD	Analysis Object Data
BFKL	Balitsky Fadin Kuraev Lipatov
CERN	Conseil Européen pour la Recherche Nucléaire
CDF	Collider Detector at Fermilab
CMS	Compact Muon Solenoid
COMPASS	Common Muon Proton Apparatus for Structure and Spectroscopy
CTP	Central Trigger Processor
DAQ	Data Acquisition system
DCA	Distance of Closest Approach
ESD	Event Summary Data
FMD	Forward Multiplicity Detector
HLT	High-Level Trigger
ISR	Intersecting Storage Rings
ITS	Inner Tracking System
LHC	Large Hadron Collider
LHCb	LHC beauty
LHCf	LHC forward
MBR	Minimum-Bias Rockefeller
MoEDAL	Monopole and Exotics Detector At the LHC
MWPC	Multi-Wire Proportional Chamber
NEM	Nachtmann-Ewerz-Maniatis
OCDB	Offline Condition DataBase
PID	Particle Identification
PWA	Partial Wave Analysis
QCD	Quantum Chromodynamics
pQCD	perturbative Quantum Chromodynamics
QED	Quantum Electrodynamics
QFT	Quantum Field Theory
QGP	Quark-Gluon Plasma
RHIC	Relativistic Heavy Ion Collider
SDD	Silicon Drift Detectors
SHERPA	Simulation of High-Energy Reactions of PArticles
SHRiMPS	Soft Hard Reactions involving Multi-Pomeron Scattering
SFM	Split Field Magnet
SPD	Silicon Pixel Detector

SPS	Super Proton Synchrotron
SSD	Silicon Strip Detector
STAR	Solenoidal Tracker at RHIC
TOF	Time-of-Flight detector
TOTEM	TOTal Elastic and diffractive cross section Measurement
TPC	Time-Projection Chamber
TRD	Transition Radiation Detector

E. Bibliography

[1] B. Müller and J.L. Nagle. Results from the Relativistic Heavy-Ion Collider. *Ann.Rev.Nucl.Part.Sci.*, 56:93–135, 2006.

[2] S.L. Glashow. Partial Symmetries of Weak Interactions. *Nucl.Phys.*, 22:579–588, 1961.

[3] A. Salam. Renormalizability of gauge theories. *Phys.Rev.*, 127:331–334, 1962.

[4] S. Weinberg. A Model of Leptons. *Phys.Rev.Lett.*, 19:1264–1266, 1967.

[5] P.W. Higgs. Broken symmetries, massless particles and gauge fields. *Phys.Lett.*, 12:132–133, 1964.

[6] P.W. Higgs. Broken Symmetries and the Masses of Gauge Bosons. *Phys.Rev.Lett.*, 13:508–509, 1964.

[7] F. Englert and R. Brout. Broken Symmetry and the Mass of Gauge Vector Mesons. *Phys.Rev.Lett.*, 13:321–323, 1964.

[8] G.S. Guralnik, C.R. Hagen, and T.W.B. Kibble. Global Conservation Laws and Massless Particles. *Phys.Rev.Lett.*, 13:585–587, 1964.

[9] D.J. Gross and F. Wilczek. Ultraviolet behavior of non-abelian gauge theories. *Phys.Rev.Lett.*, 30(26):1343–1346, 1973.

[10] H.D. Politzer. Reliable perturbative results for strong interactions? *Phys.Rev.Lett.*, 30(26):1346–1349, 1973.

[11] F. Karsch. Lattice QCD at High Temperature and Density. *Lect.Notes Phys.*, 583:209–249, 2002.

[12] T. Regge. Introduction to complex orbital momenta. *Il Nuovo Cimento (1955-1965)*, 14:951–976, 1959. doi:10.1007/BF02728177.

[13] G.F. Chew and S.C. Frautschi. Principle of Equivalence for all Strongly Interacting Particles within the S-Matrix Framework. *Phys.Rev.Lett.*, 7:394–397, 1961.

[14] V.N. Gribov. *Zh. Eksperim. i Teor. Fiz.*, 41:[English transl.: Soviet Phys. – JETP 14, 1395 (1961)], 1962.

[15] S. Donnachie, G. Dosch, P. Landshoff, and O. Nachtmann. *Pomeron Physics and QCD.* Cambridge University Press, 2005.

[16] J.R. Forshaw and D.A. Ross. Quantum Chromodynamics and the Pomeron. *Cambridge Lect.Notes Phys.*, 9:1–248, 1997.

[17] V. Barone and E. Predazzi. *High-Energy Particle Diffraction.* Springer, 1. edition, 2002.

[18] P.D.B. Collins. *An introduction to Regge theory and high-energy physics.* Cambridge University Press, Cambridge [Eng.] ; New York, 1977.

[19] J. Beringer et al. Review of Particle Physics (RPP). *Phys.Rev.*, D86:010001, 2012.

[20] G. Antchev (TOTEM Collaboration). First measurement of the total proton-proton cross section at the LHC energy of $\sqrt{s} = 7\,\mathrm{TeV}$. *Europhys.Lett.*, 96:21002, 2011, arXiv:1110.1395.

[21] A. Donnachie and P.V. Landshoff. Total cross-sections. *Phys.Lett.*, B296:227–232, 1992, arXiv:hep-ph/9209205.

[22] G. A. Jaroszkiewicz and P. V. Landshoff. Model for diffraction excitation. *Phys.Rev.D*, 10:170–174, 1974.

[23] F. E. Close and G. A. Schuler. Evidence that the pomeron transforms as a nonconserved vector current. *Phys.Lett.*, B464:279–285, 1999, arXiv:hep-ph/9905305.

[24] O. Nachtmann, C. Ewerz, and M. Maniatis. A model for high-energy soft reactions. Trento Workshop on 'Exclusive and diffractive processes in high energy proton-proton and nucleus-nucleus collisions', Feb. 2012.

[25] B. Abelev et al. (ALICE Collaboration). Measurement of inelastic, single- and double-diffraction cross sections in proton–proton collisions at the LHC with ALICE. 2012, arXiv:1208.4968.

[26] S. Roesler, R. Engel, and J. Ranft. The Monte Carlo event generator DPMJET-III. 2000, arXiv:hep-ph/0012252.

[27] T. Sjöstrand, S. Mrenna, and P. Skands. A Brief Introduction to PYTHIA 8.1. *Comput.Phys.Commun.*, 178:852–867, 2008.

[28] R. Ciesielski and K. Goulianos. MBR Monte Carlo Simulation in PYTHIA8. 2012, arXiv:1205.1446.

[29] L.N. Lipatov. Reggeization of the Vector Meson and the Vacuum Singularity in Nonabelian Gauge Theories. *Sov.J.Nucl.Phys.*, 23:338–345, 1976.

[30] E.A. Kuraev, L.N. Lipatov, and V.S. Fadin. Multi - Reggeon Processes in the Yang-Mills Theory. *Sov.Phys.JETP*, 44:443–450, 1976.

[31] E.A. Kuraev, L.N. Lipatov, and V.S. Fadin. The Pomeranchuk Singularity in Nonabelian Gauge Theories. *Sov.Phys.JETP*, 45:199–204, 1977.

[32] I.I. Balitsky and L.N. Lipatov. The Pomeranchuk Singularity in Quantum Chromodynamics. *Sov.J.Nucl.Phys.*, 28:822–829, 1978.

[33] A.D. Martin et al. Diffractive Physics. 2012, arXiv:1206.2124.

[34] T. Gleisberg et al. Event generation with SHERPA 1.1. *JHEP*, 02:007, 2009, arXiv:0811.4622.

[35] E. Klempt and A. Zaitsev. Glueballs, Hybrids, Multiquarks. Experimental facts versus QCD inspired concepts. *Phys.Rept.*, 454:1–202, 2007, arXiv:0708.4016.

[36] E. Fermi. Über die Theorie des Stoßes zwischen Atomen und elektrisch geladenen Teilchen. *Z.Phys.A*, 29:315–327, 1924. doi:10.1007/BF03184853.

[37] M. Ryskin. (private communication).

[38] D. Robson. A basic guide for the glueball spotter. *Nucl.Phys.B*, 130(2):328 – 348, 1977.

[39] P. Lebiedowicz and A. Szczurek. Exclusive pp→pp$\pi^+\pi^-$ reaction: From the threshold to LHC. *Phys.Rev.D*, 81:036003, 2010.

[40] P. Lebiedowicz and A. Szczurek. Exclusive production of meson pairs and resonances in proton-proton collisions. In *Diffraction 2012 - to be published.* AIP Proceedings (online), 2012.

[41] M.G. Albrow, T.D. Coughlin, and J.R. Forshaw. Central Exclusive Particle Production at High Energy Hadron Colliders. *Prog.Part.Nucl.Phys.*, 65:149–184, 2010, arXiv:1006.1289.

[42] Y. Oren et al. The reaction pp→pp$\pi^+\pi^-$ at 2.32 GeV/c. *Nucl.Phys.B*, 53(2):269 – 281, 1973.

[43] U. Idschok et al. Analysis of the reaction pp→p$(\pi\pi)^0$p, and the question of double pomeron exchange in high-energy production processes. *Nucl.Phys.B*, 53(2):282 – 288, 1973.

[44] D.M. Chew et al. Search for Pomeron-Pomeron - 2 π Events in 205 GeV/c π^-p Interactions. *LBL-2106*, 1973.

[45] D. Denegri et al. Double pomeron exchange and diffractive dissociation in the reaction pp →pp$\pi^+\pi^-$ at 69 GeV/c. *Nucl.Phys.B*, 98(2):189 – 203, 1975.

[46] M. Derrick et al. Double Pomeron Exchange Contribution to the Reaction p p → p p $\pi^+\pi^-$ at 205 GeV/c. *Phys.Rev.Lett.*, 32:80–82, 1974.

[47] L. Baksay et al. Evidence for double Pomeron exchange at the CERN ISR. *Phys.Lett.B*, 61(1):89 – 92, 1976.

[48] B.R. Desai, B.C. Shen, and M. Jacob. Double Pomeron Exchange in High-Energy pp Collisions. *Nucl.Phys.*, B142:258, 1978.

[49] M. Della-Negra et al. Study of double pomeron exchange in pp collisions at $\sqrt{s} = 31\text{GeV}$. *Phys.Lett.B*, 65(4):394 – 396, 1976.

[50] H. de Kerret et al. Experimental Evidence for Double-Pomeron Exchange at ISR Energies. *Phys.Lett.*, B68:385, 1977.

[51] D. Drijard et al. Double pomeron exchange in the reaction pp → pp $\pi^+\pi^-$ at ISR energies. *Nucl.Phys.B*, 143(1):61 – 80, 1978.

[52] T. Akesson et al. (AFS Collaboration). A study of exclusive central hadron production at the ISR as a search for gluonium states. *Phys.Lett.B*, 133(3–4):268 – 274, 1983.

[53] T. Akesson et al. (AFS Collaboration). A search for glueballs and a study of double pomeron exchange at the CERN Intersecting Storage Rings. *Nucl.Phys.B*, 264:154–194, 1986.

[54] M.A. Reyes et al. Partial Wave Analysis of the Centrally Produced $K_S K_S$ System at $800\,\text{GeV}/c$. *Phys.Rev.Lett.*, 81:4079–4082, 1998.

[55] D. Joyce et al. Double pomeron exchange studies in p anti-p interactions at 0.63 TeV. *Phys.Rev.*, D48:1943–1948, 1993.

[56] A. Brandt et al. A Study of inclusive double pomeron exchange in $p\bar{p} \to pX\bar{p}$ at $\sqrt{s} = 630\,\text{GeV}$. *Eur.Phys.J.*, C25:361–377, 2002, arXiv:hep-ex/0205037.

[57] A. Austregesilo and T. Schlüter. Partial-Wave Analysis of the Centrally Produced $\pi + \pi$-System in pp Reactions at COMPASS. 2012, arXiv:1207.0949.

[58] L. Adamczyk. Central Exclusive Production with the STAR detector at RHIC. In *Diffraction 2012 - to be published.* AIP Proceedings (online), 2012.

[59] M. Albrow. Central Exclusive Production in CDF at the Tevatron p$\bar{\text{p}}$ Collider. In *Diffraction 2012 - to be published.* AIP Proceedings (online), 2012.

[60] K. Aamodt et al. (ALICE Collaboration). The ALICE experiment at the CERN LHC. *JINST*, 3:S08002, 2008.

[61] B. Hippolyte. Bulk matter physics and its future at the Large Hadron Collider. In Eur.Phys.J., editor, *Hot Quarks 2008*, volume C62, pages 237–242, 2008.

[62] G. Aad et al. (ATLAS Collaboration). The ATLAS Experiment at the CERN Large Hadron Collider. *JINST*, 3:S08003, 2008.

[63] S. Chatrchyan et al. (CMS Collaboration). The CMS experiment at the CERN LHC. *JINST*, 3:S08004, 2008.

[64] J. Alme et al. The ALICE TPC, a large 3-dimensional tracking device with fast readout for ultra-high multiplicity events. *NIM*, A622:316–367, 2010, physics.ins-det/1001.1950v1.

[65] P. Billoir. Track Fitting with Multiple Scattering: A New Method. *NIM*, A225:352–366, 1984.

[66] P. Billoir, R. Frühwirth, and M. Regler. Track Element Merging Strategy and Vertex Fitting in Complex Modular Detectors. *NIM*, A241:115–131, 1985.

[67] G. Contin. Performance of the present ALICE Inner Tracking System and studies for the upgrade. *JINST*, 7:C06007, 2012.

[68] B. Alessandro et al. (ALICE Collaboration). *ALICE : Physics Performance Report (Volume 2)*, volume 32, pages 1295–2040. Journal of Physics G : Nucl. Part. Phys., 2006.

[69] A. Kalweit. *Production of light flavor hadrons and anti-nuclei at the LHC*. PhD thesis, TU Darmstadt, May 2012.

[70] M.J. Berger et al. ESTAR, PSTAR, and ASTAR: Computer Programs for Calculating Stopping-Power and Range Tables for Electrons, Protons, and Helium Ions (version 1.2.3). [online] - http://physics.nist.gov/Star, August 2005. NISTIR 4999.

[71] G. Aad et al. (ATLAS Collaboration). Rapidity gap cross sections measured with the ATLAS detector in $p + p$ collisions at $\sqrt{s} = 7$ TeV. *Eur.Phys.J*, C72:1–31, 2012. doi:10.1140/epjc/s10052-012-1926-0.

[72] T. Sjöstrand, S. Mrenna, and P. Skands. PYTHIA 6.4 Physics and Manual. *JHEP*, 05:026, 2006.

[73] R. Engel, J. Ranft, and S. Roesler. Hard diffraction in hadron-hadron interactions and in photoproduction. *Phys.Rev.D*, 52(3):1459–1468, 1995.

[74] ALICE MonALISA. Run Condition Table, 2012. Summary Table of the Data Quality on a Run-by-Run Basis in ALICE, `http://pcalimonitor.cern.ch/configuration/`.

[75] K. Aamodt et al. (ALICE Collaboration). Charged-particle multiplicity measurement in proton-proton collisions at $\sqrt{s} = 7\,\text{TeV}$ with ALICE at LHC. *Eur.Phys.J*, C68(3-4):345–354, 2010.

[76] M. Hellwig. Measurement of Multiplicity Distributions in Limited Pseudo-Rapidity Windows in pp and Pb–Pb Collisions with the ALICE Detector. Diploma Thesis, University of Heidelberg, 2011.

[77] K. Oyama. ALICE luminosity calibration. In *LHC Lumi Days 2012*, Feb. 29, 2012. https://indico.cern.ch/conferenceDisplay.py?confId=162948.

[78] K. Oyama. (private communication).

F. List of Figures

G. List of Tables

Acknowledgements

Special thanks go to Prof. Dr. Johanna Stachel for giving me the opportunity to carry out my master thesis in her group and to become involved in the ALICE experiment to study high-energy particle physics.

I would like to thank Prof. Dr. Hans-Christian Schultz-Coulon for reading and evaluating my thesis.

Dr. Rainer Schicker deserves many thanks for guiding and supporting me during my thesis.

Furthermore I would like to thank Prof. Dr. Peter Glässel, Dr. Antonin Maire, Dr. Yvonne Pachmayer and Michael Winn for proofreading my thesis.

I am very grateful for all the discussions within the ALICE PWG-UD under the direction of Dr. Jean-Pierre Revol and Dr. Eugenio Scapparone. Thanks go to all members of the working group.

I would like to thank Prof. Dr. Suh-Urk Chung for many interesting discussions.

Moreover, I appreciate the discussions and help of Dr. Peter Hristov, Dr. Marian Ivanov, Jochen Klein, Xian-Guo Lu and Dr. Ken Oyama.

I would like to express my thanks to everybody in the Heidelberg ALICE group for providing a stimulating working atmosphere and for giving help whenever needed: Friederike Bock, Dr. Oliver Busch, Dr. MinJung Kweon, PD Dr. Klaus Reygers, Johannes Stiller, Martin Völkl and many more.

Last but not least, I want to thank my family and friends, especially Elena, for their support and their never ending patience.

This work is supported by the German Federal Ministry of Education and Research under promotional reference 06HD197D and by WP8 of the hadron physics programme of the 7th and 8th EU programme period.

Erklärung:

Ich versichere, dass ich diese Arbeit selbständig verfasst und keine anderen als die angegebenen Quellen und Hilfsmittel benutzt habe.

Heidelberg, den 31. Oktober 2012 Unterschrift: ....
Felix Reidt